TU/e EINDHOVEN UNIVERSITY OF TECHNOLOGY

Measurement and modelling of radiowave propagation in urban microcells

Citation for published version (APA):
Jong, de, Y. L. C. (2001). *Measurement and modelling of radiowave propagation in urban microcells*. [Phd Thesis 1 (Research TU/e / Graduation TU/e), Electrical Engineering]. Technische Universiteit Eindhoven.

Document status and date:
Published: 01/01/2001

Document Version:
Publisher's PDF, also known as Version of Record (includes final page, issue and volume numbers)

Please check the document version of this publication:

• A submitted manuscript is the version of the article upon submission and before peer-review. There can be important differences between the submitted version and the official published version of record. People interested in the research are advised to contact the author for the final version of the publication, or visit the DOI to the publisher's website.
• The final author version and the galley proof are versions of the publication after peer review.
• The final published version features the final layout of the paper including the volume, issue and page numbers.

Link to publication

General rights
Copyright and moral rights for the publications made accessible in the public portal are retained by the authors and/or other copyright owners and it is a condition of accessing publications that users recognise and abide by the legal requirements associated with these rights.

• Users may download and print one copy of any publication from the public portal for the purpose of private study or research.
• You may not further distribute the material or use it for any profit-making activity or commercial gain
• You may freely distribute the URL identifying the publication in the public portal.

If the publication is distributed under the terms of Article 25fa of the Dutch Copyright Act, indicated by the "Taverne" license above, please follow below link for the End User Agreement:

www.tue.nl/taverne

Take down policy
If you believe that this document breaches copyright please contact us at:

openaccess@tue.nl

providing details and we will investigate your claim.

Download date: 04. Oct. 2023

Measurement and Modelling of Radiowave Propagation in Urban Microcells

Y.L.C. de Jong

Measurement and Modelling of Radiowave Propagation in Urban Microcells

PROEFSCHRIFT

ter verkrijging van de graad van doctor aan de Technische Universiteit Eindhoven, op gezag van de Rector Magnificus, prof.dr. M. Rem, voor een commissie aangewezen door het College voor Promoties in het openbaar te verdedigen op donderdag 21 juni 2001 te 16.00 uur

door

Yvo Léon Christiaan de Jong

geboren te Vlaardingen

Dit proefschrift is goedgekeurd door de promotoren:

prof.dr.ir. G. Brussaard
en
prof.dr. R.J.C. Bultitude

Copromotor: dr.ir. M.H.A.J. Herben

CIP-DATA LIBRARY TECHNISCHE UNIVERSITEIT EINDHOVEN

Jong, Yvo L.C. de

Measurement and modelling of radiowave propagation in urban microcells /
by Yvo L.C. de Jong. – Eindhoven : Technische Universiteit Eindhoven, 2001.
Proefschrift. – ISBN 90-386-1860-3
NUGI 832
Trefw.: mobiele telecommunicatie / radiogolfvoortplanting /
elektromagnetische metingen.
Subject headings: mobile communication / microcellular radio /
radiowave propagation / direction-of-arrival estimation.

Cover design by ZO, 's-Hertogenbosch

© 2001 by Y.L.C. de Jong, Dordrecht

All rights reserved. No part of this publication may be reproduced or transmitted in any form or by any means, electronic, mechanical, including photocopy, recording, or any information storage and retrieval system, without the prior written permission of the copyright owner.

Aan mijn ouders
Aan Nathalie

Summary

The work reported in this thesis is aimed at contributing to a better physical understanding of radiowave propagation in urban microcell environments and, at the same time, to the development of improved propagation prediction models for such environments. Emphasis is placed on the identification, by means of advanced experiments, and modelling of the dominant propagation mechanisms in the UHF band.

The first part of the study treats the experimental characterisation of urban mobile radio channels in terms of the propagation delay and angle-of-arrival of individual multipath waves, by means of a radio channel sounder in conjunction with a synthetic antenna array. Result of these measurements is the identification of two propagation mechanisms that have hitherto received little or no attention: transmission through buildings and scattering from trees. Building transmission is particularly significant in areas directly behind buildings surrounding the base station antenna. Scattering from trees can, for example, play a predominant role in propagation around street corners.

The second part of the study discusses the development of building transmission and tree-scattering models that can be readily incorporated in ray-based propagation prediction tools. The model for transmission through buildings does not require any information about the buildings other than the exterior coordinates, the complex permittivity of the exterior walls and an effective attenuation coefficient. The latter coefficient characterises the excess loss experienced by radiowaves propagating through a building's interior and must be determined by measurements. This is done for a large set of buildings. A model for the coherent and incoherent scattering from a single tree is developed with the aid of Twersky's multiple scattering theory. Numerical results from this scattering model show reasonable to good agreement with measured data.

The third part of the study presents a new ray-tracing propagation prediction tool that incorporates the transmission and scattering models of the previous part. This tool makes use of a new method to estimate local mean power. Unlike the conventional method of adding ray powers, this method also provides accurate values for

the often occurring case of spatially correlated multipath signals. Path loss predictions for two urban microcell environments are shown to illustrate the remarkable improvement in prediction accuracy that can be achieved with the new model.

Contents

1 Introduction **1**

1.1 Background 1
1.2 Previous work at TU/e 3
1.3 Scope and outline of the dissertation 3

2 High-resolution angle-of-arrival measurements: method **5**

2.1 Introduction 5
2.2 Measurement system 6
2.2.1 Channel sounder 7
2.2.2 Synthetic array 10
2.2.3 Antennas 12
2.3 Data model 14
2.4 Angular superresolution 16
2.4.1 Beamspace processing 18
2.4.2 UCA-MUSIC 19
2.4.3 Forward/backward averaging 20
2.4.4 Effects of a finite data set 21
2.4.5 Summary of the algorithm 23
2.5 Resolution threshold 23
2.6 Numerical results 26
2.6.1 Resolution threshold 26
2.6.2 Estimation of the number of signals 28
2.7 Experimental results 30
2.8 Conclusions 32

3 High-resolution angle-of-arrival measurements: results **35**

3.1 Introduction 35
3.2 Transmission through buildings 36
3.2.1 Realistic urban microcell environment – Bern 36

3.2.2 Controlled environment 40
3.3 Scattering from trees 42
3.3.1 Realistic urban microcell environment – Fribourg 42
3.3.2 Controlled environment 46
3.4 Conclusions 48

4 Propagation into and through buildings 49
4.1 Introduction 49
4.2 Building transmission model 51
4.2.1 Surface fields 52
4.2.2 Interior fields 54
4.2.3 Transmitted fields 58
4.2.4 External scattering 60
4.3 Numerical results 61
4.3.1 Field around a building corner 61
4.3.2 Field behind a building 63
4.4 Experimental results 65
4.4.1 Measurement equipment and procedure 66
4.4.2 Determination of the transmitted field 66
4.4.3 Determination of the attenuation coefficient 68
4.4.4 Reproducibility 69
4.4.5 Description of the buildings 71
4.4.6 Results 71
4.5 Conclusions 77

5 Scattering from trees 79
5.1 Introduction 79
5.2 Vegetation model 80
5.2.1 Overall problem geometry 81
5.2.2 Scattering from branches 82
5.2.3 Scattering from leaves 84
5.2.4 Equivalent scattering amplitude and cross section 86
5.3 Scattered field 88
5.3.1 Mean field inside the canopy 88
5.3.2 Coherent scattered field 90
5.3.3 Incoherent scattered field 94
5.4 Numerical results 96
5.4.1 Branch and leaf parameters 96
5.4.2 Attenuation coefficients 98

5.4.3 Scattering cross sections of branches and leaves 98
5.4.4 Coherent scattered field 100
5.4.5 Incoherent scattered field 103
5.5 Experimental results 104
5.5.1 Measurement equipment and procedure 105
5.5.2 Attenuation 106
5.5.3 Scattering cross section 107
5.6 Conclusions 109

6 A ray-tracing propagation prediction model for urban microcells 111
6.1 Introduction 111
6.2 Model description 112
6.2.1 Database preprocessing 114
6.2.2 Ray-tracing 115
6.2.3 Channel parameter estimation 118
6.3 Estimation of local mean power 119
6.3.1 Formulation 119
6.3.2 Computation of local mean power 120
6.3.3 Numerical results 122
6.3.4 Conclusions and discussion 127
6.4 Prediction results 128
6.4.1 Transmission through buildings – Bern 128
6.4.2 Scattering from trees – Fribourg 132
6.5 Conclusions 135

7 Summary, conclusions and recommendations 137
7.1 Summary and conclusions 137
7.2 Recommendations 140

References 143

Samenvatting 151

Acknowledgments 153

Curriculum vitae 155

1

Introduction

1.1 Background

Since the early 1990's, with the introduction of the Global System for Mobile Communications (GSM) and comparable systems, the world has seen an explosive growth of the mobile telecommunications market. In 2001, mobile telecom operators are providing voice and short message services to around 700 million subscribers worldwide. Third-generation (3G) systems such as the Universal Mobile Telecommunication System (UMTS), which is expected to be taken into service in 2002 and to have reached widespread deployment around the world in 2005, are planned to provide wireless data services like Internet access at data rates up to 2 Mbps in dense urban and indoor environments [1]. The ultra-high frequency (UHF) band is attractive for providing mobile services from a propagation point of view, but radio spectrum in this band has become a scarce and therefore expensive commodity. In Europe, a total of 155 MHz has been assigned for terrestrial 3G systems, and mobile operators in most European countries have received licenses for 15 MHz of paired spectrum or less. The ability of operators to meet the expected high demands on network capacity using this limited bandwidth will be essential for the success of 3G mobile communications.

Present-day mobile networks are designed according to the so-called cellular concept, in which the service area (e.g. an entire country) is divided into separate

geographical zones called cells. Each cell is equipped with its own radio transceiver, called base station, which serves the mobile stations located inside the cell using a subset of the available radio channels. With this method each channel can be used by many different base stations, provided that the distances between them are large enough to guarantee that the co-channel interference is below the acceptance level. Probably the best way to achieve the high capacity in urban environments required for 3G systems is the deployment of cells with radii much smaller than the 1-2 km typical for the macrocells presently used for GSM. These so-called *urban microcells* employ small, low-power base stations which are placed well below the average rooftop level of the surrounding buildings, e.g. on lamp posts or building walls. The power radiated from the base station antenna is thus confined to a small coverage area (maximum dimension typically in the order of a few hundred meters), the shape of which is strongly dependent on the local street pattern. As the line-of-sight (LOS) propagation path is often blocked, radiowave propagation via other mechanisms – such as reflection, diffraction and scattering – becomes significant in urban microcell configurations.

In order to evaluate the quality and cost-efficiency of different network scenarios before purchasing and installing the costly network hardware, the planner of cellular networks must be able to produce an accurate area prediction of relevant radio channel parameters such as path loss. This process is usually referred to as *propagation prediction*. Since all coverage and interference calculations in the planning stage of cellular radio networks are based on it, propagation prediction plays a very important role in network planning. A planner who is unable to accurately predict propagation will either produce a too expensive network or – just as likely – produce a network of bad quality [2].

For the planning of macrocells, radio network planners have been relying on empirical propagation prediction models, which treat the channel transfer function as a random process, of which the statistical parameters are found from extensive measurements [3]. Although the parameters used to describe the channel statistics are usually chosen to be dependent on the general topographic characteristics of the area around the mobile station (open, suburban, urban, etc.), these models do not describe the effects of specific propagation conditions (e.g. obstruction of the LOS path). For open macrocell environments, these models are capable of providing a root-mean-square (rms) prediction error of about 6 dB, which is considered a satisfactory value for planning purposes [2]. In urban microcell environments however, propagation strongly depends on local features of the environment (such as locations, shapes and dielectric properties of the buildings), and the channel characteristics become very location-specific. For these environments, purely empirical models do not provide an acceptable prediction accuracy [2, 4].

In recent years, so-called fundamental – or deterministic – propagation prediction models, capable of providing location-specific channel predictions on the basis of an accurate building database and physical models of propagation mechanisms such as reflection and diffraction, have received much attention [4, 5]. In particular, ray-based propagation prediction, in which the propagation of radiowaves is described in terms of straight trajectories in space called rays, has become a well-established method. Although considerably better than their statistical counterparts with regard to urban microcell scenarios, ray-based models in many cases do not provide the same prediction accuracy that can at present be achieved for macrocells. Attempts to reduce the prediction error by increasing the considered number of reflections and diffractions, and by increasing the accuracy and degree of detail of the building database, have not closed this gap in accuracy. This observation has led to the conjecture that reflection and diffraction – the only propagation phenomena considered by most existing models – may be insufficient to model the urban radio channel, and to the conclusion that it would be desirable to obtain a better, more fundamental understanding of the dominant propagation mechanisms in urban microcell environments. This is the subject of the present study.

1.2 Previous work at TU/e

The research at Eindhoven University of Technology (TU/e) in the area of radiowave propagation in urban environments goes back to the work of Van Dooren [6], which was mainly concerned with field strength prediction for the planning of land mobile satellite (LMS) systems. One of the results of this work was the fully three-dimensional ray-tracing tool named *FiPre* ("Field Prediction"), which is based on geometrical optics (GO) and the uniform theory of diffraction (UTD). Under a contract with Royal PTT Netherlands (KPN), the *FiPre* software was later adapted for propagation prediction for terrestrial mobile communication systems such as GSM [7]. In 1996, the collaboration between KPN and the TU/e was continued in the form of an investigation of the dominant propagation mechanisms in urban microcell environments and the development of a propagation prediction model specifically suited for the planning of urban microcells. The present dissertation reports on the scientific results of this study.

1.3 Scope and outline of the dissertation

The purpose of this dissertation is to contribute to the development of improved deterministic propagation prediction models for urban microcell environments. At the same time, it is aimed to be a contribution to a better physical understanding of

radiowave propagation in such environments. Emphasis is placed on the identification, by means of advanced experiments, and modelling of the dominant propagation mechanisms in the UHF band.

Chapter 2 presents a method for the high-resolution measurement of the directional properties of multipath waves. This method, which is based on the use of a wideband radio channel sounder and a synthetic array of antennas, enables the characterisation of the mobile radio channel at the level of individual multipaths, by separating the multipath signals on the basis of their different propagation delay times and angles-of-arrival.

In Chapter 3, measurement results obtained in urban microcell environments, using the method proposed in the previous chapter, are discussed. Two important propagation mechanisms are identified that hitherto have received little or no attention: transmission through buildings and scattering by trees. These mechanisms are further examined in the Chapters 4 and 5.

Chapter 4 is concerned with the modelling of propagation into and through buildings. A ray-optical transmission model based on asympotic physical optics is proposed, in which the effects of the building interior are described by a specific attenuation factor which can be chosen freely. A simple and accurate method is presented for the measurement of the losses associated with transmission through buildings, and empirical attenuation factors obtained using this method are presented for a large set of buildings.

In Chapter 5, a physical model is developed for the scattering of radiowaves from deciduous trees. Tree canopies are modelled as homogeneous random media containing randomly distributed and oriented branches – modelled as dielectric cylinders – and leaves – modelled as thin dielectric disks. Expressions are derived for the coherent and incoherent tree-scattered fields and a comparison is made with experimental data.

Chapter 6 discusses a novel ray-tracing propagation prediction tool for urban microcells, which incorporates the transmission and scattering models of the previous chapters. The considerable improvement in accuracy that can be achieved using this tool is illustrated by a comparison of prediction results with measured data.

In Chapter 7, a summary is given of the main results reported in this dissertation, and overall conclusions are drawn. Also, some recommendations are made for follow-up research.

2

High-resolution angle-of-arrival measurements: method

2.1 Introduction

Due to the important role expected for deterministic propagation prediction models in the planning stage of cellular radio networks, there is a growing need for a more fundamental understanding of the dominant propagation mechanisms in the mobile radio channel. For this purpose, a number of groups have been active in the measurement of channel characteristics at the level of the individual multipath components, in particular by separating the multipath signals on the basis of their different propagation delay times and angles-of-arrival (AOAs) [8–13].

Delay measurements are usually performed in the time domain using the pseudo-noise (PN) correlation approach [14, 15]. For the measurement of AOAs, both directional antennas [8] and (synthetic) phased arrays have been applied, the latter of which benefit from their relative ease of use and suitability for digital data processing schemes, such as high-resolution (or "superresolution") algorithms. Synthetic arrays have the inherent advantages that mutual coupling between adjacent array elements is avoided, and that the radiation pattern of the elements is not affected. The most common array geometries used in practice are the uniform linear array (ULA) [12], the rectangular lattice [9, 10] and the uniform circular array (UCA) [11, 13]. A ma-

jor drawback of the ULA is that it is not suited for two-dimensional (azimuth and elevation) AOA estimation. As has been pointed out in [9], the common assumption that all waves impinge from the horizontal plane leads to considerable errors in the azimuth estimation if the elevation differs from zero. In comparison with the rectangular array, the UCA can be synthesized in a particularly simple fashion, by placing an antenna on a rotating arm. Furthermore, due to the rotational symmetry of the array configuration, the resolution performance is independent of the azimuth angles of the incident waves.

Thus far, superresolution estimation of multipath wave AOAs using a UCA has been disregarded in the literature due to the assumed low robustness of high-resolution algorithms to noise and their requirement of *a priori* knowledge of the number of incident waves [13]. Also, AOA estimation using a UCA has hitherto been limited to azimuth angles only. In this chapter, a high-resolution approach toward two-dimensional (azimuth and elevation) AOA estimation is presented which is suited for this array configuration. The increased resolution capability enables the identification of the dominant propagation paths contributing to the total received field strength, and a quantitative analysis of the propagation mechanisms involved.

The organisation of this chapter is as follows. Section 2.2 gives a description of the measurement equipment. In Section 2.3, the data model and some notation that will be used in the rest of the chapter are introduced. The algorithm for the accurate estimation of AOAs is described in Section 2.4, and an expression for the resolution threshold, which is an important performance measure, is derived in Section 2.5. Results of computer simulations of the resolution performance are given in Section 2.6, and Section 2.7 presents experimental results that were obtained in an actual built-up environment. Finally, conclusions are drawn in Section 2.8.

2.2 Measurement system

The experimental results presented in this thesis were obtained using two different measurement systems. The first system, which was made available by Ericsson Mobile Business Networks, Enschede, The Netherlands, on several occasions in the period from June 1997 to November 1998, operates at 1900 or 2000 MHz. It will further be referred to as the Ericsson system. The second measurement system was developed for the Eindhoven University of Technology (TU/e) at the Communications Research Centre, Ottawa, Canada, according to specifications very similar to those of the Ericsson system, and has been in use at the TU/e since February 1999. This system operates at 1900 MHz and will be referred to as the TU/e system. From the viewpoint of functionality the TU/e equipment is almost identical to the Ericsson equipment (view Table 2.1). The description in this section therefore applies to both

Table 2.1: Measurement system specifications.

	Ericsson system	TU/e system
Carrier frequency (MHz)	1900/2000	1900
1-dB Bandwidth (MHz)	180	100
Nominal output power (dBm)	30	30
Receiver type	stepping-correlator	sliding-correlator
Resolution (ns)	20†	20†
PN sequence length	511	511
Unambiguous range (μs)	10.22	10.22
Effective sampling rate (samples/bit)	1	4
Instantaneous dynamic range (dB)	40	40
Acquisition rate (CIR/s)	12.8	9.8
Antenna rotation time (s)	8.3	16.0
Number of synthetic array elements	106	157
Synthetic array radius (m)	0.30	0.30

† In practice, the resolution is slightly worse than 20 ns due to the limited system bandwidth.

systems, except where specifically indicated otherwise.

2.2.1 Channel sounder

The measurement system is built up around a wideband radio channel sounder, which is based on the popular pseudonoise (PN) correlation method [14, 15]. This technique utilises a periodic PN binary sequence with period T, say $a(t)$, and exploits the properties of its autocorrelation function

$$x(\tau) = \frac{1}{T}\int_0^T a(t)a(t-\tau)dt, \tag{2.1}$$

which has a pulse-like shape, to provide an estimate of the complex impulse response (CIR) of the channel under measurement. A schematic diagram of the channel sounder is given in Fig. 2.1. The abbreviation CIR is also used here and in the following to indicate a complex impulse response *estimate*, although it is acknowledged that this is, strictly speaking, not entirely accurate.

At the channel sounder transmitter, a 50 MHz clock signal drives a shift register to produce a 50 Mbit/s reference PN sequence with a period of 511 bits. This sequence then modulates a 1900 or 2000 MHz carrier, using the binary phase-shift keying (BPSK) scheme. The modulator output is amplified to a power of 30 dBm, bandpass filtered, and subsequently radiated via a suitable antenna.

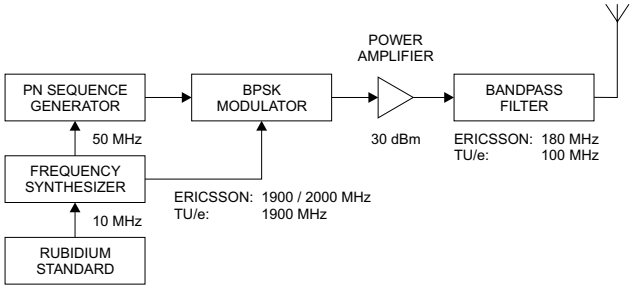

(a)

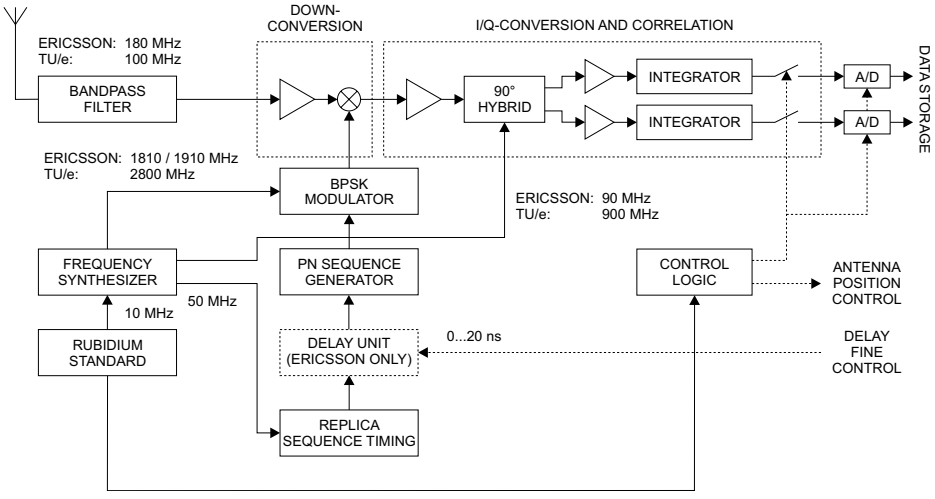

(b)

Fig. 2.1: Wideband radio channel sounder. (a) Transmitter. (b) Receiver.

At the channel sounder receiver, which is installed in a measurement vehicle, the CIR of the radio channel is estimated by demodulating and correlating the received signal with a locally generated, exact replica maximum-length sequence, which is time-shifted relative to the reference sequence. This time shifting is accomplished in different ways in the two channel sounders that were used. In the Ericsson system, which is of the stepping-correlator type, the replica sequence is delayed in discrete steps of 20 ns by means of the replica sequence timing unit. In the TU/e channel sounder receiver, the replica sequence generator is driven at a slightly lower rate (49.995 MHz) than the reference sequence generator. This produces a sequence identical with the transmitted sequence, but drifting slowly by it in time. This type of receiver is known as sliding-correlator receiver.

The in-phase and quadrature signals at the output of the correlator are *time-stretched* copies of the signals that would be seen at the output of an "ordinary" quadrature receiver if a short pulse of the form of the autocorrelation function $x(\tau)$ were transmitted over the same path through the radio channel and the transmitter and receiver filters. Thus, the channel sounder produces high-resolution time delay measurements of the channel without requiring high-speed sampling of the receiver output.

At the output of the Ericsson channel sounder receiver, a single CIR sample is produced every 0.15 ms, and the acquisition of a complete impulse response takes 78 ms. For the TU/e system these measurement times are 0.05 and 102 ms, respectively. In both systems, the measurement data samples are digitised, transferred to a personal computer and stored on a hard disk. The resulting measurement files contain CIRs with an unambiguous range of 10.22 μs (511 bits of 20 ns each) and a maximum instantaneous dynamic range of 40 dB, i.e. the ratio between the peak value of the measured delay profile and the noise floor is smaller than 40 dB. In the Ericsson system, the measured CIR is sampled at an equivalent of one sample per bit of the PN sequence; in the TU/e system the effective sampling rate is 4 samples per bit. By means of the delay unit in the Ericsson system, the clock signal that is applied to the replica sequence generator can be delayed by an additional, fixed delay time which can be externally adjusted in the range from 0 to 20 ns. Thus, the exact locations of the sample points on the measured CIR can be varied between measurements.

In order to be able to accurately measure the relative phases of multipath signals, the transmitter and receiver frequency synthesizers are locked to highly stable rubidium clocks (short-term stability better than 5×10^{-11}). To ensure accurate measurements of absolute multipath intensities, the channel sounder is calibrated prior to the measurements by connecting a known attenuation between the transmitter and the receiver.

2.2.2 Synthetic array

The channel sounder receiver is equipped with a single omnidirectional antenna on a rotating arm which is placed on top of the measurement vehicle and positioned by a motor, under control of the personal computer used for data acquisition (view Fig. 2.2(a)). Microwave absorbing material is used to minimise the effects of the vehicle roof.

During measurements the vehicle is not moving. While the channel sounder is acquiring a pre-specified number of channel responses, the antenna is rotated at constant speed along a horizontal circle with radius $r = 0.30$ m. Under the assumption that the radio channel remains stationary during the measurement, this procedure is effectively identical to the simultaneous measurement of the channel CIR at the elements of a uniform circular array of antennas (Fig. 2.2(b)). In the Ericsson system, one revolution of the antenna is completed after 8.3 s, which corresponds to the acquisition time of $M = 106$ impulse responses. Using the TU/e system, one revolution takes 16.0 s and $M = 157$.

The continuous movement of the rotating antenna introduces sensor positioning errors with respect to the assumed fixed positions $\gamma_0, \gamma_1, \ldots, \gamma_{M-1}$ of the UCA elements (view Fig. 2.2(b)). These errors are dependent on the position i of the considered delay instant within the measured CIRs and can be as large as $360^o/106 = 3.4^o$ (for the Ericsson system), which is unacceptable for the application under consideration. They can however be completely compensated for in post-processing [16].

An important UCA parameter is its radius r. As the angular estimation accuracy and resolution capability decrease with decreasing array dimensions, it is important to choose the UCA radius sufficiently large. However, there are also some important factors that limit the array size to be employed.

1. **Plane wave assumption.** The assumption that the electromagnetic field around the array can be modelled as the superposition of plane waves, which is used by the angular superresolution algorithm, requires the array size to be small compared to the distance of the array to the nearest scattering centre.

2. **Narrowband array assumption.** To ensure that each multipath wave is received identically at all array elements except for a phase factor, which is another assumption underlying the angular superresolution algorithm, the array size should be small compared to the distance covered at the speed of light during a bit period. This distance is 6 m in the present case.

3. **Practical considerations.** Practical requirements with respect to size and weight also put limitations on the UCA radius.

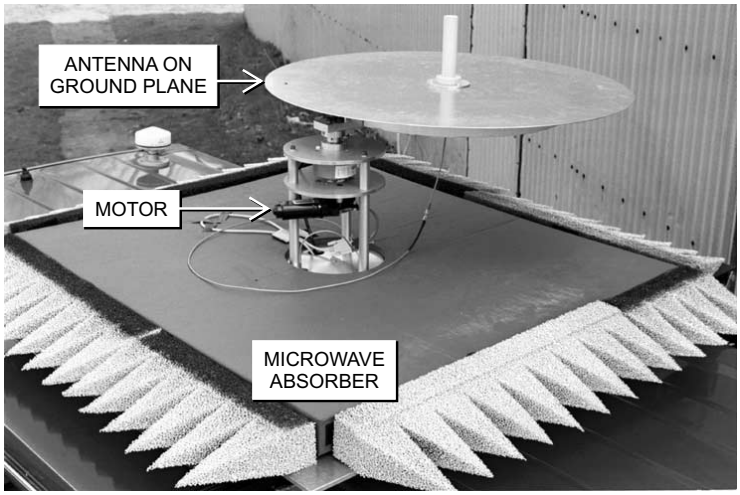

(a)

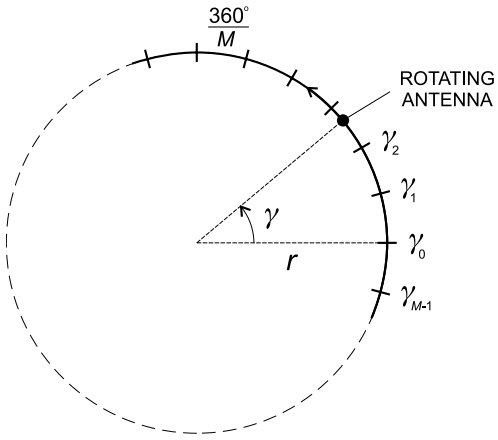

(b)

Fig. 2.2: Synthetic uniform circular array. (a) Photograph of the rotating antenna on the vehicle roof. (b) Diagram of the antenna array.

In the preparation of the experiments various array dimensions were tried out, and a UCA radius of 30 cm, which is approximately two times the wavelength, was found to be a good compromise between the above factors.

Although the transmitter and receiver oscillators are locked to very precise frequency standards, in general there is a slow drift of the measured phase due to inevitable frequency differences. This phase drift must be compensated before the measured data can be further processed. To this end, the channel response is measured during two consecutive cycles of the rotating antenna, and the phase drift is estimated from the average phase difference $\Delta\phi_d$ between the second and the first cycle. This is done for a fixed delay instant, usually the one corresponding with the highest peak in the average power delay profile. The measured phase is then corrected by multiplication of the array outputs by the phase factors $\exp(-jm\Delta\phi_d/M)$, $m = 0, 1, \ldots, M-1$. Experience with the channel sounding systems described in this section has shown that the oscillators' relative frequency offset can easily be tuned to within 2×10^{-10}, which corresponds to a frequency difference of approximately 0.4 Hz at 1900 and 2000 MHz.

A point should be noted regarding the assumed (physical) channel stationarity during the measurements. In actual mobile environments, complete channel stationarity is impossible to achieve, which is principally due to movements of vegetation such as trees caused by wind, and passing vehicles. In the present study, attention is focused on the influence of *constant* features of microcell environments rather than the effects of moving objects, which are only considered here because they form a disturbing factor during measurements. Wind effects were largely avoided by measuring only on days with little or no wind. The disturbances caused by moving traffic, which typically last several seconds, were diminished by means of averaging many measurements taken over several minutes of time. This averaging over many measurements ("snapshots") is inherent to subspace-based angular superresolution methods such as UCA-MUSIC, as will be discussed in Section 2.4.

2.2.3 Antennas

Considerable attention was paid to the choice of the antennas. At the receiver end a 2-dBi sleeve monopole antenna with an omnidirectional radiation pattern in the azimuth plane was used. The bandwidth of this antenna, defined with respect to the voltage standing wave ratio (VSWR), extends from 1700 to 2000 MHz.

In the estimation of elevation angles with a UCA, there exists a twofold ambiguity with respect to waves coming from the upper and the lower hemisphere, as is the case for any type of planar array. Since multipath contributions incident on the array from below the plane of the array – which are likely to be the result of scattering from the measurement vehicle or other objects near the antenna that do not form part of

the propagation environment under study – are of little or no interest, it is desirable for the receiving antenna to have reduced sensitivity for negative elevation angles. In the literature on outdoor AOA measurements with a mobile receiver it is sometimes assumed that the metal roof of the vehicle makes the receiving antenna insensitive to waves arriving from below the horizontal plane of the synthetic array [9]. In reality however, these disturbing multipaths will not be completely blocked, due to diffraction by the edges of the vehicle roof. Waves diffracted at the roof edges also result in distortion of the azimuthal symmetry of the radiation pattern of the receiving antenna. To minimise the antenna's interaction with the vehicle roof, it was placed over a circular, conducting ground plane with diameter $D = 5\lambda$ (view Fig. 2.2(a)). Here, λ denotes the wavelength. The measured azimuth and elevation patterns of this antenna configuration are shown in Fig. 2.3.

At the transmitter end, for the various experiments conducted in the course of the present study several types of directive antennas were used to exploit the full dynamic range of the channel sounding system even in situations with high path loss.

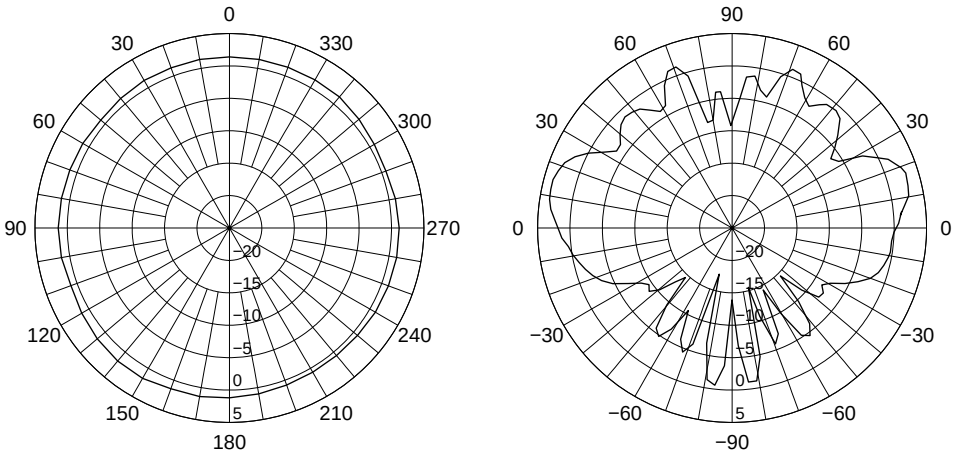

(a) (b)

Fig. 2.3: Measured radiation patterns of the receiving antenna with ground plane ($D/\lambda = 5$). (a) Azimuth pattern (H-plane). (b) Elevation pattern (E-plane).

2.3 Data model

In the considered data model, the PN sounding signal $a(t)$ has a period T, and the bit duration is T_c. The electromagnetic field around the mobile unit is assumed to be composed of N plane-wave multipath contributions arriving from different angles. The mobile is equipped with a UCA of radius r consisting of M vertically polarised antenna elements with an omnidirectional azimuth pattern (as in Fig. 2.3(a)). In complex baseband notation, the signal $y_m(\tau_i)$, $i = 0, 1, 2, \ldots$, at the correlator output corresponding with the mth antenna element ($m = 0, 1, \ldots, M-1$) can then be written as

$$y_m(\tau_i) = \sum_{n=1}^{N} c_n g(\zeta_n) e^{j\zeta_n \cos(\varphi_n - \gamma_m)} x(\tau_i - T_n) + \eta_m(\tau_i), \tag{2.2}$$

with $\tau_i = iT_c + \Delta\tau$, $\Delta\tau$ being a random delay offset with uniform probability density on the interval $0 < \Delta\tau < T_c$. The interval $(iT_c, (i+1)T_c)$ will be referred to as the ith delay interval or delay bin, as shown in Fig. 2.4. In the above expression, $\gamma_m = 2\pi m/M$ is the azimuth of the mth antenna element (view Fig. 2.2), c_n and T_n are the complex amplitude and the relative delay of the nth multipath wave, respectively, φ_n is its azimuth angle, and $\zeta_n = 2\pi r \cos(\vartheta_n)/\lambda$ represents the elevation dependence. Here, ϑ_n is the elevation of the nth wave. Further, $g(\zeta)$ is the elevation amplitude pattern of the array elements (which can be obtained from Fig. 2.3(b)), $x(\tau)$ is the autocorrelation function of the applied PN sequence (defined in (2.1)), and $\eta_m(\tau)$ is an additive white Gaussian noise signal.

The variable delay offset $\Delta\tau$ is realised as follows. In the Ericsson system it is controlled manually, by means of the delay unit shown in Fig. 2.1(b). In the course of a series of measurements, $\Delta\tau$ is varied evenly in the range from 0 to 20 ns, but during each measurement its value is fixed. In experiments conducted with the TU/e system, each measured CIR, which is sampled at 4 samples per bit, is decomposed into four CIRs sampled at 1 sample per bit. Thus, during a single cycle of the rotating antenna, four sets of array output data – with delay offsets $\Delta\tau = 0, 0.25T_c, 0.5T_c$ and $0.75T_c$ – are obtained. The actual probability distribution of $\Delta\tau$ is, obviously, not perfectly uniform. However, for the considered application a uniform probability density function forms a sufficiently accurate model.

The autocorrelation function $x(\tau)$ is a periodic function which consists of triangular peaks with a base width of $2T_c$, and has a negligible, constant value (54 dB below the peak values) in between, as illustrated in Fig. 2.4. In expression (2.2), the time in which the radiowaves travel across the array is assumed to be negligible compared with the bit period T_c (narrowband array assumption). Also, the effects of the limited bandwidth of the channel sounding system are neglected. For later

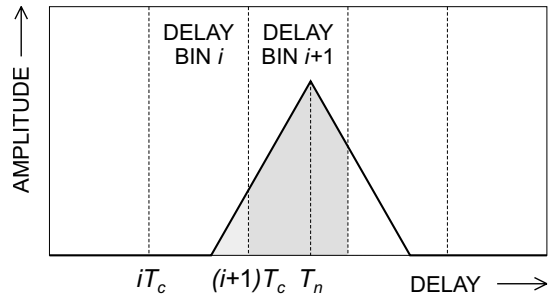

Fig. 2.4: Example of the correlation signal due to a multipath with delay T_n. Each multipath wave contributes to at most three consecutive delay bins.

use and for notational convenience a parameter θ, which represents the AOA of a multipath in terms of both azimuth and elevation, is defined as

$$\theta = \zeta e^{j\varphi}. \tag{2.3}$$

Due to the limited width of the autocorrelation function $x(\tau)$ each received multipath wave contributes to at most three consecutive delay bins, and its contributions to the other delay bins are negligible (view Fig. 2.4). When all $N - N^{(i)}$ negligible contributions to the ith delay bin are omitted, the expression (2.2) can be rewritten as

$$y_m(\tau_i) = \sum_{n=1}^{N^{(i)}} c_n^{(i)} g(\zeta_n^{(i)}) e^{j\zeta_n^{(i)} \cos(\varphi_n^{(i)} - \gamma_m)} x(\tau_i - T_n^{(i)}) + \eta_m(\tau_i), \tag{2.4}$$

where $c_n^{(i)}$, $T_n^{(i)}$, $\varphi_n^{(i)}$ and $\zeta_n^{(i)}$ are the re-indexed amplitudes, delays, azimuth angles and elevation dependences, respectively, of the $N^{(i)} \leq N$ non-negligible multipath signals contributing to the ith delay interval.

In vector notation, the UCA response at the ith delay instant is given by

$$\begin{aligned} \mathbf{y}(\tau_i) &= \left[y_0(\tau_i), y_1(\tau_i), \ldots, y_{M-1}(\tau_i) \right]^T \\ &= \sum_{n=1}^{N^{(i)}} \mathbf{u}(\theta_n^{(i)}) s_n^{(i)}(\tau_i) + \boldsymbol{\eta}(\tau_i), \end{aligned} \tag{2.5}$$

where $s_n^{(i)}(\tau_i) = c_n^{(i)} g(\zeta_n^{(i)}) x(\tau_i - T_n^{(i)})$,

$$\mathbf{u}(\theta) = \left[e^{j\zeta \cos(\varphi - \gamma_0)}, e^{j\zeta \cos(\varphi - \gamma_1)}, \ldots, e^{j\zeta \cos(\varphi - \gamma_{M-1})} \right]^T \tag{2.6}$$

represents the array steering vector in the direction represented by θ, and

$$\boldsymbol{\eta}(\tau_i) = \left[\eta_0(\tau_i), \eta_1(\tau_i), \ldots, \eta_{M-1}(\tau_i)\right]^T \tag{2.7}$$

contains the noise signals at the array elements. In the above expressions, the superscript "T" denotes transpose. In matrix notation, (2.5) is rewritten as

$$\mathbf{y}(\tau_i) = \mathbf{U}^{(i)}\mathbf{s}^{(i)}(\tau_i) + \boldsymbol{\eta}(\tau_i), \tag{2.8}$$

where

$$\begin{aligned} \mathbf{U}^{(i)} &= \left[\mathbf{u}(\theta_1^{(i)}), \mathbf{u}(\theta_2^{(i)}), \ldots, \mathbf{u}(\theta_{N^{(i)}}^{(i)})\right], \\ \mathbf{s}^{(i)}(\tau_i) &= \left[s_1^{(i)}(\tau_i), s_2^{(i)}(\tau_i), \ldots, s_{N^{(i)}}^{(i)}(\tau_i)\right]^T. \end{aligned} \tag{2.9}$$

The noise at each array element is assumed to be uncorrelated with the signals and the noise at the other elements, and also to have zero mean and variance σ^2.

2.4 Angular superresolution

In conventional beamforming [17], the array element output signals are phase-shifted and combined in such a way that they add up coherently for a given direction. Expressed in terms of a vector inner product, the beamformer response $R(\theta'; \tau_i)$ in the steering direction represented by θ', at delay instant τ_i, is written as

$$R(\theta'; \tau_i) = \mathbf{u}^\dagger(\theta')\mathbf{y}(\tau_i) = M\sum_{n=1}^{N^{(i)}} D(\theta_n^{(i)}; \theta')s_n^{(i)}(\tau_i) + \mathbf{u}^\dagger(\theta')\boldsymbol{\eta}(\tau_i), \tag{2.10}$$

where $D(\theta; \theta') = \mathbf{u}^\dagger(\theta')\mathbf{u}(\theta)/M$ represents the normalised array factor of a UCA with the main beam steered in the direction θ'. The superscript "$\dagger$" denotes conjugate transpose. Using a series representation of $e^{\pm j\zeta\cos\varphi}$, given by [18]

$$e^{\pm j\zeta\cos\varphi} = \sum_{h=-\infty}^{\infty} (\pm j)^h J_h(\zeta)e^{jh\varphi}, \tag{2.11}$$

and Graf's addition theorem for Bessel functions [19], it can be shown that

$$D(\theta; \theta') = J_0\left(\left|\theta - \theta'\right|\right), \tag{2.12}$$

provided that $M \gg \min(\zeta, \zeta')$. Here, $J_h(\cdot)$ denotes the Bessel function of the first kind of order h. The array factor $D(\theta; \theta')$ is plotted in Fig. 2.5.

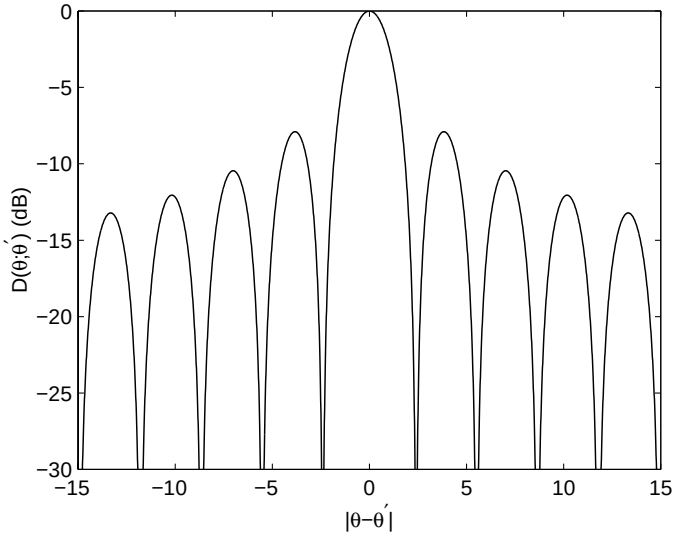

Fig. 2.5: Normalised UCA array factor $D(\theta;\theta')$.

The half-power beamwidth (HPBW) of an antenna (array) is normally defined in a specified radiation pattern cut as the angle between the two directions in which the directivity is one-half the maximum value. Let us define the angular separation between two directions (φ_1, ζ_1) and (φ_2, ζ_2) in the complex θ-plane as the distance $\Delta\theta = |\theta_1 - \theta_2|$ between the corresponding θ_1 and θ_2. Then, it is seen from (2.12) that the HPBW of the array, expressed in $\Delta\theta$, is constant over the entire field-of-view. From Fig. 2.5, it is also seen that conventional beamforming with a UCA results in high sidelobe levels in the array beam pattern. This latter property, together with the objective to obtain high-resolution AOA estimates even with a relatively small UCA radius, forms the rationale behind the choice for a superresolution algorithm for AOA estimation, named UCA-MUSIC, which will be discussed in the remainder of this section.

Angular superresolution techniques such as MUSIC are well-known to offer a significantly better resolution performance than conventional beamformers, of which the resolution is generally limited by the array's HPBW. This resolution enhancement stems from (a) the additional information obtained by multiple spatial sampling of the incoming wavefront, and (b) the additional assumptions made about the incident signals, such as the assumption that the total field consists of a finite and known number of plane waves [20]. In general, the more specialised the assumptions, the better is the superresolution which is achieved if the underlying model is

conformed to by the measured data. For a general review of superresolution AOA estimation algorithms, including their performance, sensitivity and limitations, the reader is referred to [17, 20, 21].

2.4.1 Beamspace processing

The elements of the vector $\mathbf{u}(\theta)$ may be thought of as samples of the signal

$$u(\gamma, \theta) = e^{j\zeta \cos(\varphi - \gamma)}, \tag{2.13}$$

which is periodic in γ with period 2π and can therefore be represented by the Fourier series [19]

$$u(\gamma, \theta) = \sum_{h=-\infty}^{\infty} j^{|h|} a_h(\theta) e^{-jh\gamma}, \tag{2.14}$$

of which the coefficients $a_h(\theta)$ – which have the same magnitudes as, but are not equal to the Fourier coefficients $j^{|h|}a_h(\theta)$ – are found using (2.11) as

$$a_h(\theta) = J_{|h|}(\zeta) e^{jh\varphi}. \tag{2.15}$$

Although the spectral width of the signal $u(\gamma, \theta)$ is infinite in theory, the magnitudes $J_{|h|}(\zeta)$ of the Fourier coefficients decrease fast for $|h| > \zeta$, and are in fact bounded by [13]

$$|J_{|h|}(\zeta)| \leq \left(\frac{\zeta e}{2|h|}\right)^{|h|} \leq \left(\frac{\pi r e}{\lambda |h|}\right)^{|h|}, \quad h \neq 0, \tag{2.16}$$

where e, as before, is a constant with the value $2.71828\ldots$. For sufficiently large $|h|$, the coefficients $a_h(\theta)$ for which $|h| > \pi re/\lambda$ become negligibly small. Aliasing can hence be avoided by choosing the number of array elements (the spatial sample frequency) $M > 2\pi re/\lambda$, and we are only interested in the non-negligible coefficients $a_h(\theta)$, $-H \leq h \leq H$, with $H = \lfloor \pi re/\lambda \rfloor$, where $\lfloor \cdot \rfloor$ is the largest integer smaller than the argument (entier function). Note that in the present case ($r = 0.30$ m, $\lambda \simeq 0.15$ m and $M = 106$ or $M = 157$), the above condition is well satisfied.

A unit-norm vector of coefficients

$$\mathbf{a}(\theta) = \left[a_{-H}(\theta), \ldots, a_0(\theta), \ldots, a_H(\theta)\right]^T \tag{2.17}$$

can be obtained directly from $\mathbf{u}(\theta)$ by the transformation

$$\mathbf{a}(\theta) = \frac{1}{\sqrt{M}} \mathbf{C}\mathbf{V}\mathbf{u}(\theta), \tag{2.18}$$

where

$$\begin{aligned}\mathbf{C} &= \operatorname{diag}\left\{j^{-H}, \ldots, j^{0}, \ldots, j^{-H}\right\},\\ \mathbf{V} &= \frac{1}{\sqrt{M}}\left[\mathbf{v}_0, \mathbf{v}_1, \ldots, \mathbf{v}_{M-1}\right],\\ \mathbf{v}_m &= \left[\omega^{-mH}, \ldots, \omega^{0}, \ldots, \omega^{mH}\right]^T,\end{aligned} \tag{2.19}$$

$\omega = \exp(j2\pi/M)$, which is based on the $(2H+1) \times M$ submatrix of the spatial discrete Fourier transform [18, 22]. Multiplication of (2.8) by the matrix $\mathbf{CV}$ yields

$$\mathbf{z}(\tau_i) = \mathbf{CV}\mathbf{y}(\tau_i) = \mathbf{A}^{(i)}\mathbf{s}^{(i)}(\tau_i) + \mathbf{n}(\tau_i), \tag{2.20}$$

where

$$\begin{aligned}\mathbf{A}^{(i)} &= \sqrt{M}\left[\mathbf{a}(\theta_1^{(i)}), \mathbf{a}(\theta_2^{(i)}), \ldots, \mathbf{a}(\theta_{N^{(i)}}^{(i)})\right],\\ \mathbf{n}(\tau_i) &= \mathbf{CV}\boldsymbol{\eta}(\tau_i).\end{aligned} \tag{2.21}$$

Processing of the array measurement data in the spatial frequency domain is referred to as phase mode excitation-based beamspace processing [22] and has important advantages over element space processing, such as reduced sensitivity to noise and modelling errors [17], and the possibility to employ forward/backward averaging [22], as will be discussed in Section 2.4.3.

2.4.2 UCA-MUSIC

The UCA-MUSIC algorithm uses the eigenstructure of the beamspace array output covariance matrix as a basis for AOA estimation. In the present case, covariance matrices are estimated for all time delay intervals $\left(iT_c, (i+1)T_c\right)$, $i = 0, 1, \ldots$, and for each interval UCA-MUSIC provides AOA estimates of the $N^{(i)}$ multipath signals that contribute to the measured channel response. The covariance matrix corresponding to the ith delay bin can be expressed as

$$\mathbf{R}^{(i)} = \mathrm{E}\left\{\mathbf{z}(\tau_i)\mathbf{z}^{\dagger}(\tau_i)\right\} = \mathbf{A}^{(i)}\mathbf{S}^{(i)}\mathbf{A}^{(i)\dagger} + \sigma^2\mathbf{I}, \tag{2.22}$$

where $\mathbf{S}^{(i)} = \left[s_{mn}^{(i)}\right]$ is the signal covariance matrix, of which the elements

$$s_{mn}^{(i)} = \mathrm{E}\left\{s_m^{(i)}(\tau_i)s_n^{(i)\dagger}(\tau_i)\right\} \tag{2.23}$$

represent the temporal correlations between pairs of signals. In the above expressions, $\mathrm{E}\{\cdot\}$ denotes statistical expectation, and in (2.22) use has been made of the fact that $\mathbf{CVV}^{\dagger}\mathbf{C}^{\dagger} = \mathbf{I}$.

Let $\lambda_1^{(i)} \geq \lambda_2^{(i)} \geq \ldots \geq \lambda_L^{(i)}$ denote the $L = 2H + 1$ eigenvalues of $\mathbf{R}^{(i)}$, and $\mathbf{e}_1^{(i)}, \mathbf{e}_2^{(i)}, \ldots, \mathbf{e}_L^{(i)}$ the corresponding normalised eigenvectors. Provided that $\mathbf{S}^{(i)}$ is non-singular, $\mathbf{A}^{(i)}\mathbf{S}^{(i)}\mathbf{A}^{(i)\dagger}$ is of rank $N^{(i)}$, and it follows that $\lambda_l^{(i)} > \sigma^2$, $l = 1, \ldots, N^{(i)}$, and $\lambda_l^{(i)} = \sigma^2$, $l = N^{(i)} + 1, \ldots, L$, as long as $N^{(i)} < L$. Furthermore, $\mathbf{e}_l^{(i)\dagger}\mathbf{a}(\theta_n^{(i)}) = 0$, $l = N^{(i)} + 1, \ldots, L$; $n = 1, \ldots, N^{(i)}$, i.e., the eigenvectors associated with the $L - N^{(i)}$ smallest eigenvalues (spanning the noise subspace) are orthogonal to the space spanned by the $N^{(i)}$ beamspace steering vectors (the signal subspace) [23]. MUSIC-based estimation algorithms exploit this orthogonality property to form a null spectrum, which is in our case given by

$$Q^{(i)}(\theta) = \sum_{l=N^{(i)}+1}^{L} \left|\mathbf{e}_l^{(i)\dagger}\mathbf{a}(\theta)\right|^2 = 1 - \sum_{l=1}^{N^{(i)}} \left|\mathbf{e}_l^{(i)\dagger}\mathbf{a}(\theta)\right|^2. \tag{2.24}$$

A two-dimensional search for the nulls of $Q^{(i)}(\theta)$ over the full field-of-view yields unbiased and zero-variance estimates of the $N^{(i)}$ actual AOAs, regardless of signal-to-noise ratio and angular spacing between the sources. The corresponding signal powers, which are on the main diagonal of the matrix $\mathbf{S}^{(i)}$, are obtained via the least-squares solution to (2.22). Assuming the noise variance to be negligible compared to the signal powers, $\mathbf{S}^{(i)}$ can be found using

$$\mathbf{S}^{(i)} = \left(\mathbf{A}^{(i)\dagger}\mathbf{A}^{(i)}\right)^{-1}\mathbf{A}^{(i)\dagger}\mathbf{R}^{(i)}\mathbf{A}^{(i)}\left(\mathbf{A}^{(i)\dagger}\mathbf{A}^{(i)}\right)^{-1}. \tag{2.25}$$

Note that in practical applications of MUSIC-like estimation algorithms, only estimates of the actual covariance matrix $\mathbf{R}^{(i)}$ are available and it is therefore not possible to obtain unbiased, zero-variance estimates of the AOAs.

2.4.3 Forward/backward averaging

Eigenstructure-based superresolution algorithms such as UCA-MUSIC fail when the signal covariance matrix $\mathbf{S}^{(i)}$ – of which the elements are given by (2.23) – is singular, which occurs when two or more signals are perfectly correlated or coherent, i.e., when at least one of the temporal correlation coefficients

$$\rho_{t,mn}^{(i)} = \frac{s_{mn}^{(i)}}{\mathrm{E}\left\{\left|s_m^{(i)}(\tau_i)\right|\right\}\mathrm{E}\left\{\left|s_n^{(i)}(\tau_i)\right|\right\}}, \quad m > n, \tag{2.26}$$

$\rho_{t,mn}^{(i)} = \rho_{t,nm}^{(i)*}$, $m < n$, lies on the unit circle. The superscript "$*$" denotes complex conjugate. In the present case, signal coherence occurs only when two or more multipaths have exactly the same propagation delay. However, in practice UCA-MUSIC will be less accurate when two or more signals are strongly correlated, i.e.,

when the difference between the delays of two multipaths is very small compared to T_c.

In order to improve the UCA-MUSIC performance in a correlated signals scenario, the covariance matrix $\mathbf{R}^{(i)}$ can be forward/backward (FB) averaged prior to the calculation of its eigenvalues and eigenvectors [22, 24]. The FB averaging technique hinges on the fact that the beamspace array steering vector $\mathbf{a}(\theta)$ is centro-Hermitian, which means that it satisfies $\mathbf{J}\mathbf{a}(\theta) = \mathbf{a}(\theta)^*$, where $\mathbf{J}$ is the reverse permutation matrix[1] [22].

The FB averaged covariance matrix is

$$\tilde{\mathbf{R}}^{(i)} = \frac{1}{2}\left(\mathbf{R}^{(i)} + \mathbf{J}\mathbf{R}^{(i)*}\mathbf{J}\right) = \mathbf{A}^{(i)}\tilde{\mathbf{S}}^{(i)}\mathbf{A}^{(i)\dagger} + \sigma^2\mathbf{I}, \tag{2.27}$$

where

$$\tilde{\mathbf{S}}^{(i)} = \frac{1}{2}\left(\mathbf{S}^{(i)} + \mathbf{S}^{(i)*}\right) \tag{2.28}$$

is the FB averaged signal covariance matrix. The eigenvalues of $\tilde{\mathbf{R}}^{(i)}$ are denoted by $\tilde{\lambda}_1^{(i)} \geq \tilde{\lambda}_2^{(i)} \geq \ldots \geq \tilde{\lambda}_L^{(i)}$ and the corresponding normalised eigenvectors by $\tilde{\mathbf{e}}_1^{(i)}, \tilde{\mathbf{e}}_2^{(i)}, \ldots, \tilde{\mathbf{e}}_L^{(i)}$.

The elements of $\tilde{\mathbf{S}}^{(i)}$ can be expressed in terms of $\tilde{\rho}_{t,mn}^{(i)}$, the effective temporal correlation coefficient after FB averaging, as

$$\tilde{s}_{mn}^{(i)} = \tilde{\rho}_{t,mn}^{(i)}\, \mathrm{E}\left\{\left|s_m^{(i)}(\tau_i)\right|\right\}\, \mathrm{E}\left\{\left|s_n^{(i)}(\tau_i)\right|\right\}. \tag{2.29}$$

The coefficients $\rho_{t,mn}^{(i)}$ and $\tilde{\rho}_{t,mn}^{(i)}$ are related through

$$\tilde{\rho}_{t,mn}^{(i)} = \mathrm{Re}\left\{\rho_{t,mn}^{(i)}\right\} = \left|\rho_{t,mn}^{(i)}\right| \cos(\phi_{mn}^{(i)}), \tag{2.30}$$

where $\phi_{mn}^{(i)}$ represents the phase difference between the signals $s_m^{(i)}(\tau_i)$ and $s_n^{(i)}(\tau_i)$. The result of the FB averaging preprocessing is that the magnitudes of the correlation coefficients $\rho_{t,mn}^{(i)}$, $m \neq n$, are effectively decreased, i.e., the signals are decorrelated. Thus, FB averaging improves the condition of the array output covariance matrix and consequently the performance of the UCA-MUSIC algorithm.

2.4.4 Effects of a finite data set

In practical applications of UCA-MUSIC the covariance matrix $\tilde{\mathbf{R}}^{(i)}$ is estimated from a finite number of beamspace data snapshots $\mathbf{z}(\tau_{i;k})$, with $\tau_{i;k} = \tau_i + \Delta\tau_k$,

[1] The reverse permutation matrix $\mathbf{J} = \left[J_{mn}\right]$ is defined by $J_{mn} = \delta_{m,N-n}$, where N is the dimension of the matrix and δ_{mn} is the Kronecker delta.

$k = 1, 2, \ldots, K$, where $\Delta\tau_k$ is a realisation of the random delay offset $\Delta\tau$. The resulting estimated covariance matrix is

$$\hat{\mathbf{R}}^{(i)} = \frac{1}{2K} \sum_{k=1}^{K} \left(\mathbf{z}(\tau_{i;k}) \mathbf{z}^{\dagger}(\tau_{i;k}) + \mathbf{J}\mathbf{z}^{*}(\tau_{i;k}) \mathbf{z}^{T}(\tau_{i;k}) \mathbf{J} \right), \tag{2.31}$$

with eigenvalues $\hat{\lambda}_1^{(i)} \geq \hat{\lambda}_2^{(i)} \geq \ldots \geq \hat{\lambda}_L^{(i)}$, and corresponding normalised eigenvectors $\hat{\mathbf{e}}_1^{(i)}, \hat{\mathbf{e}}_2^{(i)}, \ldots, \hat{\mathbf{e}}_L^{(i)}$. The estimated null spectrum can be written as

$$\hat{Q}^{(i)}(\theta) = \sum_{l=N^{(i)}+1}^{L} \left| \hat{\mathbf{e}}_l^{(i)\dagger} \mathbf{a}(\theta) \right|^2 = 1 - \sum_{l=1}^{N^{(i)}} \left| \hat{\mathbf{e}}_l^{(i)\dagger} \mathbf{a}(\theta) \right|^2, \tag{2.32}$$

and the AOA estimates are obtained by searching for its $N^{(i)}$ deepest local minima. In general, the estimated matrix $\hat{\mathbf{R}}^{(i)}$ differs from the true FB averaged covariance matrix $\tilde{\mathbf{R}}^{(i)}$, which causes a perturbation of the estimated null spectrum from the true null spectrum. This in turn causes errors in the AOA estimates and limits the capability to discriminate between closely spaced sources (resolution threshold, view Section 2.5).

Another consequence of the estimation of $\tilde{\mathbf{R}}^{(i)}$ from finite data is that the eigenvalues become all different with probability one, so that it is no longer straightforward to estimate the dimensionality of the noise subspace. However, an objective estimate of the number of multipath signals contributing to the considered time delay bin can be obtained by applying certain criteria from information theory such as FB-AIC (Akaike's information criterion) and FB-MDL (minimum description length) [24]. The former scheme was originally proposed by Akaike [25] for application in time series analysis, later used for the estimation of the number of incident signals in array processing [26], and then modified to work correctly when FB averaging is employed [24]. According to the FB-AIC scheme, the number of signals is estimated as the value of $\hat{N}^{(i)}$ that minimises the criterion

$$\mathrm{AIC}(\hat{N}^{(i)}) = -K(M - \hat{N}^{(i)}) \ln \left[\frac{\left(\prod_{l=\hat{N}^{(i)}+1}^{L} \hat{\lambda}_l^{(i)} \right)^{1/(L-\hat{N}^{(i)})}}{\frac{1}{L - \hat{N}^{(i)}} \sum_{l=\hat{N}^{(i)}+1}^{L} \hat{\lambda}_l^{(i)}} \right], \tag{2.33}$$

where ln denotes the natural logarithm. The relative performance of FB-AIC and FB-MDL was investigated in [24, 27] and is also addressed briefly in Section 2.6.2 of this chapter.

2.4.5 Summary of the algorithm

The procedure to obtain high-resolution AOA estimates from a finite number of CIR snapshots $\mathbf{y}(\tau_{i;k})$, $i = 0, 1, \ldots$, $k = 1, 2, \ldots, K$, measured at the elements of a UCA is summarised in the following. It is assumed that the phase drift resulting from the frequency difference between the transmitter and receiver frequency standards has been compensated (cf. Section 2.2.2), and that the impulse response estimates are obtained at the exact positions represented by $\gamma_0, \gamma_1, \ldots, \gamma_{M-1}$.

For each delay interval $\big(iT_c, (i+1)T_c\big)$:

1. form the K beamspace array output vectors $\mathbf{z}(\tau_{i;k}) = \mathbf{C}\mathbf{V}\mathbf{y}(\tau_{i;k})$;
2. form the estimated covariance matrix $\hat{\mathbf{R}}^{(i)}$ according to equation (2.31);
3. compute the L eigenvalues $\hat{\lambda}_l^{(i)}$ and corresponding normalised eigenvectors $\hat{\mathbf{e}}_l^{(i)}$ of $\hat{\mathbf{R}}^{(i)}$, sorted in the order of descending eigenvalues;
4. evaluate the FB-AIC criterion (2.33) for $\hat{N}^{(i)} = 0, 1, \ldots, L-1$, and select the value of $\hat{N}^{(i)}$ that gives the lowest value;
5. using any non-linear minimisation method, find the values of θ in the domain formed by $0 < \varphi < 2\pi$ and $0 < \zeta < 2\pi r/\lambda$ that are associated with the $\hat{N}^{(i)}$ deepest local minima of $\hat{Q}^{(i)}(\theta) = 1 - \sum_{l=1}^{\hat{N}^{(i)}} |\hat{\mathbf{e}}_l^{(i)\dagger}\mathbf{a}(\theta)|^2$ and call them $\theta_1^{(i)}, \theta_2^{(i)}, \ldots, \theta_{\hat{N}^{(i)}}^{(i)}$;
6. reconstruct the matrix $\mathbf{A}^{(i)} = \sqrt{M}\big[\mathbf{a}(\theta_1^{(i)}), \mathbf{a}(\theta_2^{(i)}), \ldots, \mathbf{a}(\theta_{\hat{N}^{(i)}}^{(i)})\big]$;
7. compute the matrix $\hat{\mathbf{S}}^{(i)} = \big(\mathbf{A}^{(i)\dagger}\mathbf{A}^{(i)}\big)^{-1}\mathbf{A}^{(i)\dagger}\hat{\mathbf{R}}^{(i)}\mathbf{A}^{(i)}\big(\mathbf{A}^{(i)\dagger}\mathbf{A}^{(i)}\big)^{-1}$.

The complex values $\theta_n^{(i)}$, $n = 1, 2, \ldots, \hat{N}^{(i)}$ represent the estimated AOAs and the elements on the main diagonal of $\hat{\mathbf{S}}^{(i)}$ are the corresponding estimated signal powers.

2.5 Resolution threshold

The UCA-MUSIC algorithm, like other eigenstructure-based techniques, can exactly determine the AOAs of any two closely spaced sources when the true covariance matrix of the array output data is available. In practice, however, the covariance matrix is estimated from a finite set of snapshots. The deviation between the estimated and the true covariance matrices produces a perturbation of the null spectrum, which in

turn causes biased estimates and limits the capability of the algorithm to discriminate between closely spaced sources. The objective of this section is to derive an expression for the resolution threshold of UCA-MUSIC, which is the signal-to-noise ratio (SNR) below which two closely spaced multipath waves, with equal signal powers P, can no longer be "resolved", i.e. when the null spectrum at either of the two true AOAs, which will be called θ_1 and θ_2, is greater than at the angle $\theta_m = (\theta_1 + \theta_2)/2$ between the true AOAs with more than 50% probability. The notation used in this section is the same as in the previous sections, but, for convenience, the superscripts "(i)" will be omitted.

General expressions for the mean of the MUSIC null spectrum, generated from a FB averaged covariance matrix estimated from finite data, were derived in [28] and later used in [27]. Neglecting terms of order $1/K^2$, the mean null spectrum for two sources is given by

$$\mathrm{E}\{\hat{Q}(\theta)\} = \tilde{Q}(\theta) + \frac{1}{2K}\sum_{l=1}^{2}\frac{\tilde{\lambda}_l\sigma^2}{(\tilde{\lambda}_l - \sigma^2)^2}\left[(L-2)\left|\tilde{\mathbf{e}}_l^{\dagger}\mathbf{a}(\theta)\right|^2 - \tilde{Q}(\theta)\right], \tag{2.34}$$

Here, $\tilde{\lambda}_l$, $\tilde{\mathbf{e}}_l$ and $\tilde{Q}(\theta)$ are the eigenvalues, normalised eigenvectors and null spectrum, respectively, corresponding with the FB averaged ensemble covariance matrix $\tilde{\mathbf{R}}$. The resolution threshold ξ_T is found as the smallest SNR for which the inequality

$$\mathrm{E}\{\hat{Q}(\theta_l)\} \le \mathrm{E}\{\hat{Q}(\theta_m)\}, \quad l = 1, 2 \tag{2.35}$$

is satisfied [27].

With the aid of (2.34) and a derivation similar to that in [27], the expectations in (2.35) can be expressed in terms of the two largest eigenvalues $\tilde{\mu}_l = \tilde{\lambda}_l - \sigma^2$, $l = 1, 2$, of the "noise-free" covariance matrix

$$\begin{aligned}\tilde{\mathbf{S}}\mathbf{A} &= MP\left[\mathbf{a}(\theta_1), \mathbf{a}(\theta_2)\right]\begin{bmatrix}1 & \tilde{\rho}_t\\ \tilde{\rho}_t & 1\end{bmatrix}\left[\mathbf{a}(\theta_1), \mathbf{a}(\theta_2)\right]^{\dagger}\\ &= MP\left[\tilde{\mathbf{e}}_1, \tilde{\mathbf{e}}_2\right]\begin{bmatrix}\tilde{\mu}_1' & 0\\ 0 & \tilde{\mu}_2'\end{bmatrix}\left[\tilde{\mathbf{e}}_1, \tilde{\mathbf{e}}_2\right]^{\dagger},\end{aligned} \tag{2.36}$$

in which $\tilde{\rho}_t = \tilde{\rho}_{t,12}$ denotes the temporal correlation between the two signals after FB averaging (cf. Section 2.4.3) and $\tilde{\mu}_l' = \tilde{\mu}_l/MP$. This yields

$$\mathrm{E}\{\hat{Q}(\theta_l)\} = \frac{L-2}{2K}\left\{-\frac{1}{M^2\xi^2\tilde{\mu}_1'\tilde{\mu}_2'} + \frac{1-\rho_s^2}{M\xi\tilde{\mu}_1'\tilde{\mu}_2'}\left[1 + \frac{\tilde{\mu}_1' + \tilde{\mu}_2'}{M\xi\tilde{\mu}_1'\tilde{\mu}_2'}\right]\right\}, \quad l = 1, 2, \tag{2.37}$$

and

$$\begin{aligned}\mathrm{E}\big\{\hat{Q}(\theta_m)\big\} =& \tilde{Q}(\theta_m) + \frac{L-2}{2K}\Bigg\{\frac{(\tilde{\mu}_1' + \tilde{\mu}_2') - 2\rho_m^2(1+\tilde{\rho}_t)}{M\xi\tilde{\mu}_1'\tilde{\mu}_2'} \\ &+ \frac{(\tilde{\mu}_1'^2 + \tilde{\mu}_1'\tilde{\mu}_2' + \tilde{\mu}_2'^2) - 2\rho_m^2(1+\tilde{\rho}_t)(\tilde{\mu}_1' + \tilde{\mu}_2')}{M^2\xi^2\tilde{\mu}_1'^2\tilde{\mu}_2'^2}\Bigg\},\end{aligned} \tag{2.38}$$

where $\xi = P/\sigma^2$ is the SNR of each of the signals, $\rho_s = \mathbf{a}^\dagger(\theta_1)\mathbf{a}(\theta_2)$ is the spatial correlation between the sources, and $\rho_m = \mathbf{a}^\dagger(\theta_1)\mathbf{a}(\theta_m) = \mathbf{a}^\dagger(\theta_2)\mathbf{a}(\theta_m)$ is the spatial correlation between either one of the sources and a wave arriving from the direction corresponding with θ_m. By using Graf's addition theorem for Bessel functions [19], it can be shown that

$$\rho_s = J_0(\Delta\theta) \quad \text{and} \quad \rho_m = J_0(\Delta\theta/2), \tag{2.39}$$

where $\Delta\theta = |\theta_1 - \theta_2|$ denotes the difference between the "angles" θ_1 and θ_2.

The resolution threshold ξ_T is obtained by solving the quadratic equation that results after equating (2.37) and (2.38). Using a derivation similar to that in [28], it follows from equation (2.36) that

$$\tilde{\mu}_l' = 1 + \rho_s\tilde{\rho}_t \pm \big|\rho_s + \tilde{\rho}_t\big|, \;\; l = 1, 2. \tag{2.40}$$

This leads to the following closed-form expression for ξ_T:

$$\xi_T = \frac{L-2}{4KM\tilde{Q}(\theta_m)}A\left\{1 + \sqrt{1 + \frac{8K\tilde{Q}(\theta_m)}{L-2}B}\right\}, \tag{2.41}$$

where A and B are given by

$$A = \frac{(1-\rho_s^2) + 2\rho_m^2(1+\tilde{\rho}_t) - 2(1+\rho_s\tilde{\rho}_t)\big[1 - \tilde{Q}(\theta_m)\big]}{(1-\rho_s^2)(1-\tilde{\rho}_t^2)}, \tag{2.42}$$

$$B = \frac{2(1+\rho_s\tilde{\rho}_t)}{(1-\rho_s^2) + 2\rho_m^2(1+\tilde{\rho}_t) - 2(1+\rho_s\tilde{\rho}_t)\big[1 - \tilde{Q}(\theta_m)\big]}. \tag{2.43}$$

Note from (2.41) that the resolution threshold is inversely proportional to K, the number of snapshots, and reduces to zero for $K \to \infty$. This means that resolution is always achieved if the true covariance matrix is exactly known, regardless of the SNR or the spacing between the AOAs.

For the evaluation of the null spectrum height $\tilde{Q}(\theta_m)$, use is made of the following expression for the normalised eigenvectors:

$$\tilde{\mathbf{e}}_l = \frac{\mathbf{a}(\theta_1) \pm \mathbf{a}(\theta_2)}{\big|\mathbf{a}(\theta_1) \pm \mathbf{a}(\theta_2)\big|}, \;\; l = 1, 2, \tag{2.44}$$

which, again, is obtained from a derivation similar to that in [28]. This yields

$$\tilde{Q}(\theta_m) = 1 - \left|\tilde{\mathbf{e}}_1 \mathbf{a}(\theta_m)\right|^2 - \left|\tilde{\mathbf{e}}_2 \mathbf{a}(\theta_m)\right|^2 = 1 - \frac{2\rho_m^2}{1+\rho_s}. \tag{2.45}$$

The resolution threshold for two sources of equal power, as derived here for the special case of a UCA, is a very useful performance parameter for AOA estimation algorithms, and is often used in the published literature. It should be noted, however, that the superposition principle does not hold for non-linear superresolution algorithms such as UCA-MUSIC. One must therefore be very careful in extrapolating results obtained from (2.41) to a larger number of sources or to other more general cases.

2.6 Numerical results

Computer simulations of the performance of the UCA-MUSIC algorithm and the effect of FB averaging preprocessing are presented in this section. As in the previous section, the superscripts "(i)" are omitted.

2.6.1 Resolution threshold

First, simulations are shown of the resolution threshold ξ_T for two equipowered multipath signals, for which a theoretical expression was derived in the previous section. Fig. 2.6 shows simulated and theoretical values of ξ_T, as a function of the angular spacing $\Delta\theta = |\theta_2 - \theta_1|$, and for different propagation delay differences $\Delta T = T_2 - T_1$. In the simulation, the considered delay interval is the zeroth bin $(0, T_c)$, the AOAs of the multipath components are equal to $\theta_{1,2} = \pm\Delta\theta/2$, $\Delta\theta$ being a real number, their delay times are $T_{1,2} = (T_c \pm \Delta T)/2$, and their SNRs are

$$\xi_n = \frac{\mathrm{E}\left\{\left|s_n(\tau_i)\right|^2\right\}}{\sigma^2} = \frac{1}{\sigma^2 T_c}\int_0^{T_c} \left|s_n(\tau_i)\right|^2 d\tau, \quad n = 1, 2. \tag{2.46}$$

The simulated noise was produced by a pseudorandom normal number generator. The number of snapshots was taken to be $K = 20$, and all other parameters were chosen the same as for the Ericsson measurement system described in Section 2.2 ($M = 106$, $T_c = 20$ ns). Each of the simulated threshold values in Fig. 2.6 is based on 50 independent trials.

The theoretical and simulated results presented in Fig. 2.6 show reasonable to good agreement. As expected, the resolution capability of UCA-MUSIC is observed to decrease with decreasing ΔT (and hence increasing signal correlation). With FB averaging however, the signal correlation is effectively reduced and the performance

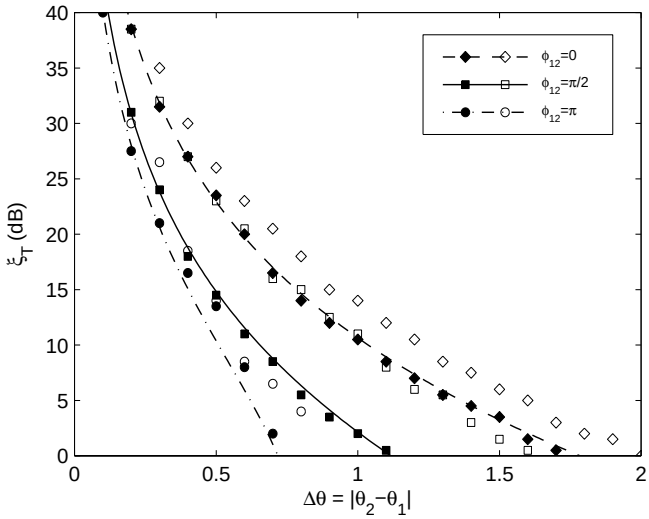

(a)

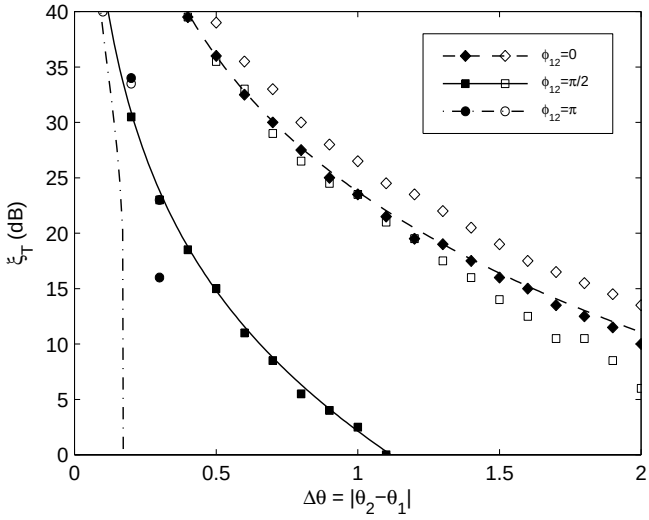

(b)

Fig. 2.6: Theoretical and simulated resolution thresholds, for propagation delay differences (a) $\Delta T = 0.5T_c$ and (b) $\Delta T = 0.1T_c$. $M = 106$, $K = 20$, $T_c = 20$ ns. "Closed" markers correspond with FB averaging; "open" markers represent performance without FB averaging. Simulated thresholds are based on 50 independent trials.

degradation is therefore only limited, except when the phase difference ϕ_{12} between the signals is either 0 or π. The small improvements due to FB averaging for $\phi_{12} = 0$ and $\phi_{12} = \pi$ that can still be seen in Fig. 2.6 are the result of the fact that this scheme effectively doubles the number of snapshots [24]. Because the array's directional properties are uniform in the complex θ-plane, the above results are representative of the resolution capability over the entire field-of-view. Also, they are independent of the array radius r and the wavelength λ, which are both included in the definition of θ (view Section 2.3).

In comparison with conventional beamforming, of which the capability to resolve two equipowered waves is generally limited by the array HPBW ($\Delta\theta_{-3\text{dB}} \simeq 2.2$, cf. Fig. 2.5), the resolution performance of UCA-MUSIC is considerably better – except in the exceptional case of weak, highly correlated signals with a phase difference near 0 or π.

2.6.2 Estimation of the number of signals

In addition to the foregoing resolution considerations, simulations were made to illustrate how poor estimates of the number of paths N impact the UCA-MUSIC null spectrum and the AOA estimation. To this end, a scenario with five incident multipath waves was simulated, with the parameters given in Table 2.2. The signal phases ϕ_n and delays T_n were chosen randomly. Fig. 2.7(a)-(c) show the null spectrum for $\hat{N} = 4, 5$ and 8, respectively. The corresponding estimated AOAs and SNRs are given in the table.

From Fig. 2.7 it is observed that a modest under- or overestimation of N does not lead to dramatic changes of the null spectrum. Increasing underestimation of N generally leads to shallower local minima, and ultimately to the vanishing of the local minima corresponding with the weakest multipath waves. A modest overestimation of N introduces spurious local minima which, however, hardly alter the positions of the deeper nulls corresponding with the true AOAs. Table 2.2 shows that the estimated signal powers of the falsely detected waves are all around or below the noise level, and therefore insignificant in comparison with the dominant multipath signals which are of primary interest. From these observations it is concluded that it is better to tolerate a small overestimation of N than to underestimate the number of incident waves, which would lead to undetected multipath contributions. Of the available objective criteria for detecting the number of sources from a FB averaged covariance matrix, FB-AIC and FB-MDL [24], the former scheme provides slightly higher estimates of N for a small number of snapshots. Furthermore, for the scenario considered in [27], this scheme was shown to offer the highest probability of correctly detecting the number of waves for small values of K.

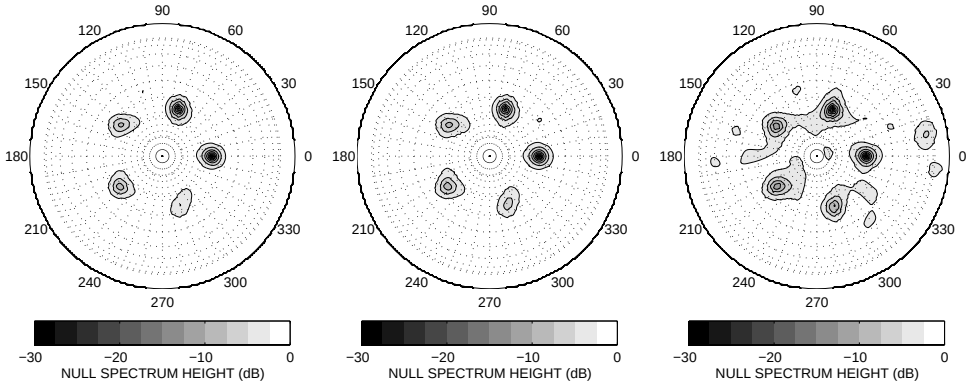

(a) (b) (c)

Fig. 2.7: UCA-MUSIC null spectra $\hat{Q}(\theta)$ for the simulated scenario. (a) $\hat{N} = 4$. (b) $\hat{N} = 5$. (c) $\hat{N} = 8$. Dotted lines are drawn every ten degrees azimuth and elevation (outer perimeter corresponds with $\vartheta = 0^{\mathrm{o}}$; center dot corresponds with $\vartheta = \pm 90^{\mathrm{o}}$).

Table 2.2: Theoretical and estimated multipath parameters.

n	theoretical			$\hat{N} = 4$		
	φ (deg)	ζ (rad)	ξ (dB)	φ (deg)	ζ (rad)	ξ (dB)
1	0.0	5.00	30.0	-0.3	4.99	30.5
2	+72.0	5.00	25.0	+71.1	5.02	25.5
3	+144.0	5.00	20.0	+143.0	5.24	20.9
4	-144.0	5.00	15.0	-144.2	5.28	15.7
5	-72.0	5.00	10.0	–	–	–

n	$\hat{N} = 5$			$\hat{N} = 8$		
	φ (deg)	ζ (rad)	ξ (dB)	φ (deg)	ζ (rad)	ξ (dB)
1	-0.3	4.99	29.6	-0.1	4.98	30.7
2	+71.2	5.01	24.6	+71.4	4.94	25.3
3	+142.6	5.16	19.6	+143.6	5.08	20.0
4	-144.1	5.21	14.8	-142.7	5.03	15.1
5	-68.8	5.17	10.1	-71.2	5.40	11.4
6	–	–	–	+180.0	6.59	-2.9
7	–	–	–	-35.0	6.29	-5.3
8	–	–	–	+11.3	11.26	-7.4

2.7 Experimental results

This section discusses the results of two measurements carried out in a residential area in Leidschendam, The Netherlands, which is characterised by 5-15 m high buildings, scattered vegetation, and low traffic density (view Fig. 2.8). The objective of the measurements was to determine whether the method described in this chapter can be used in real built-up environments to identify the dominant propagation mechanisms. The channel sounding system used was the Ericsson equipment, and the carrier frequency was 1900 MHz. The transmitting antenna was located in a tower at 46 m above ground level, well above the average rooftop level of most other buildings in the area. This was done to prevent "complex" propagation paths, resulting from multiple interactions with the environment, from becoming important. The antenna was a 7.1-dBi vertically polarised double-ridged pyramidal horn antenna with an azimuthal 3-dB beamwidth of 53^{o} and a bandwidth (defined with respect to the VSWR) covering the frequency region from 1 to 18 GHz. During the measurements described in this section, it was pointed south-east. The number of snapshots taken for each measurement was $K = 20$.

Figs. 2.9 and 2.10 show the temporal and angular multipath distributions measured at the two mobile station (MS) locations indicated in Fig. 2.8, together with 360-degree panorama photographs taken from the receiver perspective, which serve as an accurate angular reference. In these figures, the marker size indicates the am-

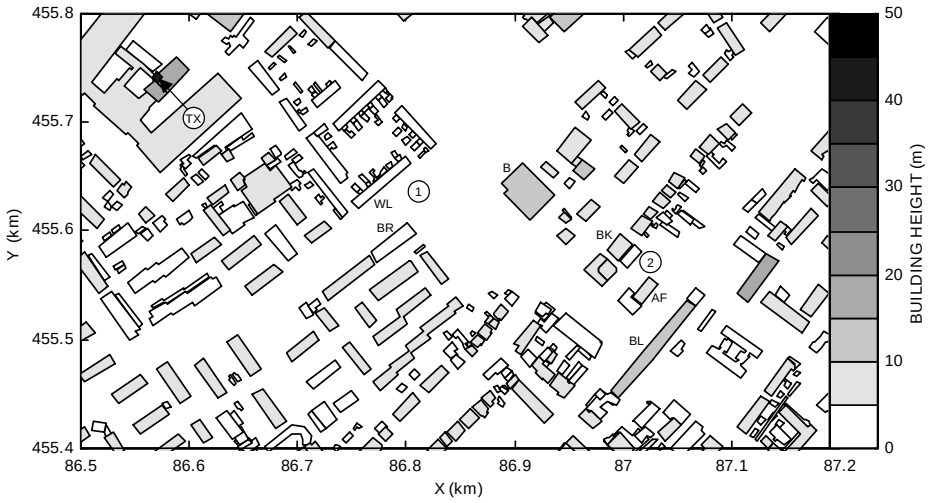

Fig. 2.8: Map of the measurement site. Gray levels indicate building heights.

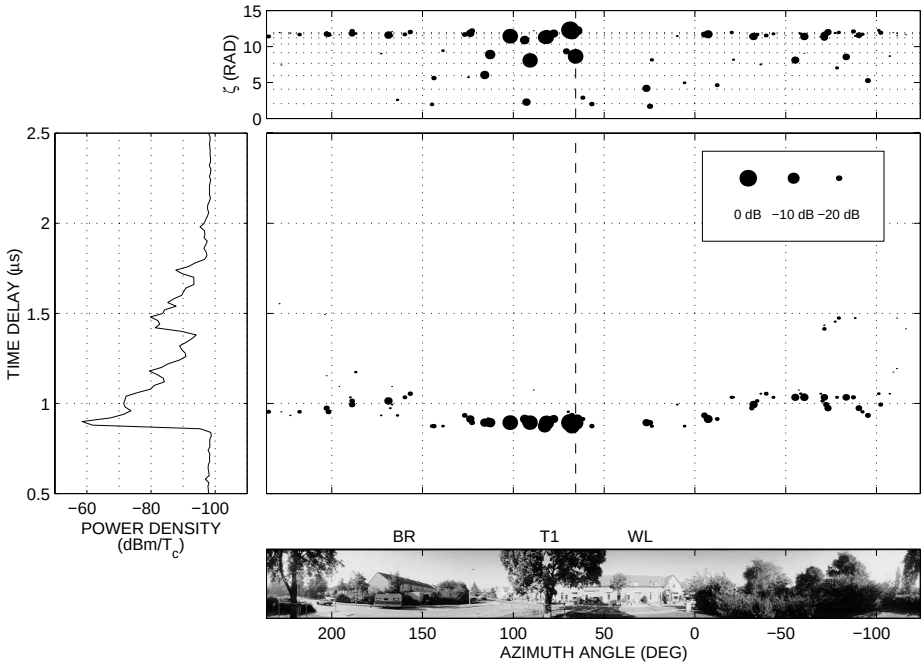

Fig. 2.9: Temporal-angular multipath distribution for MS location 1. Marker size indicates multipath wave amplitude relative to total power (down to -30 dB). BS antenna position is indicated by dashed vertical line.

plitude of each resolved multipath wave relative to the total power (which is obtained by integration of the measured power delay profile), elevation angles are represented through ζ (cf. Section 2.3), and the BS antenna position is indicated by a dashed vertical line. The power delay profile shown in the left box of each figure is the measured local average profile, computed over all antenna positions with respect to power density.

In the first measurement, the MS location (marked as "1" in Fig. 2.8) was chosen such that the direct wave was obstructed by a tree (T1 in Fig. 2.9). Scattering and absorption of the wave incident on the tree's canopy result in an attenuation of 13 dB over the free-space loss (although this is not shown here), and a considerable angular spread. The second peak in the measured power delay profile is due to the radiowaves scattered from vegetation surrounding the MS ($-160^{\circ} < \varphi < 0^{\circ}$), which was directly illuminated by the BS antenna. The relatively weak contribution with delay $\tau \simeq 1.5\,\mu$s is the result of reflection and diffraction from the building B, which is behind the vegetation.

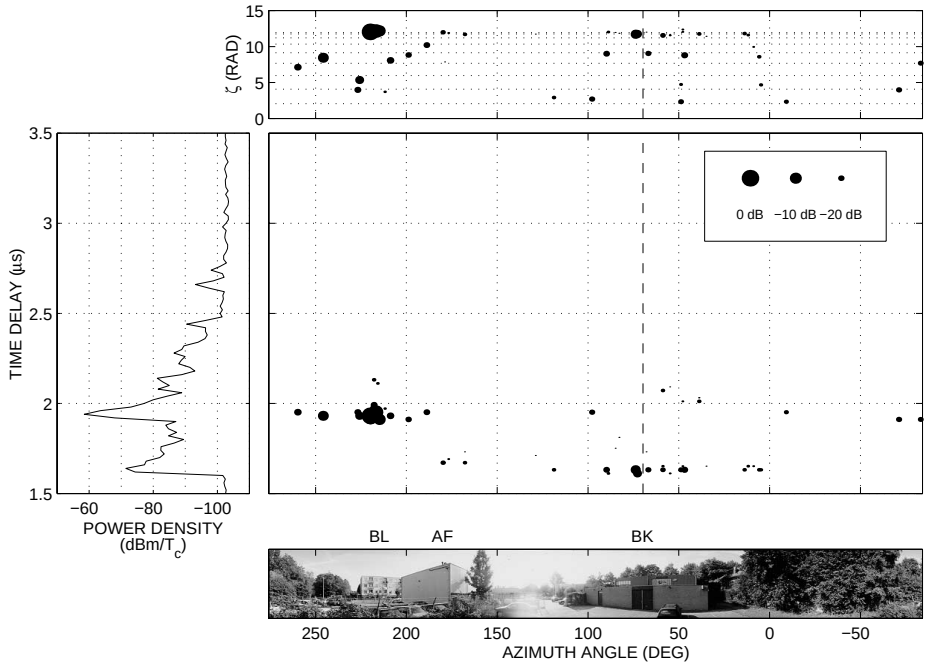

Fig. 2.10: Temporal-angular multipath distribution for MS location 2. Marker size indicates multipath wave amplitude relative to total power (down to -30 dB). BS antenna position is indicated by dashed vertical line.

In the second measurement, the MS was situated at a car park behind a 6-m-high building (location "2" in Fig. 2.8). Again, the first multipath contributions have a considerable angular spread, which is probably due to the row of trees between the transmitting antenna and the building BK. The diffraction contribution over the rooftop of BK is observed approximately at the expected azimuth angle of 70 degrees. The wave with $\varphi = 213^{o}$ can be identified (on the basis of both AOA and propagation delay) as a reflection from building BL. In this particular case, this reflected wave is the dominant contribution, due to the attenuation of the direct wave by the trees behind BK.

2.8 Conclusions

In this chapter, a method has been proposed to obtain high-resolution AOA estimates of multipath radiowaves using a wideband radio channel sounder and a synthetic uniform circular array. The UCA-MUSIC algorithm and forward/backward averag-

ing were demonstrated to be suitable algorithms for the high-resolution estimation of two-dimensional (azimuth and elevation) AOAs from complex impulse response measurement data obtained with this array configuration. Problems of the algorithm with respect to robustness to noise, which were expected by the authors of [13], were not experienced. The problem of the *a priori* estimation of the number of incident signals based on a finite set of measurement data was solved by applying a modified version of Akaike's information criterion (FB-AIC) [24].

Expressions were derived for the theoretical resolution capability of the UCA-MUSIC algorithm. The achievable angular resolution was shown to depend on a number of factors, including the signal-to-noise ratio, the temporal correlation between the signals and the number of snapshots. Roughly, for the array radius considered in the present work, an azimuthal resolution better than 5 degrees is achievable if $K = 20$ or higher, and if the incidence directions of the incident waves are close to horizontal. For high elevation angles, the resolution capability is relatively poor.

It was demonstrated that the combination of high-resolution AOA estimates and time delay information enables the identification of the dominant multipaths in an actual built-up environment. The determination of the elevation angles of the radiowaves permits one to obtain additional information about the nature of the involved propagation mechanisms.

3

High-resolution angle-of-arrival measurements: results

3.1 Introduction

In the previous chapter, a method was presented for the measurement, with high resolution, of the angle-of-arrival (AOA) of multipath radiowaves. Experimental results obtained in a suburban environment with the base station antenna above the rooftop level were provided to demonstrate the capability of the method to identify the dominant propagation mechanisms in realistic built-up environments. In the framework of a collaboration between the TU/e, KPN and Swisscom (formerly Swiss Telecom PTT), measurements of this type were also carried out in urban environments in Bern and Fribourg, Switzerland, under microcellular conditions, i.e. with the simulated base station antenna under the rooftop level. The objective of these measurements was to verify and possibly improve the accuracy of existing propagation prediction models. In particular, an investigation was made of the dominant propagation mechanisms in urban microcell environments. A selection of the results of these measurements is presented in this chapter. In addition, results are shown of experiments that were conducted later to further investigate the propagation mechanisms identified in the Swiss measurement campaign.

Section 3.2 provides experimental results that identify the transmission of ra-

diowaves through buildings as an important propagation mechanism in configurations where the line-of-sight path is obstructed by a building or a row of buildings. In Section 3.3 it is shown that, under certain circumstances, scattering from trees can play a prominent role. Conclusions are drawn in Section 3.4.

3.2 Transmission through buildings

Most existing deterministic propagation models developed for propagation prediction in urban microcell environments treat the buildings as being opaque, i.e. transmitted field contributions are neglected. In fact, the assumption that the first buildings surrounding the base station antenna obstruct the radiated field, and thus largely confine the signal power to the area enclosed by them, is at the heart of the microcellular concept. In [29], Rizk observed that, for some particular configurations, existing propagation models seriously underestimate the field strength behind the first row of buildings. A possible explanation for this discrepancy is that, contrary to the commonly made assumption mentioned above, the buildings in this scenario were not opaque at UHF frequencies, and were "leaking" a significant portion of the field incident on them. In view of this, it is of interest to obtain a better understanding of the propagation phenomena responsible for the field directly behind buildings, and to investigate whether transmission through buildings is an important one of them.

This section presents results of high-resolution AOA measurements conducted behind a building, or a row of buildings, obstructing the line-of-sight propagation path to the base station antenna. The first of these measurements were carried out in a realistic urban microcell environment in Bern, Switzerland, using the Ericsson channel sounding equipment (view Table 2.1) at 2000 MHz. They are described in Section 3.2.1. Section 3.2.2 discusses an additional AOA measurement, which was conducted in a more "controlled" environment, using the TU/e equipment, at a carrier frequency of 1900 MHz.

3.2.1 Realistic urban microcell environment – Bern

The area in Bern selected for the measurements, which is depicted in Fig. 3.1, is characterised by a relatively regular street pattern, narrow streets (10-15 m) faced by three- to five-storey concrete buildings with irregular faces – primarily caused by balconies and windows. Scattered trees are found in the entire area, as well as parked cars along the curbs. The traffic density in the area is low, except in Rodtmatt Street, which is wider than the other streets in the area. A vertically polarised, 3-dBi, omnidirectional base station antenna was located in the middle of the area, at a height of 5 m. This location is marked as "BS" in Fig. 3.1.

In an earlier study conducted by Swisscom and reported in [29], narrowband

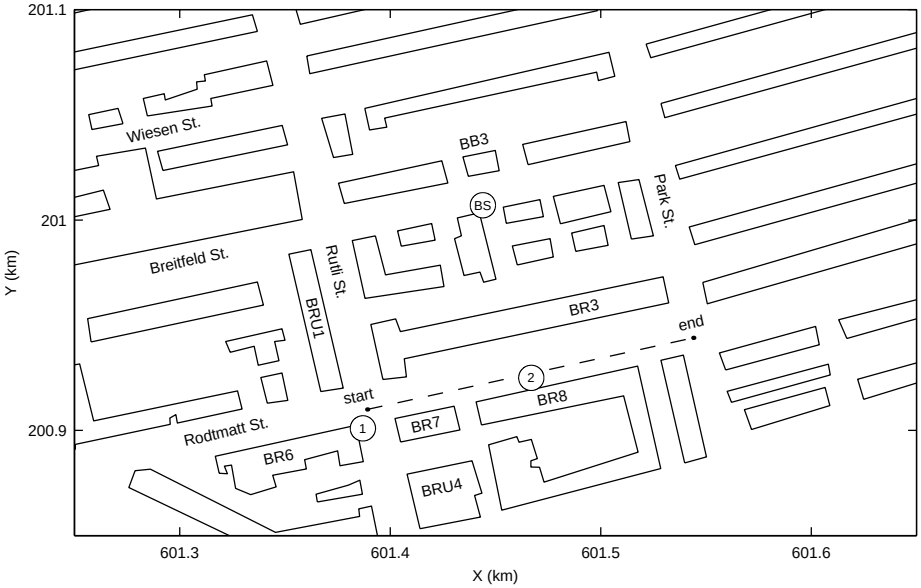

Fig. 3.1: Map of the measurement site in Bern.

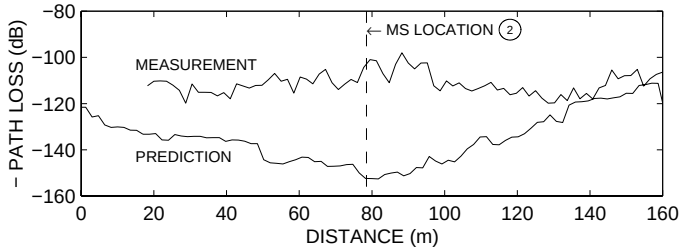

Fig. 3.2: Measured and predicted path loss along the trajectory in Rodtmatt Street.

field measurements were taken along the trajectory in Rodtmatt Street indicated in Fig. 3.1, with almost the same base station configuration. The frequency used for these measurements was 1890 MHz. The measured path loss, averaged over space in order to remove small-scale fading effects, is shown in Fig. 3.2, together with a prediction generated using the ray-tracing model described in [29], which takes into account all combinations of multiple specular reflection, up to order nine, and single diffraction, but not transmission. It is seen that the field strength behind building BR3 is considerably underestimated by the model, especially in the middle part of the trajectory. Near the intersections with Rutli and Park Street, the prediction error

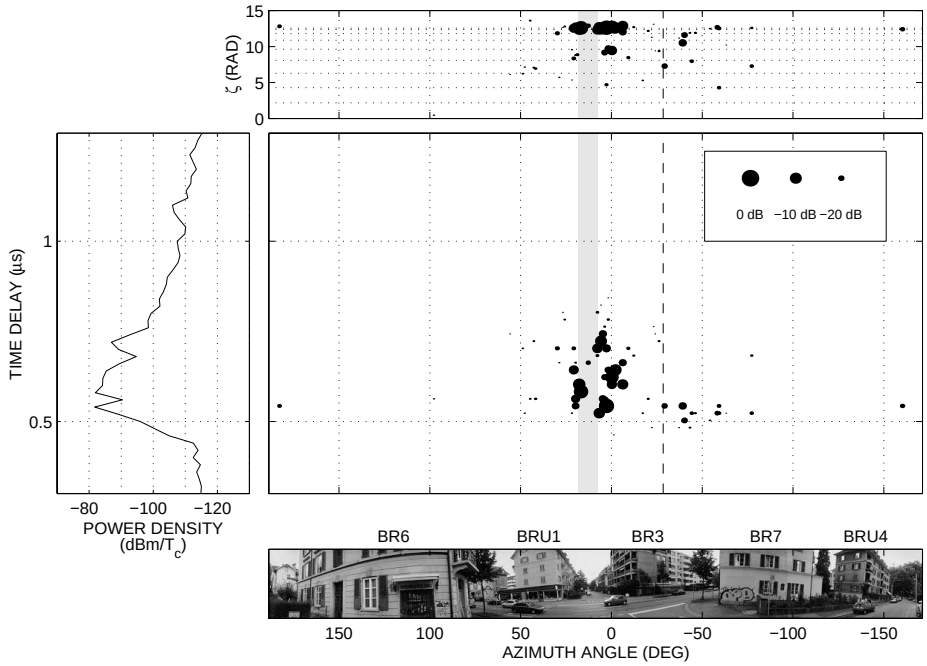

Fig. 3.3: Temporal-angular multipath distribution for MS location 1 in Bern. Marker size indicates multipath wave amplitude relative to total power (down to -30 dB). BS antenna position is indicated by dashed vertical line.

is much smaller.

Measurements were performed at two mobile station (MS) locations – the first near the beginning of the trajectory, where the prediction error is relatively small, and the second somewhere in the middle, where the error is very large. These locations are indicated by “1” and “2” in Fig. 3.1. Figs. 3.3 and 3.4 show the temporal and angular multipath distributions measured at these locations. In these figures, as previously, elevation angles are represented through ζ (cf. Section 2.3), and the base station antenna position is indicated by a dashed vertical line. Furthermore, in these and the following figures, the azimuth regions corresponding to points at the ground level that can be directly “seen” by both the base station and the MS antenna are marked by grey zones. All ray contributions resulting from a single interaction with the environment must arrive from within these regions. Also, rays diffracted from a building corner obstructing the line-of-sight must arrive from the directions represented by the edges of the grey zones.

As can be seen in Fig. 3.3, the received field at MS location 1 is mainly composed

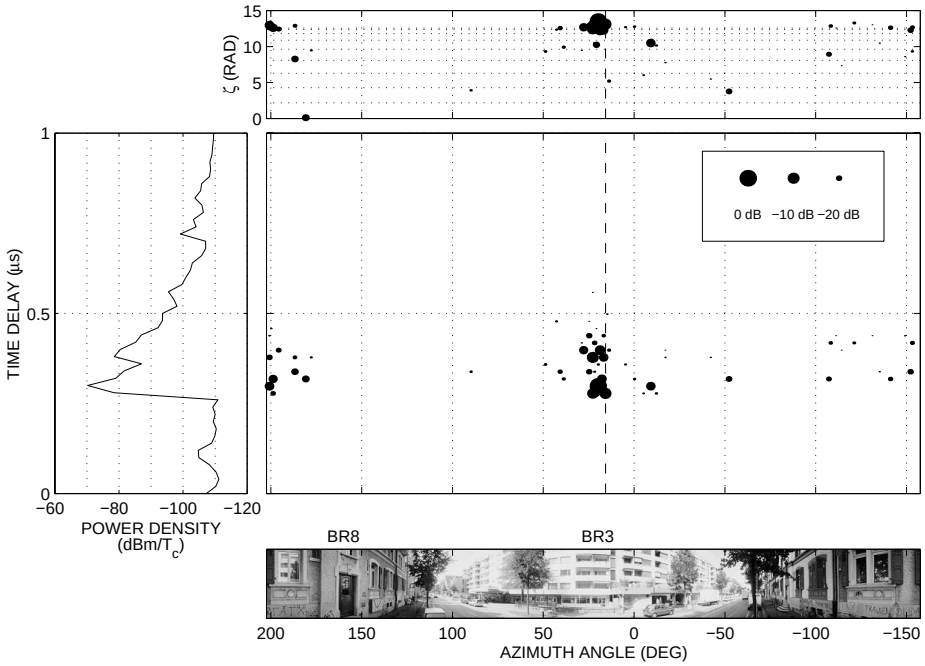

Fig. 3.4: Temporal-angular multipath distribution for MS location 2 in Bern. Marker size indicates multipath wave amplitude relative to total power (down to -30 dB). BS antenna position is indicated by dashed vertical line.

of contributions due to multipath radiowaves propagating through Breitfeld Street, around the corner with Rutli Street and then on to the receiver. The fact that most waves arrive from outside the grey area indicates that they are the result of repeated interactions with the buildings, e.g. of multiple reflection between the buildings on both sides of the streets. These observations are in agreement with the results of the prediction. The AOAs of the very first contributions arriving at the MS are close to the direction of the base station antenna. As their elevation angles are relatively high, these waves are most likely the result of propagation over building BR3. However, their contribution to the total received field is negligible.

According to the propagation model used to produce the prediction of Fig. 3.2, the field received at MS location 2 is composed of multipath waves propagating around both sides of the building block between Breitfeld Street and Rodtmatt Street. Because the reflection and diffraction losses associated with these propagation paths are high, the predicted field strength for this scenario is very low. Fig. 3.4 shows the temporal-angular multipath distribution measured at this MS location. The received

field is dominated by a series of strong contributions arriving from the direction of building BR3. For the corresponding time delays, the average power delay profile shows two high peaks, which can be determined to be 28 and 35 dB below the free-space level. The ζ-values of these contributions show that they cannot be the result of over-rooftop propagation (for which the elevation angle ϑ should be greater than 25^{o}, or $\zeta < 11.4$ radians), but must result from transmission through BR3. The small angular spread of these multipath waves is probably the result of multiple scattering taking place inside the building. The waves arriving from $\varphi \simeq 200^{\,\mathrm{o}}$ are reflected from building BR8, which is on the other side of the MS.

The second peak of the measured power delay profile appears as a second cluster of points in Fig. 3.4. The time delay difference between both clusters suggests that the second contribution is due to reflection from building BB3 (with reflection coefficient -7 dB) and subsequent transmission through BR3.

3.2.2 Controlled environment

Additional AOA measurements behind buildings were later carried out on the TU/e campus, which is a more "controlled" environment than most real urban microcell environments: during weekends, it was possible to perform measurements in the absence of disturbing factors such as traffic, parked cars and people inside and around the buildings. The results shown here were obtained for the configuration of Fig. 3.5, in which the building TR obstructs the line-of-sight path between the base station antenna – a vertically polarised, 12-dBi, omnidirectional antenna with a vertical 3-dB beamwidth of 6^{o}, placed at a height of 6.5 m – and the mobile station. A detailed description of this building is given in Section 4.4.2.

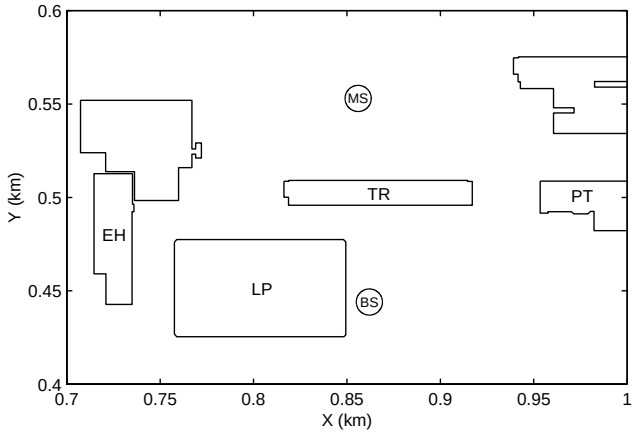

Fig. 3.5: Map of the measurement site on the TU/e campus.

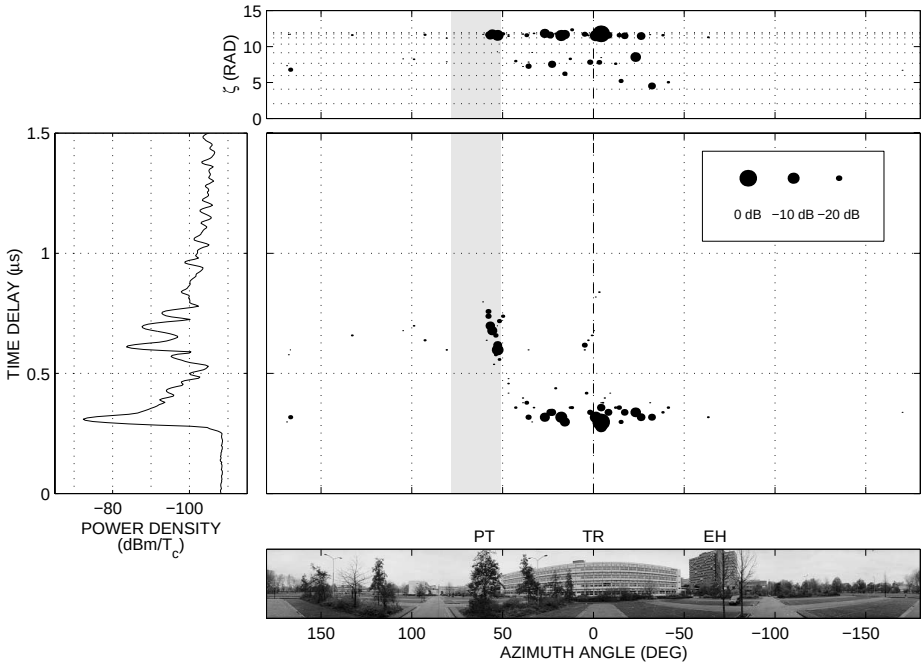

Fig. 3.6: Temporal-angular multipath distribution for building transmission experiment. Marker size indicates multipath wave amplitude relative to total power (down to -30 dB). BS antenna position is indicated by dashed vertical line.

Fig. 3.6 shows the measured temporal and angular multipath distribution. The first and highest peak in the average power delay profile is a result of a number of waves arriving from the direction of building TR. The corresponding elevation angles are smaller than would be the case for propagation over the rooftop of TR [30]; hence, these waves propagate through the building. The received power due to these contributions is 32 dB below the free-space level. The multipath components which arrive 0.3–0.5 μs after the first peak, from the angular region $50^{\circ} < \varphi < 60^{\circ}$, can be identified as reflections from the side face of building PT and from a low transformer kiosk between TR and PT [30], which is not shown in Fig. 3.5.

The azimuth angles of the waves transmitted through building TR are spread out over a large interval ($-40^{\circ} < \varphi < 40^{\circ}$). Evidently, these waves propagate through different parts of the building and therefore have different propagation delays. However, as their delay differences are small in terms of the resolution of the channel sounding system, these waves cannot be resolved in the time domain and appear as a single peak in the power delay profile. In comparison with these results, only a very

small angular spread is observed at MS location 2 in Bern (view Fig. 3.4). This is probably a result of the fact that only a small part of the obstructing building BR3 was directly illuminated by the base station antenna, as can be seen in Fig. 3.1.

3.3 Scattering from trees

Scattering of radiowaves from objects such as trees has been brought up in several studies as a possible explanation for observed discrepancies between field strength predictions and measurements in urban microcell environments – especially for scenarios in which propagation around street corners is important [31, 32]. It has proved to be difficult or even impossible, however, to obtain hard evidence for the significance of this phenomenon from conventional, narrowband field measurements. The measurement technique described in the previous chapter makes it possible to separate scattered waves from other multipath components, and is therefore more suitable for this purpose.

Section 3.3.1 presents AOA measurement results obtained in an urban microcell configuration in Fribourg, Switzerland, which provide evidence for the importance of scattering from vegetation. These measurements were performed at 2000 MHz, using the Ericsson channel sounding equipment (view Table 2.1). In Section 3.3.2, results are shown of a measurement on a single tree, conducted using the TU/e equipment, at a carrier frequency of 1900 MHz.

3.3.1 Realistic urban microcell environment – Fribourg

A plan of the area in Fribourg selected for the AOA experiments is shown in Fig. 3.7. This environment is characterised by four- to six-storey concrete buildings with irregular faces (balconies and windows), trees lining both sides of the main street (Perolles), and moderate to high traffic density. Cars are parked along the curbs. A small park with trees is located opposite to one of the side streets (Jacques-Gachoud). The location of this park is sketched in the plan. In the recent past, Swisscom performed extensive measurements in the area of Fig. 3.7 [29, 31]. One of the results of these measurements was that the received field strength could not be predicted satisfactorily using a model based on reflection and diffraction. This was conjectured to be a result of inadequate modelling of the mechanisms responsible for propagation around the street corners, particularly the neglect of tree scattering effects. The AOA experiments discussed in the following were performed to verify this hypothesis.

A vertically polarised, 3-dBi, omnidirectional base station antenna was placed at the location indicated by “BS” in Fig. 3.7. The base station antenna height was 5 m. Results obtained at two MS locations in Perolles Street, which are indicated in the same figure, are shown in Figs. 3.8 and 3.10. As before, the grey zones in these

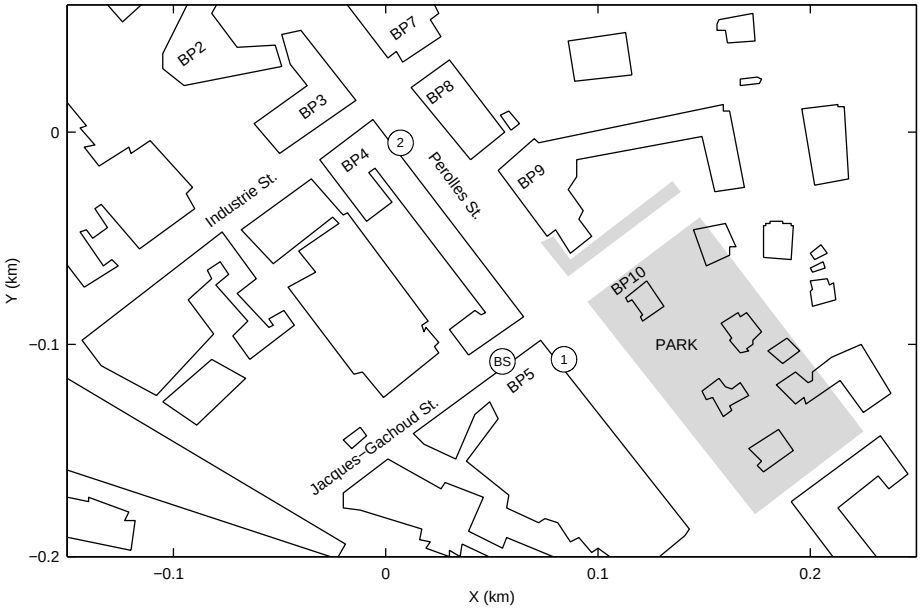

Fig. 3.7: Map of the measurement site in Fribourg.

figures indicate the angular regions in which points at the ground level can be "seen" directly by both the base station and the MS antenna.

The first contributions received at MS location 1 arrive from the direction of the street in which the base station is located (Jacques-Gachoud). These waves are the result of (multiple) reflection between the buildings BP4 and BP5, possibly followed by diffraction from BP4 or BP5. The strongest contributions, however, arrive from the angular region $-30^{\mathrm{o}} < \varphi < 10^{\mathrm{o}}$, corresponding with the park opposite to Jacques-Gachoud Street. The objects in this region, which was directly illuminated by the base station, are mostly trees (view Fig. 3.9). The waves from this region are therefore, most likely, the result of scattering from trees. The total bistatic scattering cross section of these scatterers can be estimated using the bistatic radar equation, and the resulting value of 60 m^2 is in good agreement with the theoretical value for a number of large trees (view Section 5.5.3). The waves arriving from directions in the interval $75^{\mathrm{o}} < \varphi < 120^{\mathrm{o}}$ are the result of scattering from the trees in the park, and subsequent reflection from building BP5.

Theoretically, the field received at MS location 2 is dominated by third- and higher-order reflected rays arriving from the direction of building BP9 [33]. Contributions reflected from this building are indeed visible in the measurement results

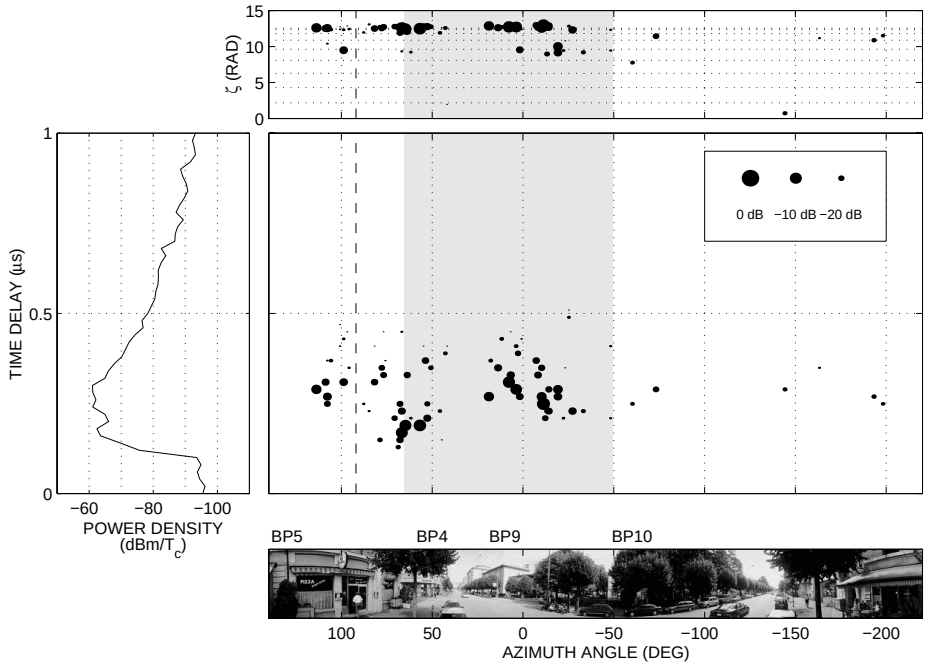

Fig. 3.8: Temporal-angular multipath distribution for MS location 1 in Fribourg. Marker size indicates multipath wave amplitude relative to total power (down to -30 dB). BS antenna position is indicated by dashed vertical line.

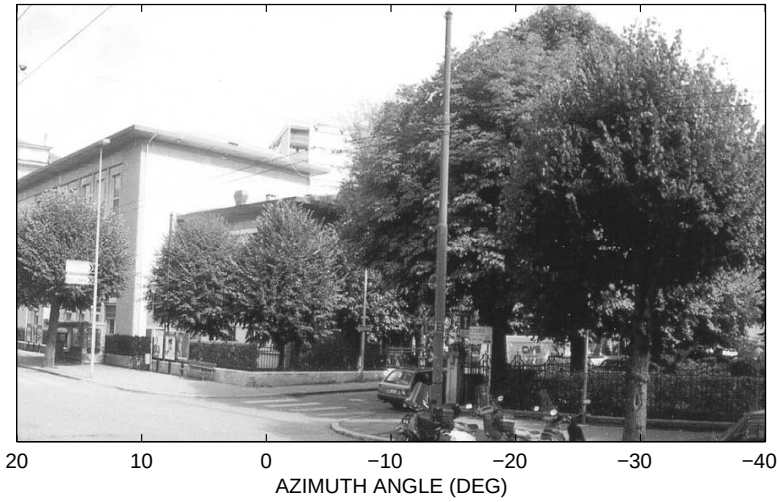

Fig. 3.9: Enlarged section of the panorama photograph taken at MS location 1 in Fribourg.

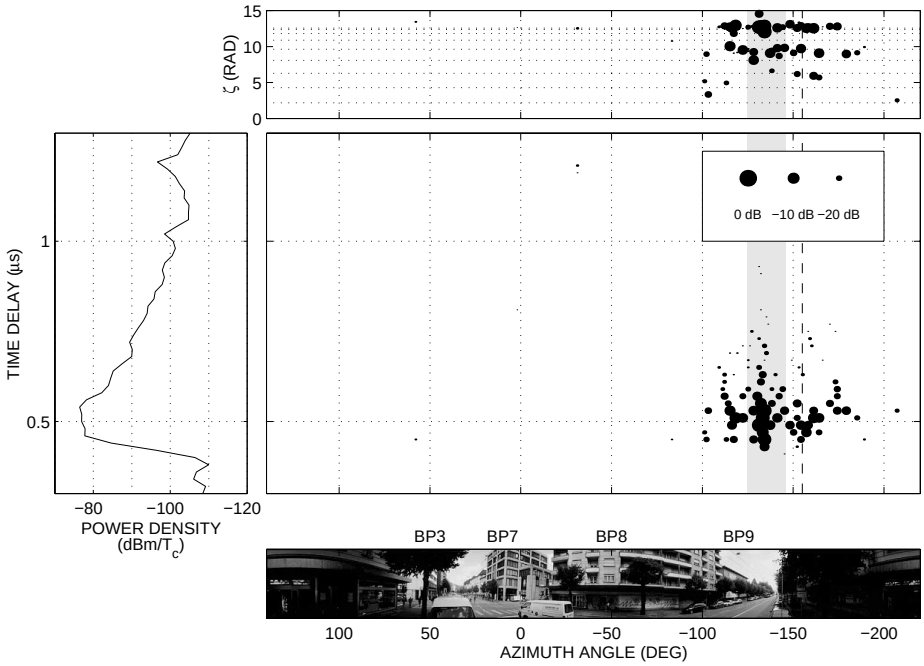

Fig. 3.10: Temporal-angular multipath distribution for MS location 2 in Fribourg. Marker size indicates multipath wave amplitude relative to total power (down to -30 dB). BS antenna position is indicated by dashed vertical line.

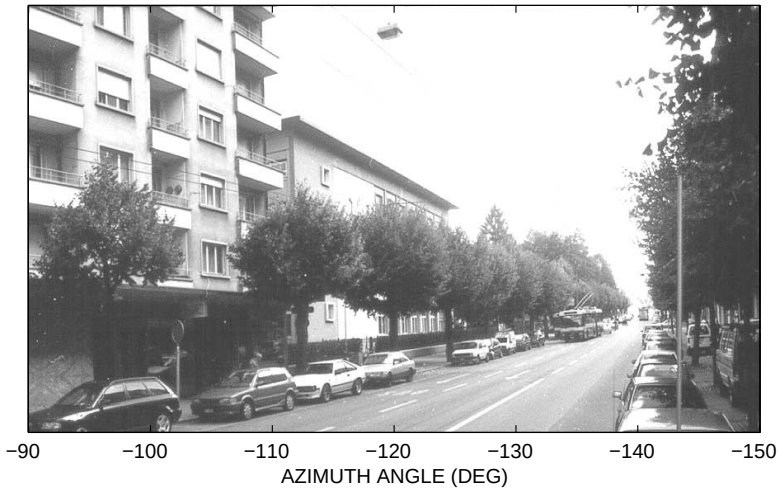

Fig. 3.11: Enlarged section of the panorama photograph taken at MS location 2 in Fribourg.

of Fig. 3.10, but they are less prominent than the series of waves arriving from $\varphi \simeq -130^{o}$, which corresponds to the direction of the park opposite to Jacques-Gachoud Street. The front side of this park was directly illuminated by the base station antenna. A better view of this angular region is given in Fig. 3.11 (the trolley bus seen in this figure was not present during the measurement). The multipath components arriving from this direction have a considerable delay spread, which is a strong indication that they are the result of scattering from a number of spatially dispersed scatterers, such as the trees in the park. Based on the received power in the time delay interval around $\tau \simeq 0.5$ μs, the total bistatic scattering cross section of these scatterers can be estimated as approximately 30 m^2. Again, this value is similar to the theoretical scattering cross section of a group of large trees (view Section 5.5.3).

3.3.2 Controlled environment

In order to verify the hypothesis that scattering from trees is a significant propagation phenomenon which may account for some of the discrepancies between propagation predictions and measurements, additional AOA experiments were performed on a single deciduous tree in a "controlled" environment. This environment is formed by a large farmer's field in Boxtel, The Netherlands, on which no objects other than the tree are present. A plan of this configuration is sketched in Fig. 3.12. A photograph of the tree, which was in full leaf during the measurements, is shown in Fig. 5.6 on page 97 of this thesis. The base station antenna, a 7.1-dBi vertically polarised

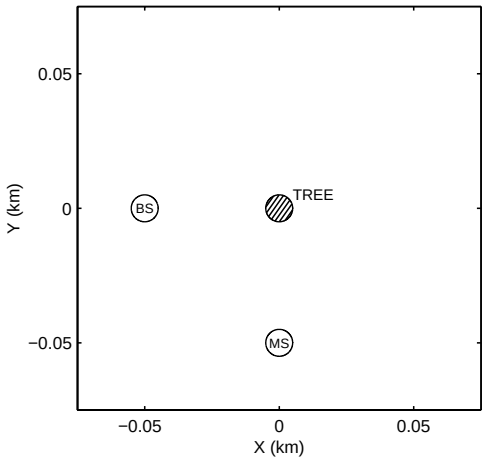

Fig. 3.12: Map of the measurement site in Boxtel.

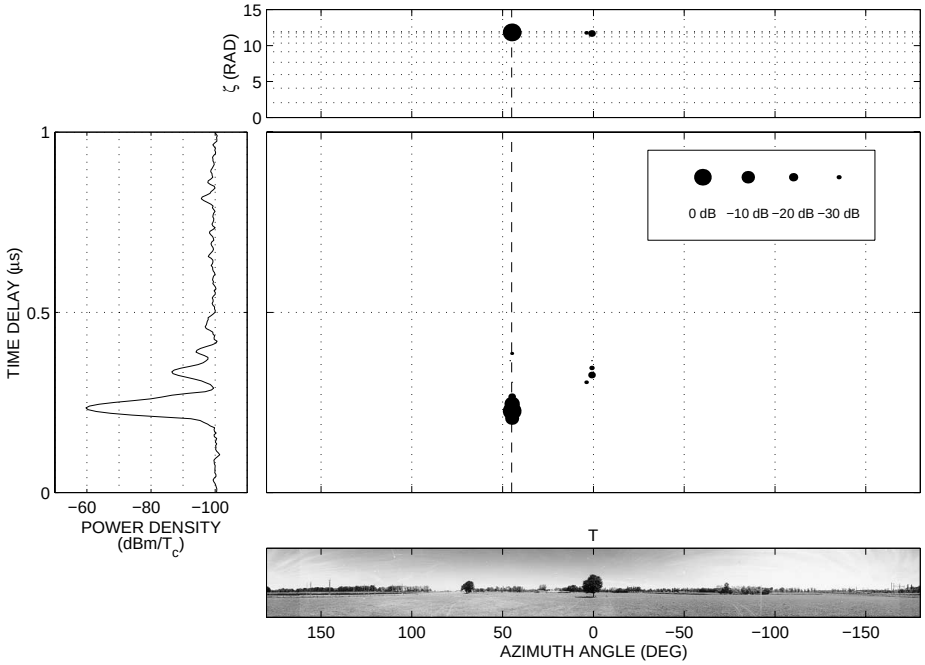

Fig. 3.13: Temporal-angular multipath distribution for tree scattering experiment. Marker size indicates multipath wave amplitude relative to total power (down to -40 dB). BS antenna position is indicated by dashed vertical line.

double-ridged pyramidal horn with an azimuthal 3-dB beamwidth of 53°, was located at a height of 7 m, and directed towards the centre of the tree canopy. The directivity of this antenna in the direction of the MS location was 8 dB below the maximum directivity.

Fig. 3.13 shows the measured temporal-angular distribution of the received multipath components. The two highest peaks in the power delay profile are due to the direct wave from the transmitter and the scattering contribution from the tree. The height of the peak due to the scattered wave corresponds with a bistatic scattering cross section of approximately 5 m^2, which is in excellent agreement with the results of Section 5.5.3. The third contribution, which arrives from the same direction as the direct wave, must be the result of reflection at the ends of the cable connecting the transmitter unit with the antenna. This cable has a mechanical length of 15 m and a nominal velocity factor of 66%, which matches the measured delay of 0.16 μs with respect to the first peak.

3.4 Conclusions

In this chapter, results of wideband AOA measurements obtained under microcellular conditions, i.e. with low simulated base station antennas, were presented. Transmission through buildings, which is not taken into account by most existing propagation prediction models, was demonstrated to be the dominant propagation mechanism in two different configurations. In fact, as will be shown in Chapter 4, this phenomenon plays a significant role in most of the many building transmission experiments that were carried out in a later stage of the present study. In the two examples discussed in this chapter, the path losses of the transmitted contributions, relative to the free-space loss, are approximately 30 dB. Such a low shielding effectiveness of buildings, if disregarded in the planning stage of urban microcellular networks, may lead to unacceptable levels of co-channel interference.

Results obtained in two other configurations show that scattering from trees can be significant in situations where the line-of-sight propagation path is obstructed and reflection and diffraction contributions are weak, for example in streets perpendicular to the street in which the base station is located. This may well explain why models based on reflection and diffraction alone have proved to be unsatisfactory, under circumstances reported in [31, 32], in modelling propagation around street corners. A theoretical model for the scattering from trees is presented in Chapter 5.

4

Propagation into and through buildings

4.1 Introduction

Propagation research for mobile communications in urban microcells has hitherto been focused mainly on the modelling of reflection and diffraction of radiowaves from buildings. These buildings are usually treated as being opaque for radiowaves at the UHF frequencies used for mobile communications. Yet, it was shown in Chapter 3 that transmission through buildings can be the dominant propagation mode in at least parts of the coverage area. In the framework of the European COST 231 project and in some other studies, effort has been put into the modelling of building penetration [4, 34, 35] and transmission [36, 37]. The results of this work are relevant to the present study, but have not led to transmission models that can be directly incorporated in ray-tracing-based propagation prediction tools.

The rigorous computation of the fields due to building penetration and transmission, using e.g. the method of moments [38], finite-difference time domain (FDTD) methods [39, 40], or indoor ray-tracing [41, 42], presumes the availability of detailed knowledge of the buildings' geometrical and dielectric properties, both external and internal. In the practice of cellular network planning such detailed databases are not available and simpler models – using only a few parameters for each building describing its penetration and transmission characteristics – are more desirable.

The primary objective of this chapter is to present a ray-optical model for the

transmission of radiowaves through buildings for which only the exterior coordinates and very limited additional information are available. The unknown interior of each building is characterised by an effective attenuation constant α_b. The new transmission model can be used in conjunction with "conventional" models for ray-optical reflection and (external) diffraction based on the uniform theory of diffraction (UTD), but it introduces two additional types of radiowave interaction with the buildings. According to the new model, rays incident on one of the planar faces that together make up the building surface (or exterior wall) can penetrate into the building. These rays are called geometric-optical (GO) transmitted rays. Also, rays incident on one of the vertical building edges joining two planar faces give rise to *internally* diffracted rays, i.e. diffracted rays that propagate into the building interior. Rays that have propagated into the building in either of these ways can then again propagate into the free space surrounding the building via GO transmission or internal diffraction. The field outside a building due to such so-called *transmitted rays* is referred to as the (total) transmitted field due to that building.

To date, no high-frequency asymptotic solution exists for the canonical problem of scattering from a dielectric wedge, from which the exact external and internal UTD diffraction coefficients required for a rigorous ray-optical transmission model could be derived. The diffraction coefficients used in this chapter provide an approximate solution to this canonical problem. Contrary to the well-known diffraction coefficients proposed by Luebbers [43] and Tiberio-Maliuzhinets [44], which are also approximations but very commonly used to model external diffraction from dielectric wedges, they can also be used to compute internal diffraction fields. The new diffraction coefficients are derived from integral representations of the fields just inside and outside the exterior wall of the building. In accordance with the laws of physical optics (PO), these surface fields are approximated by GO fields. The theory in this chapter closely follows the work by Taket, Burge and co-workers on diffraction by conducting and lossless dielectric wedges [45, 46]. However, the new transmission model forms an extension to this work in the sense that it also takes into account the losses in the interiors of the scattering objects (the buildings).

The organisation of this chapter is as follows. The new building transmission model is presented in Section 4.2. Section 4.3 provides some numerical results that were generated by this model. It is shown, among other things, that the field in the deep shadow behind a rectangular building is determined entirely by GO transmission. This observation forms the basis of the experiments discussed in Section 4.4. In that section, empirical values of α_b are obtained for a set of 22 buildings, by fitting the expression for the GO transmitted field to the results of field measurements taken in the buildings' deep shadow regions. Section 4.5 concludes the chapter.

4.2 Building transmission model

For the purpose of the present study, buildings are modelled as infinitely high objects with planar faces. These faces (including windows, doors, etc.) are modelled as thin slabs with uniform (effective) complex permittivity ϵ_r. Further, only the exterior building coordinates are assumed to be known. An illustration of this building model is given in Fig. 4.1. In this figure, region 1 denotes the interior building volume; region 2 is the free space surrounding the building. These regions are separated by the closed surface S, which represents the building's exterior wall. For convenience, S will also be used in the following to denote a single planar face of the building. The vector $\hat{\mathbf{n}}$ is the unit normal vector of S which points into region 2.

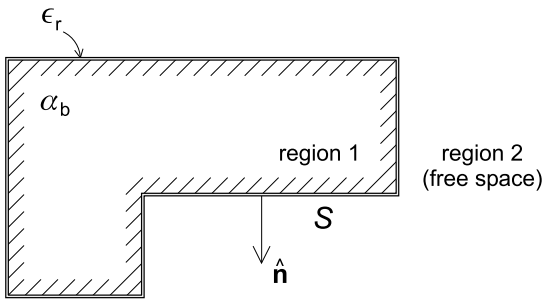

Fig. 4.1: Illustration of the building model (top view).

As with ray-tracing models that do not incorporate transmission through buildings, the interaction of radiowaves with the building's exterior wall is assumed to be independent of the building interior, and to be completely determined by ϵ_r. This assumption enables one to extend existing propagation prediction tools with the present transmission model in a straightforward manner.

Obviously, as in outdoor environments, radio propagation inside buildings is governed by mechanisms such as reflection, diffraction and scattering from various objects. The distribution of the field strength inside a building is therefore dependent on specific features of its internal structure (e.g. layout, construction materials). As no knowledge is available about these features, it is impossible to predict the exact internal field distribution. Instead, in an attempt to capture the global behaviour of the penetrated and transmitted fields, the building interior is treated as a homogeneous medium in which the excess propagation loss – the path loss relative to the free-space loss – can be described by a specific attenuation factor α_b, expressed in decibels per metre, and the propagation velocity is equal to that in free space. Hence, the behaviour of the field inside the building (region 1) is described by the Green's

function

$$G_1(\mathbf{r}, \mathbf{r}') = \frac{e^{-jk_1|\mathbf{r}-\mathbf{r}'|}}{4\pi|\mathbf{r}-\mathbf{r}'|}, \tag{4.1}$$

with $k_1 = k - j\alpha_b/8.686$, k being the free-space wavenumber. In general, rays incident on an interface between free space and a lossy medium are refracted, i.e. the transmission angle is not equal to the incidence angle, even if the phase constant in the lossy medium is equal to k [47]. However, as $|\mathrm{Im}\, k_1| = \alpha_b/8.686 \ll k$ for the relatively small values of α_b found in practice (view Section 4.4), refraction of rays at the exterior wall can be neglected.

4.2.1 Surface fields

The field incident on the building from region 2 is assumed to be a ray-optical field and can therefore be written as

$$E_2^i(\mathbf{r}) = A_i(\mathbf{r}) \exp\{-jkS_i(\mathbf{r})\}, \tag{4.2}$$

where k is the free-space wavenumber. The eikonal of the incident field may be expanded up to second order about any point $\mathbf{r}_0$ on the building surface, as

$$S_i(\mathbf{r}) = S_i(\mathbf{r}_0) + \hat{\mathbf{k}}_i \cdot (\mathbf{r}-\mathbf{r}_0) + \frac{1}{2}(\mathbf{r}-\mathbf{r}_0) \cdot \left[\frac{\hat{\mathbf{x}}_1\hat{\mathbf{x}}_1}{r_1} + \frac{\hat{\mathbf{x}}_2\hat{\mathbf{x}}_2}{r_2} \right] \cdot (\mathbf{r}-\mathbf{r}_0), \tag{4.3}$$

where $\hat{\mathbf{k}}_i$ is the incident wave direction at $\mathbf{r}_0$. Furthermore, r_1 and r_2 are the principal radii of curvature of the incident wavefront, and $\hat{\mathbf{x}}_1$ and $\hat{\mathbf{x}}_2$ are unit vectors, each of which in combination with $\hat{\mathbf{k}}_i$ defines one of the principal planes of curvature. It is assumed that $\hat{\mathbf{x}}_1$ is oriented vertically, parallel to the building surface, and $\hat{\mathbf{x}}_2$ is oriented horizontally. The amplitude factor $A_i(\mathbf{r})$ varies only slowly, and can be considered constant in the neighbourhood of $\mathbf{r}_0$, i.e. $A_i(\mathbf{r}) = A_i(\mathbf{r}_0)$ if $\mathbf{r}$ is near $\mathbf{r}_0$.

According to the PO approximation, the field on the exterior surface of the building is assumed to be zero at all surface points that are not directly illuminated by the incident field. Of the field incident on any directly illuminated surface point, a fraction is reflected back into region 2, and part is transmitted into the building interior. The GO reflected field can be written as

$$E_2^r(\mathbf{r}) = A_i(\mathbf{r}_0) R(\mathbf{r}_0) \exp\{-jkS_i(\mathbf{r} - 2\hat{\mathbf{n}}\hat{\mathbf{n}} \cdot (\mathbf{r}-\mathbf{r}_0))\}, \quad \mathbf{r} \text{ near } \mathbf{r}_0, \tag{4.4}$$

where $R(\mathbf{r}_0)$ is the reflection coefficient of the wall, which, in general, depends on the dielectric properties of the external-side building materials and the angle of the

incident wave with respect to the building surface at $\mathbf{r}_0$. The total GO exterior field near $\mathbf{r}_0$ is

$$E_2^{\mathrm{GO}}(\mathbf{r}) = E_2^i(\mathbf{r}) + E_2^r(\mathbf{r}), \quad \mathbf{r} \text{ near } \mathbf{r}_0. \tag{4.5}$$

Likewise, the GO transmitted field in region 1 can be written as

$$E_1^t(\mathbf{r}) = A_i(\mathbf{r}_0)T(\mathbf{r}_0)\exp\{-jkS_i(\mathbf{r}_0) - jk_1[S_i(\mathbf{r}) - S_i(\mathbf{r}_0)]\}, \quad \mathbf{r} \text{ near } \mathbf{r}_0, \tag{4.6}$$

where $T(\mathbf{r}_0)$ is the transmission coefficient of the wall at $\mathbf{r}_0$. The GO interior field near $\mathbf{r}_0$, just inside the exterior wall, is completely due to the transmitted field and therefore

$$E_1^{\mathrm{GO}}(\mathbf{r}) = E_1^t(\mathbf{r}), \quad \mathbf{r} \text{ near } \mathbf{r}_0. \tag{4.7}$$

In principle, the reflection and transmission coefficients of the exterior wall in equations (4.4) and (4.6) can be chosen freely. In cases in which the geometrical and dielectric properties of the exterior wall are precisely known it may be possible to find the exact coefficients, otherwise approximate reflection and transmission coefficients must be used. In the present case, use is made of the soft Fresnel reflection coefficient (view Fig. 4.2 for the definition of the incidence angle θ_i)

$$R(\mathbf{r}) = \frac{\cos\theta_i - \sqrt{\epsilon_r - \sin^2\theta_i}}{\cos\theta_i + \sqrt{\epsilon_r - \sin^2\theta_i}}. \tag{4.8}$$

This reflection coefficient, in combination with values of the complex permittivity ϵ_r within a range that applies to most common building materials, is well known to provide an accurate approximation of the fields reflected from building faces (for vertical polarisation), and is used in most deterministic propagation prediction models. A permittivity equal to 5 was shown to be an optimum choice in two independent studies [48, 49] and will be used in the following.

Application of the Fresnel reflection coefficient implies that a fraction of the incident field equal to the soft Fresnel transmission coefficient

$$T_2 = \frac{2\cos\theta_i}{\cos\theta_i + \sqrt{\epsilon_r - \sin^2\theta_i}} \tag{4.9}$$

is transmitted across the outer boundary of the wall. Of this field, in turn, a fraction is transmitted into the building interior (region 1). Because $|\mathrm{Im}\, k_1| = \alpha_b/8.686 \ll k$, the corresponding transmission coefficient can be written as

$$T_1 = \frac{2\cos\theta_t}{\cos\theta_t + \sqrt{1/\epsilon_r - \sin^2\theta_t}} \tag{4.10}$$

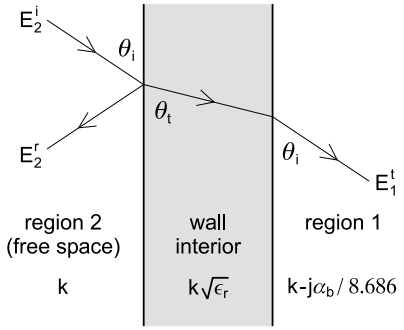

Fig. 4.2: Reflection from and transmission through a dielectric wall.

and the propagation direction of the field transmitted through the wall is equal to that of the incident field (view Fig. 4.2). The effects of reflection and scattering inside the wall, the calculation of which would require precise knowledge of the wall's (local) thickness and internal structure, are neglected. Also, for simplicity, the losses inside the wall are not included in the transmission coefficient. Together with the losses inside the building interior, they are accounted for by the attenuation coefficient α_b. With the above approximations, the transmission coefficient of the wall becomes [50]

$$T(\mathbf{r}) = T_1 T_2 = 1 - R^2(\mathbf{r}). \tag{4.11}$$

4.2.2 Interior fields

For any scattering object the internal field may be expressed as the integral of the total interior surface field (and a Green's function) over the entire surface [51]. In the PO approximation, the true interior field is replaced by the GO surface field $E_1^{\mathrm{GO}}(\mathbf{r})$. To further simplify matters, the interior field due to a single planar face S of the building will be considered. This can be written as

$$E_1(\mathbf{r}) = \iint_S \left[G_1(\mathbf{r}, \mathbf{r}') \frac{\partial E_1^{\mathrm{GO}}(\mathbf{r}')}{\partial \hat{\mathbf{n}}} - E_1^{\mathrm{GO}}(\mathbf{r}') \frac{\partial G_1(\mathbf{r}, \mathbf{r}')}{\partial \hat{\mathbf{n}}} \right] dS', \tag{4.12}$$

in which the gradients are taken with respect to $\hat{\mathbf{n}}$, the unit normal vector of S (view Fig. 4.1). Under the assumption that S is large in terms of the wavelength, the phase of the integrand in (4.12) varies rapidly over S. According to the method of stationary phase, the integral can therefore be well approximated by the contributions from the neighbourhoods of critical (stationary) points on S [45, 46]. In the present case there are two sorts of critical points. The first type is formed by the point in

the interior of S where the phase is stationary, if it exists. The second type are those points on the vertical edges of S where the phase of the integrand is stationary with respect to movement along the edge. There can be maximally two critical points of the second type per building face, depending on whether the edges are directly illuminated by the incident field. These points correspond with the edge-diffraction points in the UTD.

The interior field is evaluated at a point with position vector $\mathbf{r}$. It is convenient to express this point in terms of its displacement from an (arbitrary) critical point $\mathbf{r}_0$ on S. For surface points $\mathbf{r}'$ in the neighbourhood of $\mathbf{r}_0$, the Green's function can be approximated by

$$\begin{aligned} G_1(\mathbf{r}_0+s\hat{\mathbf{k}}_s, \mathbf{r}') = & \frac{\exp\{-jk_1[s-\hat{\mathbf{k}}_s\cdot(\mathbf{r}'-\mathbf{r}_0)]\}}{4\pi s} \\ & \times \exp\left\{-jk_1\left[\frac{(\mathbf{r}'-\mathbf{r}_0)\cdot(\overline{\mathbf{I}}-\hat{\mathbf{k}}_s\hat{\mathbf{k}}_s)\cdot(\mathbf{r}'-\mathbf{r}_0)}{2s}\right]\right\}, \end{aligned} \tag{4.13}$$

where $s = |\mathbf{r}-\mathbf{r}_0|$ is the distance from $\mathbf{r}_0$ to the observation point, the unit vector $\hat{\mathbf{k}}_s = (\mathbf{r}-\mathbf{r}_0)/s$ denotes the scattering direction, and $\overline{\mathbf{I}}$ is the unit dyadic. With this approximation, the interior field due to the isolated critical point at $\mathbf{r}_0$ can be written as (cf. [45, 46])

$$\begin{aligned} E_1^c(\mathbf{r}_0+s\hat{\mathbf{k}}_s) = & -\frac{jk_1e^{-jk_1s}}{4\pi s}E_2^i(\mathbf{r}_0)T(\mathbf{r}_0)\,\hat{\mathbf{n}}\cdot(\hat{\mathbf{k}}_i+\hat{\mathbf{k}}_s) \\ & \times \iint_{S_c} \exp\{-jk_1[\mathbf{b}\cdot(\mathbf{r}'-\mathbf{r}_0)+\frac{1}{2}(\mathbf{r}'-\mathbf{r}_0)\cdot\overline{\mathbf{C}}\cdot(\mathbf{r}'-\mathbf{r}_0)]\}dS', \end{aligned} \tag{4.14}$$

where

$$\begin{aligned} \mathbf{b} &= \hat{\mathbf{k}}_i - \hat{\mathbf{k}}_s \\ \overline{\mathbf{C}} &= \frac{\overline{\mathbf{I}}-\hat{\mathbf{k}}_s\hat{\mathbf{k}}_s}{s} + \frac{\hat{\mathbf{x}}_1\hat{\mathbf{x}}_1}{r_1} + \frac{\hat{\mathbf{x}}_2\hat{\mathbf{x}}_2}{r_2}, \end{aligned} \tag{4.15}$$

and the integration domain S_c is a subdomain of S which contains only the critical point at $\mathbf{r}_0$. The total interior field at $\mathbf{r} = \mathbf{r}_0 + s\hat{\mathbf{k}}_s$ is calculated as the sum of the contributions from all critical points.

If the face S contains a critical point of the first type, which is the case if there is a (directly illuminated) point $\mathbf{r}_0$ within S for which $\hat{\mathbf{k}}_s = \hat{\mathbf{k}}_i$, its contribution to the total interior field is found by replacing the integration domain S_c in (4.14) by the whole infinite plane S_∞ of which S is a subdomain [45]. The stationary-phase

approximation of the resulting double integral is given by

$$E_1^t(\mathbf{r}_0 + s\hat{\mathbf{k}}_s) = E_2^i(\mathbf{r}_0)T(\mathbf{r}_0)\sqrt{\frac{r_1 r_2}{(r_1+s)(r_2+s)}}\, e^{-jk_1 s}. \tag{4.16}$$

This field contribution is recognised as the field associated with a GO "transmitted ray" propagating along the direct path from the source of the incident field, through a transmission point at $\mathbf{r}_0$, to $\mathbf{r}$. In the special case that the critical point of the first kind (i.e., the GO transmission point) lies on an edge of S, the transmitted field in (4.16) must be multiplied by a factor 1/2.

The diffraction contributions from the critical points of the second type must be treated separately. For each of these points, a set of coordinates (t', z') in the plane of S is defined by (view Fig. 4.3)

$$\mathbf{r}' = \mathbf{r}_0 + t'\hat{\mathbf{t}} + z'\hat{\mathbf{z}}, \tag{4.17}$$

where $\hat{\mathbf{t}}$ is a unit vector in the plane of S which points to the side of the edge on which the surface lies, and $\hat{\mathbf{z}}$ is a vertical unit vector pointing upwards. The contribution from each diffraction point can be found by taking the integration domain S_c in (4.14) to be [45]

$$S_c = \begin{cases} S, & \text{if } \hat{\mathbf{t}}\cdot\mathbf{b} > 0 \\ S - S_\infty, & \text{if } \hat{\mathbf{t}}\cdot\mathbf{b} < 0. \end{cases} \tag{4.18}$$

Then, after performing the integrations over t' (from 0 to $\pm\infty$, depending on the sign of $\hat{\mathbf{t}}\cdot\mathbf{b}$) and z' (from $-\infty$ to ∞), it follows that [46]

$$E_1^d(\mathbf{r}_0 + s\hat{\mathbf{k}}_s) = E_2^i(\mathbf{r}_0)\; D_{\text{int}}^{2\to 1}\sqrt{\frac{r_1}{s(r_1+s)}}\, e^{-jk_1 s}, \tag{4.19}$$

where

$$D_{\text{int}}^{2\to 1} = -\frac{1}{2}\text{sgn}\big[\hat{\mathbf{t}}\cdot\mathbf{b}\big]\; T(\mathbf{r}_0)\; \hat{\mathbf{n}}\cdot(\hat{\mathbf{k}}_s + \hat{\mathbf{k}}_i)\; \sqrt{C}\; K_-\left(\sqrt{\frac{k_1 C\big[\hat{\mathbf{t}}\cdot\mathbf{b}\big]^2}{2}}\right) \tag{4.20}$$

is the internal diffraction coefficient for diffraction from region 2 into region 1. Here, the vector $\hat{\mathbf{k}}_s$ points into the building interior. Furthermore, the function sgn$(\cdot)$ is defined as

$$\text{sgn}(x) = \begin{cases} 1, & \text{if } x > 0, \\ 0, & \text{if } x = 0, \\ -1, & \text{if } x < 0, \end{cases} \tag{4.21}$$

the parameter C is written as

$$C = \frac{1}{\hat{\mathbf{t}} \cdot \overline{\mathbf{C}} \cdot \hat{\mathbf{t}}} \tag{4.22}$$

and the function

$$K_{-}(\tau) = \frac{1}{\sqrt{\pi}} e^{j(\tau^2+\pi/4)} \int_{\tau}^{\infty} e^{-jt^2} dt \tag{4.23}$$

is the modified Fresnel integral. An accurate algorithm for computing $K_{-}(\cdot)$, which can be used for complex argument values, is presented in [52]. This algorithm involves the evaluation of a polynomial function, the coefficients of which have to be computed only once by a fast Fourier transformation. The vector inner products and the parameter C in (4.20) can be expressed in terms of the incident and scattering angles φ' and φ, which are defined from the exterior side of S (view Fig. 4.3), as follows:

$$\begin{aligned} \hat{\mathbf{t}} \cdot \mathbf{b} &= -\cos\varphi' - \cos\varphi \\ \hat{\mathbf{n}} \cdot \hat{\mathbf{k}}_i &= -\sin\varphi' \\ \hat{\mathbf{n}} \cdot \hat{\mathbf{k}}_s &= \sin\varphi \\ C &= \left[\frac{\sin^2\varphi'}{r_2} + \frac{\sin^2\varphi}{s} \right]^{-1}. \end{aligned} \tag{4.24}$$

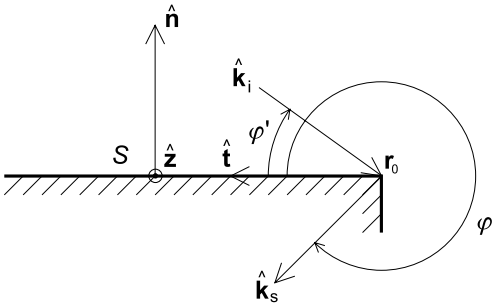

Fig. 4.3: Definition of coordinate vectors and incident and scattering angles relative to the planar face S (top view).

To calculate the interior field due to diffraction from the wedge formed by a building corner, the two planar faces that compose the corner must be treated separately, i.e., a diffraction coefficient is evaluated for each face that is illuminated by the incident field.

4.2.3 Transmitted fields

The GO transmitted and internally diffracted fields inside the building, which are due to the field (4.2) incident on the building from the outside, will in turn be incident on the building surface from the interior and give rise to secondary fields outside the building (as well as secondary fields inside the building, but these will be neglected). These secondary exterior fields are referred to as transmitted fields, and the rays describing these fields are called transmitted rays (view Fig. 4.4). The scattered fields external to the building caused by reflection and diffraction from its outer faces and corners will be considered in Section 4.2.4.

Consider the interior field

$$E_1^i(\mathbf{r}) = A_i(\mathbf{r}) \exp\{-jk_1 S_i(\mathbf{r})\} \tag{4.25}$$

incident on the single planar building face S and, for the moment, assume that no other fields are present. As in Section 4.2.1, the eikonal $S_i(\mathbf{r})$ is expanded about an arbitrary critical point $\mathbf{r}_0$ on the building surface, which leads to expression (4.3). At each surface point, the field just inside the exterior wall is assumed to be zero if the point is not directly illuminated by the incident field. Of the field incident on any

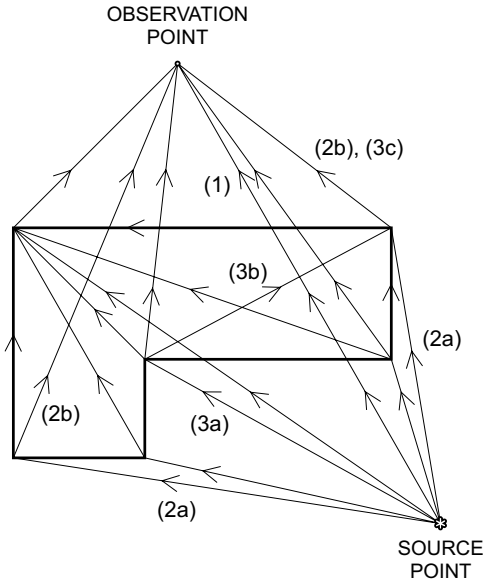

Fig. 4.4: Illustration of transmitted rays (top view).

directly illuminated surface point, a part is transmitted into region 2 and forms the GO exterior field. For observation points $\mathbf{r}$ close to $\mathbf{r}_0$, this field can be written as

$$E_2^{\mathrm{GO}}(\mathbf{r}) = E_2^t(\mathbf{r}) = A_i(\mathbf{r}_0)T(\mathbf{r}_0) \times \exp\{-jk_1 S_i(\mathbf{r}_0) - jk[S_i(\mathbf{r}) - S_i(\mathbf{r}_0)]\}, \quad \mathbf{r} \text{ near } \mathbf{r}_0. \quad (4.26)$$

The field that is reflected back into the building interior is neglected.

The total transmitted field due to S at any observation point in region 2 can be written as an integral of the exterior surface field due to $E_1^i(\mathbf{r})$ (and a Green's function) over S [51]. As before, this surface field is replaced by the GO surface field due to $E_1^i(\mathbf{r})$, which yields

$$E_2(\mathbf{r}) = -\iint_S \left[G_2(\mathbf{r}, \mathbf{r}') \frac{\partial E_2^{\mathrm{GO}}(\mathbf{r}')}{\partial \hat{\mathbf{n}}} - E_2^{\mathrm{GO}}(\mathbf{r}') \frac{\partial G_2(\mathbf{r}, \mathbf{r}')}{\partial \hat{\mathbf{n}}} \right] dS', \quad (4.27)$$

where $G_2(\mathbf{r}, \mathbf{r}')$ is the free-space Green's function. As before, the unit normal vector $\hat{\mathbf{n}}$ points into region 2 (view Fig. 4.1). As S is large in terms of the wavelength, the transmitted field $E_2(\mathbf{r})$ is principally due to a GO contribution (if S contains a critical point of the first type) and maximally two diffraction contributions from the edges of S. The GO transmitted field is

$$E_2^t(\mathbf{r}_0 + s\hat{\mathbf{k}}_s) = E_1^i(\mathbf{r}_0)T(\mathbf{r}_0)\sqrt{\frac{r_1 r_2}{(r_1 + s)(r_2 + s)}}\, e^{-jks}, \quad (4.28)$$

and the edge-diffracted fields can each be written as

$$E_2^d(\mathbf{r}_0 + s\hat{\mathbf{k}}_s) = E_1^i(\mathbf{r}_0)D_{\mathrm{int}}^{1\to 2}\sqrt{\frac{r_1}{s(r_1 + s)}}\, e^{-jks}, \quad (4.29)$$

where

$$D_{\mathrm{int}}^{1\to 2} = \frac{1}{2}\mathrm{sgn}\left[\hat{\mathbf{t}} \cdot \mathbf{b}\right] T(\mathbf{r}_0)\, \hat{\mathbf{n}} \cdot (\hat{\mathbf{k}}_s + \hat{\mathbf{k}}_i)\, \sqrt{C}\, K_-\left(\sqrt{\frac{kC\left[\hat{\mathbf{t}} \cdot \mathbf{b}\right]^2}{2}}\right) \quad (4.30)$$

is the internal diffraction coefficient for diffraction from region 1 into region 2. In this case, the scattering direction vector $\hat{\mathbf{k}}_s$ points into the exterior region of the building (region 2). As before, s is the distance between the critical point $\mathbf{r}_0$ and the observation point $\mathbf{r} = \mathbf{r}_0 + s\hat{\mathbf{k}}_s$, and the vector inner products and the parameter C used in (4.30) can be expressed in terms of the incident and scattering angles φ' and φ, according to (4.24). The two faces of every corner must be treated separately,

so that the diffraction coefficient $D_{\text{int}}^{1\to 2}$ is evaluated for each face that is illuminated from the inside. Again, in the special case that the transmission point lies on an edge of S, the GO transmitted field must be multiplied by a factor 1/2.

Consequent accounting for all possible combinations of GO transmission and internal diffraction, according to the approach described above, can lead to maximally three different types of transmitted rays:

1. the GO transmitted ray, which passes through two transmission points;

2. single-diffracted rays, which pass through one transmission point and one diffraction point;

3. double-diffracted rays, which pass through two (different) diffraction points.

As an example, Fig. 4.4 shows all possible transmitted rays for a relatively simple configuration. For some of these rays, the categories in which they fall are indicated by bracketed numbers. The transmission points of the GO transmitted ray coalesce if the observation point is located on a shadow boundary of the incident field. Transmitted rays of type (2) with coincident transmission and diffraction points occur for every ray incident on a building corner of which only one face is visible from the source point. Together with the externally diffracted rays that will be discussed in Section 4.2.4, these rays ensure the continuity of the total field across the shadow boundary of the incident field.

4.2.4 External scattering

The scattered fields external to the building that have been considered so far are the result of interaction with the building interior. The fields reflected and diffracted from the building's outer surface, which have not been considered yet, can be predicted by means of "standard" reflection and diffraction models, e.g. by using the Fresnel reflection coefficient discussed in Section 4.2.1 and the diffraction coefficient of Luebbers [43] or Tiberio-Maliuzhinets [44]. Expressions for these fields can also be obtained, however, as part of the theory of the previous sections.

The evaluation of the stationary-phase contributions to an integral of the form (4.27), but with the exterior surface field $E_2(\mathbf{r})$ equal to that in (4.5), cf. [45, 46], leads to a reflected field given by

$$E_2^r(\mathbf{r}_0 + s\hat{\mathbf{k}}_s) = E_2^i(\mathbf{r}_0) R(\mathbf{r}_0) \sqrt{\frac{r_1 r_2}{(r_1+s)(r_2+s)}}\, e^{-jks}, \tag{4.31}$$

which is identical to the expression normally used in the published literature on

deterministic propagation prediction, and to a diffracted field given by

$$E_2^d(\mathbf{r}_0 + s\hat{\mathbf{k}}_s) = E_2^i(\mathbf{r}_0) D_{\text{ext}} \sqrt{\frac{r_1}{s(r_1+s)}}\, e^{-jks}. \tag{4.32}$$

In the latter expression,

$$D_{\text{ext}} = \frac{1}{2}\text{sgn}\big[\hat{\mathbf{t}}\cdot\mathbf{b}\big]\Big[\big(1+R(\mathbf{r}_0)\big)(\hat{\mathbf{n}}\cdot\hat{\mathbf{k}}_s) + \big(1-R(\mathbf{r}_0)\big)(\hat{\mathbf{n}}\cdot\hat{\mathbf{k}}_i)\Big] \times \sqrt{C}\; K_-\left(\sqrt{\frac{kC\big[\hat{\mathbf{t}}\cdot\mathbf{b}\big]^2}{2}}\right) \tag{4.33}$$

is a diffraction coefficient that is complementary to the internal diffraction coefficient (4.20) in the sense that it is valid only if both $\hat{\mathbf{k}}_i$ and $\hat{\mathbf{k}}_s$ point into region 2. Similarly as before, in the calculation of the externally diffracted field from a building corner, D_{ext} must be evaluated separately for each illuminated face of the corner. Also, the reflected field in (4.31) must be multiplied by 1/2 if the reflection point lies on an edge of the reflecting face. The degree of agreement between the coefficient (4.33) and the diffraction coefficients of Luebbers and Tiberio-Maliuzhinets is investigated in the next section.

4.3 Numerical results

The new building transmission model is applied here to a number of simple configurations. One objective of this section is to illustrate how the UTD diffraction coefficients of Taket and Burge, which are part of the new model (view Sections 4.2.2 to 4.2.4), compare with other, more commonly used diffraction coefficients. A second objective is to investigate the relative importance of GO transmitted fields and diffraction fields in (1) the region in the neighbourhood of a building corner that is directly illuminated by the transmitter, and (2) the deep shadow area *behind* a building.

4.3.1 Field around a building corner

First, the diffraction coefficients of Taket and Burge, given by equations (4.20), (4.30) and (4.33), are compared with two diffraction coefficients that are well-known, but cannot be used for penetrable objects: Luebbers' heuristic diffraction coefficient [43] and Tiberio-Maliuzhinets' diffraction coefficient for an impedance wedge [44]. The latter diffraction coefficient is used in conjunction with the reflection coefficient for impedance boundaries [44]. As this is the only diffraction coefficient available to date that has been derived from the exact solution to the canonical problem of

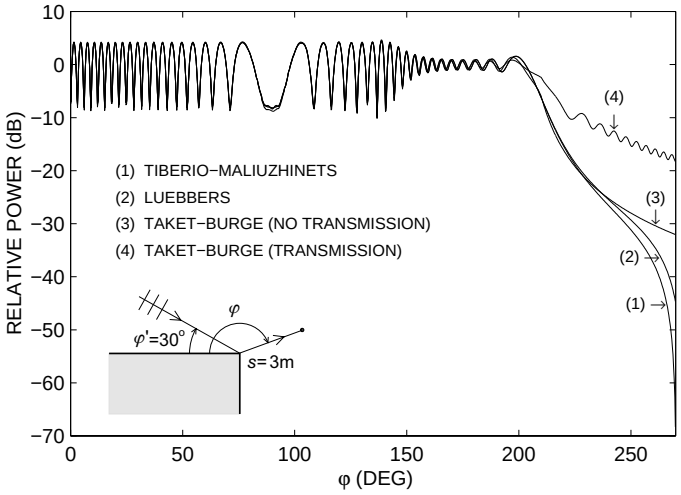

Fig. 4.5: Received power, relative to the free-space level, for a plane-wave illumination of a right-angled wedge. $\epsilon_r = 5$, $\alpha_b = 2.0$ dB/m, $\varphi' = 30^{\mathrm{o}}$, $s = 3$ m.

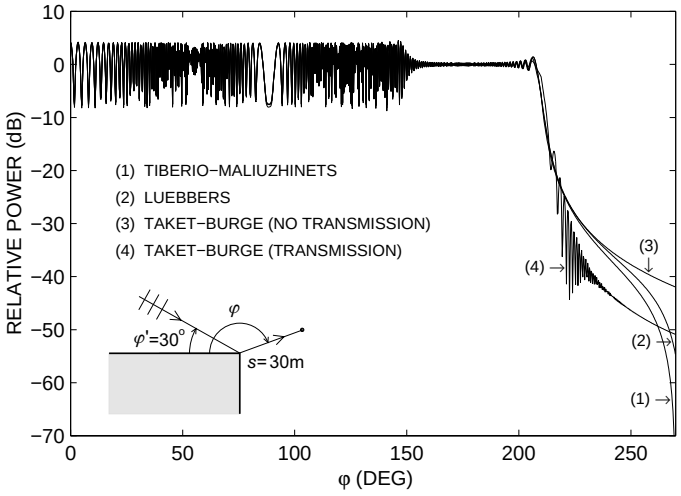

Fig. 4.6: Received power, relative to the free-space level, for a plane-wave illumination of a right-angled wedge. $\epsilon_r = 5$, $\alpha_b = 2.0$ dB/m, $\varphi' = 30^{\mathrm{o}}$, $s = 30$ m.

diffraction from a non-conducting wedge (with impedance faces), it is used here as a reference. Figs. 4.5 and 4.6 show patterns of the total field for a plane wave incident on a right-angled wedge representing a building corner. The incidence angle φ' is 30^o, the permittivity ϵ_r of the building faces is equal to 5 (the conductivity is zero), and the frequency is 1900 MHz. The building attenuation coefficient α_b is chosen equal to 2.0 dB/m. As will be shown in Section 4.4, this is a realistic value. The distance s from the corner to the observation point is 3 m in Fig. 4.5 and 30 m in Fig. 4.6. In both cases, the results for Tiberio-Maliuzhinets, Luebbers and Taket-Burge (external diffraction only) are fairly similar except for the deep shadow region, where they diverge. Especially the heuristic diffraction coefficient of Luebbers provides an excellent approximation of Tiberio-Maliuzhinets.

Very different results are obtained when transmission through the building corner is considered (curves "4" in Figs. 4.5 and 4.6). For $s = 3$ m, close to the building corner, the field in the shadow region is dominated by the GO transmitted ray, and is considerably higher than would be predicted without considering transmission. For $s = 30$ m on the other hand, farther away from the corner, the GO transmitted ray does not play a significant role as it is attenuated considerably in the building interior. As can be seen in Fig. 4.6, in this case the field in the shadow region is actually lower than if transmission is not considered. As it turns out, this is the result of destructive interference between the internally diffracted ray (with coalescent diffraction and transmission points at the building corner) and the externally diffracted ray.

The following conclusions can be drawn regarding the effects of building transmission on propagation around building corners. Increased field strength levels are to be expected only if the observation point is located in the shadow region very near to the building corner. At larger distances from the corner the field is dominated by diffraction contributions. The diffraction coefficients of Taket and Burge provide a reasonable approximation of the more exact diffraction coefficient of Tiberio-Maliuzhinets, but tend to underestimate the diffracted field. However, to the best of the author's knowledge, these are the only diffraction coefficients available to date that can be used for penetrable objects.

4.3.2 Field behind a building

In the scenario of Fig. 4.7, the transmitter is located at a fixed position and the total field is computed along a trajectory behind a single building. As previously, a carrier frequency of 1900 MHz, a permittivity of 5 and an α_b-value of 2.0 dB/m are used. The results are shown in Fig. 4.8, in which the left half of the plot represents the total field (including external and internal diffraction) and the right half shows only the GO field (direct unobstructed and transmitted). The shadow boundaries of the incident field (ISB) and the externally diffracted field (EDSB) are indicated in both

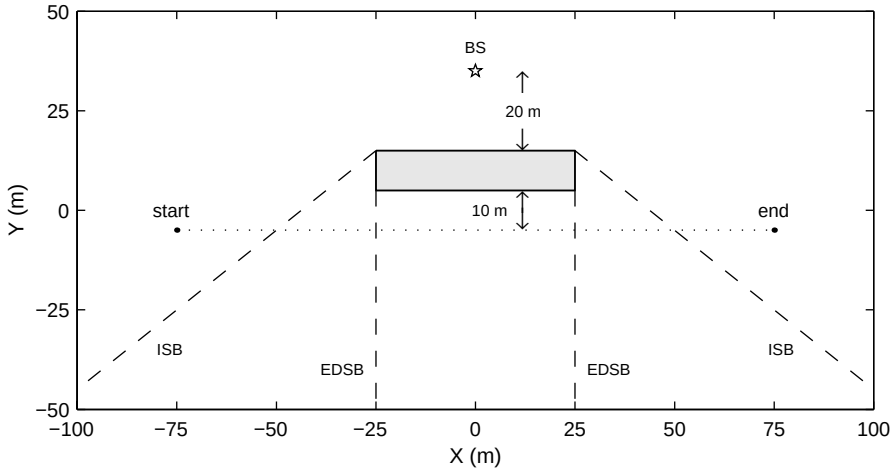

Fig. 4.7: Configuration of the simulated environment. Trajectory and shadow boundaries are indicated by dashed lines. “BS” denotes the base station location.

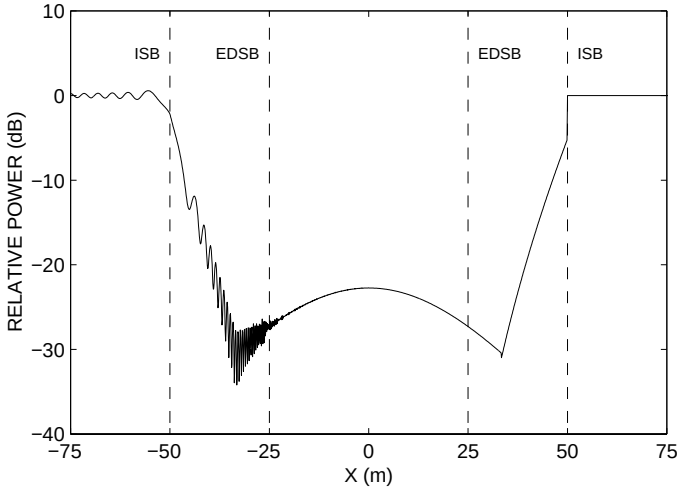

Fig. 4.8: Received power, relative to the free-space level, for the simulated environment ($\epsilon_r = 5$, $\alpha_b = 2.0$ dB/m). Left half of the plot shows the total field; right half shows GO contribution only. Shadow boundaries are indicated by dashed lines.

figures.

From Fig. 4.8 it is obvious that GO transmission plays a dominant role in the GO shadow region between the ISBs. The most significant differences between the total field and the GO field occur around the shadow boundaries and in the vicinity of points where the GO transmitted ray passes through one of the other building corners ($X = \pm 33.3$ m). At these boundaries the GO field exhibits "jumps" while the total field remains continuous. Even in these regions, however, the difference between the two fields is smaller than 4 dB.

It is further seen that the field in the region between the EDSBs (-25 m $< X <$ 25 m in this example) is determined entirely by the GO transmitted field, i.e., contributions from diffracted rays are negligible. This observation forms the basis of the experiments discussed in Section 4.4, in which empirical values of α_b are obtained by fitting the expression for the GO transmitted field to measured data taken in the deep shadow area directly behind a building.

4.4 Experimental results

The free parameter α_b used in the transmission model of Section 4.2 is related to the internal building structure in a highly complicated way and must therefore be determined empirically, i.e., from measurements of the path loss – relative to the free-space loss – experienced by waves transmitted through buildings. This excess path loss will be referred to as the building transmission loss L_t.

A major concern in the measurement of building transmission losses is formed by the disturbing effect of multipath contributions entering the receiving antenna via objects in the environment of the considered building. A solution to this problem may be found in the use of wideband and/or directional measurement techniques, which offer the possibility to separate multipath waves on the basis of their different propagation delay times and angles-of-arrival (AOAs), respectively [16]. Using a combination of these techniques, it was demonstrated in [53] that it is indeed possible to distinguish the radiowaves transmitted through an obstructing building from other multipath contributions in a realistic microcell environment. However, important practical disadvantages of this method are the relatively complex measurement procedure and the long time needed to measure the transmitted field, even for a single receiver location.

This section introduces a fast, simple and yet accurate method to measure the transmitted field along a trajectory behind an obstructing building, using a wideband radio channel sounder [54]. Furthermore, it presents results of building transmission loss measurements for a set of 22 buildings that can be considered typical for urban environments in The Netherlands. Empirical values of the attenuation coefficient α_b

are determined for each of these buildings.

4.4.1 Measurement equipment and procedure

The building transmission measurements discussed in this section were performed using the TU/e radio channel sounding system that was described in detail in Section 2.2 of this thesis. This system operates at 1900 MHz and has a temporal resolution of 20 ns. Instead of the rotating antenna that was used to estimate the AOA of multipath waves, a fixed, vertically polarised, omnidirectional receiving antenna was mounted on the roof of a measurement vehicle, at 2.4 m above ground level. The radiation patterns of this antenna are shown in Fig. 2.3 on page 13 of this thesis.

The transmitting antenna – a vertically polarised, 12-dBi, omnidirectional antenna with a vertical 3-dB beamwidth of 6^o – was positioned on one of the long sides of the building under test, at a height of 6.5 m, typical for the base station configuration in urban microcells. During a measurement, impulse response data were recorded every 0.1 s while the measurement vehicle was moving at a low, constant speed (usually around 1.5 m/s) along a straight trajectory on the other side of the building. Road lay-out and other local circumstances influenced the final choices of the transmitting antenna location and the measurement trajectory.

4.4.2 Determination of the transmitted field

To illustrate how the absolute transmitted field strength can be determined from the impulse response data, a typical data set – measured behind a 15-m high office building on the TU/e campus (view the plan in Fig. 4.9 and the photograph in Fig. 4.14(f) on page 73 of this thesis) – is shown in Fig. 4.10. In this measurement, the transmitting antenna was at the location marked as "Tx1" in Fig. 4.9. The major part of the building consists of small offices separated by brick walls, with wooden doors opening to a central corridor. A large restaurant hall is situated in the right part. The building has a concrete, metal and glass external construction.

The set of power delay profiles recorded along the trajectory is denoted by $p(\tau; d)$, τ being the propagation delay time and d being the distance along the trajectory. For each d, the values of τ for which $p(\tau; d)$ has local maxima form estimates of the propagation delays of the dominant multipaths. The values of $p(\tau; d)$ at each of these τs is proportional to the multipath intensity. The proportionality factor between the two can be determined prior to the measurement by connecting a known attenuation between the transmitter and receiver.

The received field is composed of several multipath waves propagating around the building via reflection, diffraction and scattering from surrounding objects, and a contribution due to transmission through the building. The waves propagating around the building arrive at the receiving antenna roughly from the front and back

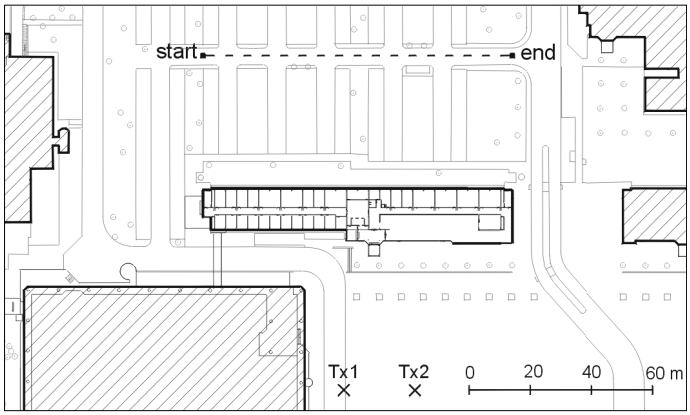

Fig. 4.9: Plan view of the measurement environment.

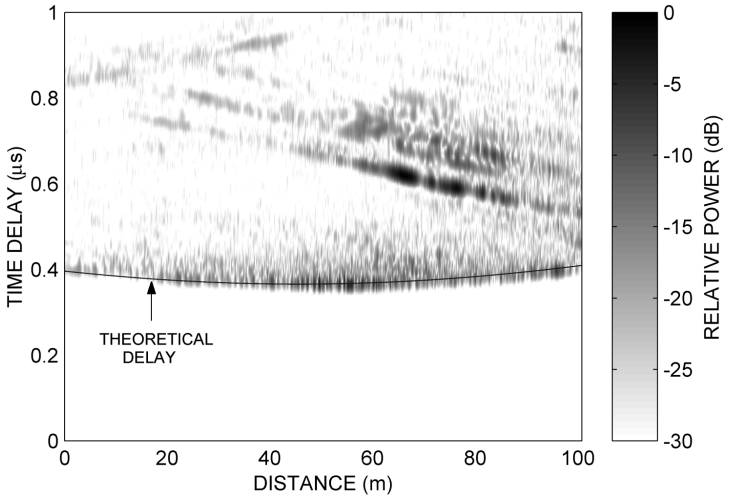

Fig. 4.10: Measured power delay profiles along the trajectory.
Transmitter is at location “Tx1”.

of the vehicle. As the distance along the trajectory increases, the profile maxima corresponding to these waves move along the delay axis at an approximately constant rate (see Fig. 4.10). The sign of this rate depends on whether a wave propagates around the left or the right side of the building. Generally, as in Fig. 4.10, the first transmitted contribution can easily be identified by its hyperbolic shape and because it has minimum delay for all d. The weaker "clutter" arriving directly after this first contribution is possibly the result of waves undergoing (multiple) backward and forward reflection in the building interior, and will be ignored.

To simplify the determination of the transmitted field, the building is modelled as a rectangular box having the same length as the building behind which the measurement was made, and a width equal to its maximum width (view Fig. 4.11). Diffraction effects – which are insignificant in the deep shadow region directly behind the building (view Section 4.3) – are neglected, and the transmitted field is assumed to be the result of a single GO transmitted ray propagating directly from the transmitting antenna through the building to the receiving antenna, at a propagation velocity equal to that in free space (cf. Section 4.2). In Fig. 4.10, the solid line represents the theoretical delay $\tau_t(d)$ associated with the GO transmitted ray. This delay is seen to be in very good agreement with the measured delay of the first transmitted contribution. The absolute transmitted field strength, required to determine L_t, is obtained from $p(\tau; d)$ by setting $\tau = \tau_t(d)$ and multiplying by the proportionality factor found in the calibration.

4.4.3 Determination of the attenuation coefficient

The thin solid line in Fig. 4.12 represents the measured building transmission loss for the example discussed in the previous section. This loss exhibits strong and rapid spatial fluctuations, which indicates that, in reality, the transmitted field is the result of two or more waves propagating along paths of approximately the same length. These fast fading effects are neglected for the purpose of fitting the proposed model to the global behaviour of the measured transmitted field. The large-scale fading component of the measured L_t, represented in Fig. 4.12 by the thick solid line, is obtained by averaging over 40 wavelengths [55], which corresponds to approximately 6 m.

According to the transmission model of Section 4.2, the building transmission loss experienced by the GO transmitted field is equal to

$$L_t = \alpha_b \cdot d_{\text{in}} - 20 \log\left|T(\mathbf{r}_1)\right| - 20 \log\left|T(\mathbf{r}_2)\right| \qquad \text{dB}, \tag{4.34}$$

where d_{in} is the length of the transmitted ray path inside the building, $\mathbf{r}_1$ and $\mathbf{r}_2$ are the transmission points on the building surface, and $T(\mathbf{r}_1)$ and $T(\mathbf{r}_2)$ are the associated transmission coefficients (view Fig. 4.11). In the case considered here, the angles

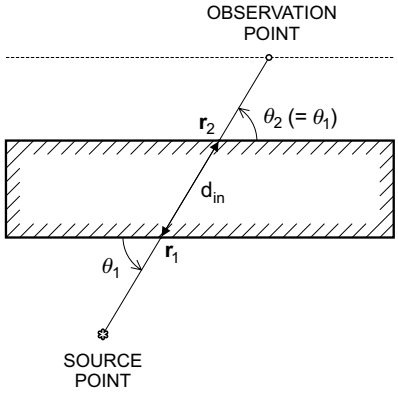

Fig. 4.11: Illustration of the simplified building model.

θ_1 and θ_2 are equal, so that $T(\mathbf{r}_1) = T(\mathbf{r}_2)$. Note that the above expression for L_t follows from equations (4.16) and (4.28), after converting to decibels and subtracting the free-space loss.

The specific attenuation factor α_b is chosen such that the root-mean-square (rms) error of the theoretical L_t with respect to the averaged measured data is minimised. For the example under consideration, this results in a value of $\alpha_b = 1.51$ dB/m (for $\epsilon_r = 5$), and the rms error is 5.76 dB. The dashed line in Fig. 4.12 represents the theoretical L_t computed using these parameters. In this particular example, it would be possible to reduce the rms error by using different values of α_b for the left and the right half of the building, thus reflecting the fact that there are more internal walls in the left section (view Fig. 4.9).

4.4.4 Reproducibility

In order to assess the reliability of the transmission loss measurements and the determination of α_b, the reproducibility of the experimental results was investigated for the building under present consideration. Important factors that could cause two subsequent measurements to yield different results are (1) non-stationarity of the environment, mainly because of movements inside the building, and (2) difficulty to conduct the measurements at exactly the same observation points [48]. The lower curve in Fig. 4.12 represents the result of a second measurement along the same trajectory, with the transmitting antenna at location "Tx1". Apart from a small misalignment in distance, caused by speed variations of the measurement vehicle, this result is almost identical to that of the first measurement. Fig. 4.13 shows the results of two consecutive measurements along the same trajectory, but with the transmitting antenna at location "Tx2" (view Fig. 4.9). Again, the measured L_t-curve is seen

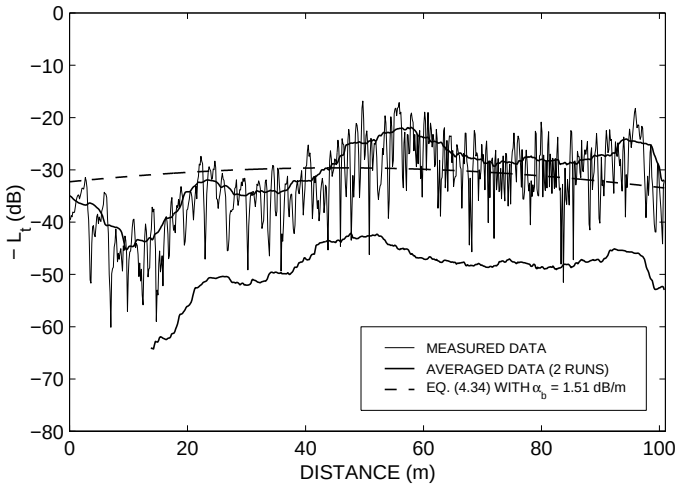

Fig. 4.12: Measured and modelled building transmission loss L_t (transmitting antenna at location “Tx1”). Lower curve has an offset of -20 dB for clarity.

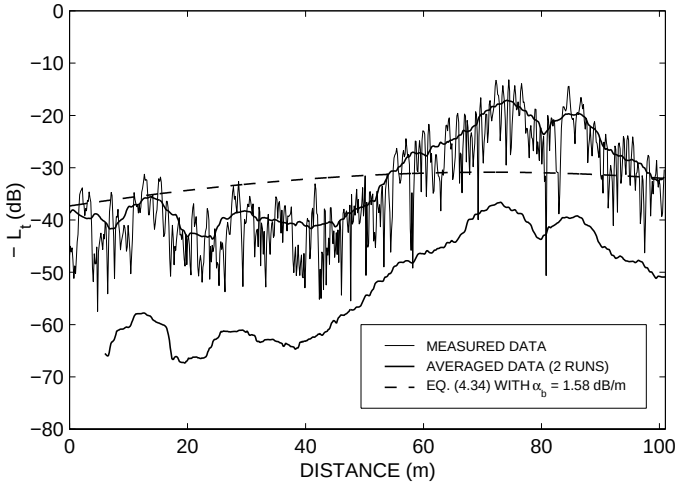

Fig. 4.13: Measured and modelled building transmission loss L_t (transmitting antenna at location “Tx2”). Lower curve has an offset of -20 dB for clarity.

to be well reproducible. Although there is a significant difference with respect to the result for antenna position "Tx1", the value of α_b obtained for position "Tx2" is close to the first value, viz. 1.58 dB/m. This indicates that the measured α_b is not very sensitive to the exact measurement configuration, and that it is indeed inherent to the internal properties of the building.

4.4.5 Description of the buildings

The buildings selected for the measurements can be roughly classified into the four categories listed in Table 4.1. Although it might be argued that residential houses (category 1) are more typical of suburban than urban environments, this type of building is sometimes also found in city centres and was therefore not left out of consideration. A list of all buildings and their external properties is given in Table 4.2. For buildings consisting of different sections with different heights, the minimum height is specified. For the six buildings in Table 4.2 that are marked with an asterisk, plots of the measured building transmission loss L_t are presented and discussed in the next section. Photographs of these buildings are shown in Fig. 4.14. The office building on the TU/e campus that was discussed previously is referred to as building 22 in Table 4.2. A photograph of this building is shown in Fig. 4.14(f).

Table 4.1: Building categories.

Category	Description
1	Residential houses
2	Multi-storey residential buildings (flats)
3	Mixed commercial/residential buildings
4	Office buildings

4.4.6 Results

By means of the procedure described in Sections 4.4.2 and 4.4.3, the building transmission loss L_t and the corresponding best fit of α_b were determined for all buildings listed in Table 4.2. Figs. 4.15(a)–(f) show the measured L_t-curves for six of these buildings. For each of the total number of 22 buildings, the empirical value of α_b and the corresponding rms modelling error is given in the Tables 4.3–4.6, as well as the range in which the averaged measured building transmission loss lies. Overall, this range extends roughly from 20 to 40 dB.

In general, expression (4.34) provides a good fit to the measured data when the attenuation factor α_b is optimised for the building under consideration (rms errors

Table 4.2: Exterior properties of the buildings selected for the experiments.

Building	Cat.	External-side building materials	External dimensions†		
			L (m)	W (m)	H (m)
1	1	brick / window glass / ceramic roof tiles	47	10	8
2	1	painted wood / window glass / concrete roof tiles	46	10	9
3*	1	brick / window glass / concrete roof tiles	73	9	9
4	1	brick / window glass / ceramic roof tiles	36	8	8
5	1	brick / window glass / ceramic roof tiles	73	7	9
6	2	brick / window glass	57	11	23
7	2	brick / wooden panels / window glass	74	11	12
8	2	brick / window glass	119	20	14
9*	2	reinforced concrete covered with insulating material / glass windows / metal railings	98	12	26
10	2	brick / window glass / metal railings	67	19	22
11	3	brick / window glass	65	9	9
12	3	brick / cement panels / window glass	36	12	9
13	3	brick / cement panels / window glass	49	12	9
14*	3	brick / cement panels / window glass	36	12	9
15*	3	brick (ground floor) / concrete panels (upper storeys) / window glass	58	15	10
16	4	brick / window glass	23	13	10
17	4	concrete panels / window glass	51	13	12
18	4	concrete block / dark-tinted window glass	62	13	14
19*	4	reinforced concrete shell / reflective window glass	40	14	23
20	4	reinforced concrete shell / reflective window glass	45	13	26
21	4	concrete panels / window glass	39	14	18
22*	4	reinforced concrete covered with metal panels / window glass / metal railings	102	18	15

† L(ength) × W(idth) × H(eight).

* Photographs of these buildings are shown in Fig. 4.14.

(a) Building 3

(b) Building 9

(c) Building 14

(d) Building 15

(e) Building 19

(f) Building 22

Fig. 4.14: Photographs of six of the buildings selected for the experiments.

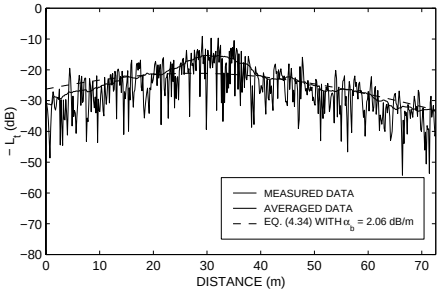

(a) Building 3

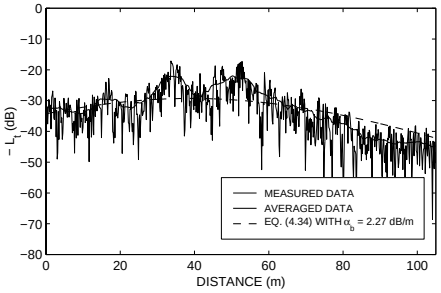

(b) Building 9

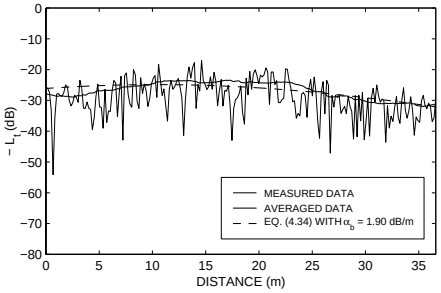

(c) Building 14

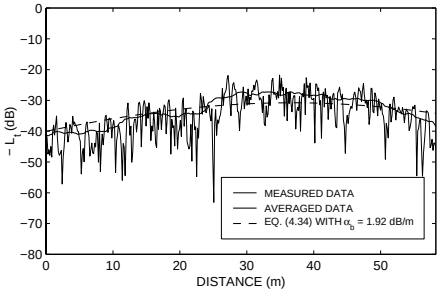

(d) Building 15

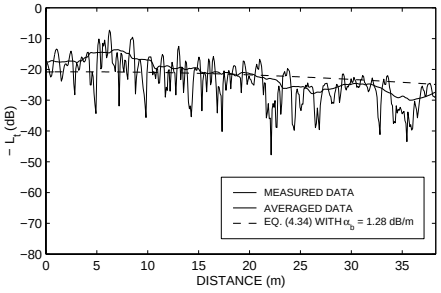

(e) Building 19

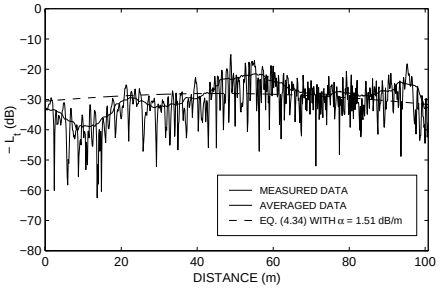

(f) Building 22

Fig. 4.15: Measured and modelled building transmission loss L_t for six of the buildings selected for the experiments.

Table 4.3: Measured transmission characteristics for the buildings of category 1.

Building	Empirical α_b (dB/m)	Rms error (dB)	Range of measured L_t (dB)
1	1.82	2.07	16–27
2	1.96	3.05	17–30
3	2.06	2.55	15–34
4	2.51	1.36	21–28
5	2.94	4.17	14–38
Average	2.26	2.64	–

Table 4.4: Measured transmission characteristics for the buildings of category 2.

Building	Empirical α_b (dB/m)	Rms error (dB)	Range of measured L_t (dB)
6	1.74	3.65	15–30
7	1.72	4.73	14–34
8	1.49	3.61	30–49
9	2.27	3.73	22–45
10	1.65	2.97	28–47
Average	1.77	3.74	–

Table 4.5: Measured transmission characteristics for the buildings of category 3.

Building	Empirical α_b (dB/m)	Rms error (dB)	Range of measured L_t (dB)
11	1.91	2.72	16–29
12	1.93	2.27	21–34
13	1.65	1.34	20–25
14	1.90	1.53	23–32
15	1.92	2.29	27–41
Average	1.86	2.03	–

Table 4.6: Measured transmission characteristics for the buildings of category 4.

Building	Empirical α_b (dB/m)	Rms error (dB)	Range of measured L_t (dB)
16	1.91	1.63	26–33
17	2.26	1.63	31–41
18	3.69	1.51	51–64
19	1.28	3.53	14–30
20	1.85	3.01	22–35
21	1.90	2.74	24–40
22	1.51	5.76	22–45
Average	2.06	2.83	–

around 3 dB). Building 22, which was taken as an illustrative example in this chapter, represents a "worst case" in that the rms error achieved for this building is the highest of all buildings tested (5.76 dB). This relatively large error can be explained by the building's internal inhomogeneity (view Fig. 4.9).

The 22 buildings tested can be characterised rather well by the average α_b-values of their respective categories, which are in turn all close to the total average value of $\alpha_b = 2.0$ dB/m. This is a strong indication that the presented model, in combination with an α_b-value of 2.0 dB/m, has considerable predictive value. The largest spread around the average value is observed in category 4 (office buildings). This is possibly the result of the widely different internal layouts and the diversity of building materials used in this category. The layout and materials of the buildings in the other categories are much more uniform.

4.5 Conclusions

A ray-optical model has been presented which describes the penetration of radiowaves into buildings and their transmission through buildings. This model can be used as a seemless extension to ray-tracing-based propagation models that only take into account external reflection and diffraction, as do most current models. It introduces two additional types of radiowave interaction with buildings, viz. GO transmission through their outer walls and internal diffraction from their corners. The new model requires information about the buildings' exterior coordinates and permittivity ϵ_r, and a suitable choice of the attenuation factor α_b, which is related to the internal building structure.

Numerical investigations indicate that the diffraction coefficients of Taket and Burge that are used in the transmission model provide a reasonably good approximation of the more exact diffraction coefficient of Tiberio-Maliuzhinets, but tend to underestimate the diffracted field. However, they are the only diffraction coefficients available to date that can be used for penetrable objects. GO transmission through building corners is significant only in the vicinity of the corner. Farther away, the field is determined mainly by diffraction contributions. Diffraction effects are negligible in the deep shadow *behind* buildings, where the field is entirely determined by GO transmission.

For a given value of ϵ_r, the parameter α_b of a building can be obtained by fitting the expression for the GO transmitted field to measured values of the building transmission loss L_t in the building's deep shadow. By means of a simple and accurate method that was also presented in this chapter, measurements of L_t were carried out for a set of 22 buildings. The results of these measurements show that L_t is usually in the range between 20 and 40 dB. This is low considering the fact that (externally)

diffracted fields in the shadow area of a building can easily be more than 40 dB below the free-space level. For accurate prediction of the field strength in such heavily shadowed regions, which are typical for urban microcells, taking into account the transmitted rays is of great importance.

Empirical α_b-values obtained in the present study (assuming a permittivity of 5 and zero conductivity) range from 1.3 to 3.7 dB/m, but most are concentrated around the average value of 2.0 dB/m. Therefore, if it is not feasible to determine α_b for each individual building, as will be usually the case in the practice of network planning, no large prediction errors are expected if all buildings are characterised by this average value.

An important benefit of the new transmission model is that it automatically accounts for outdoor-to-indoor propagation, i.e. the penetration of radiowaves into buildings. This phenomenon is receiving increased attention as indoor coverage is becoming an important aspect of mobile network quality. It is noted, however, that the present model can only be expected to provide good results for building penetration at the ground level, due to its two-dimensional nature. A different model has to be used for the prediction of indoor field strength levels at higher floors.

5

Scattering from trees

5.1 Introduction

In Chapter 3 of this thesis it was observed that the scattering of radiowaves from trees, which are abundantly found in most European cities, is an important propagation mechanism. Investigations of tree effects on radio channel characteristics have hitherto been restricted mainly to coherent scattering, of which the attenuation of waves propagating through the foliage ("tree shadowing") is the most obvious manifestation [56, 57]. Incoherent scattered fields – which are due to the macroscopic dielectric heterogeneity of the medium formed by the tree canopy – are often neglected, even though they are generally predominant over the coherent scattered field in directions other than the forward direction. In scenarios where the line-of-sight path is obstructed and reflected and diffracted multipath contributions are weak, incoherent tree-scattered fields can become dominant. A specific case in which scattering from trees plays an important role was discussed in Section 3.3. The experimental results discussed in that section indicate that the fields scattered from trees located near a street intersection can be more significant than the fields diffracted by the building corners. Considering the effects of incoherent tree scattering can therefore lead to a better modelling of radiowave propagation around street corners.

This chapter presents a new theoretical model for the coherent and incoherent scattering from deciduous trees. As this model finds its application in propagation

prediction for urban microcell environments, it is kept quasi-two-dimensional. This means that it will be assumed that the reception point and the source of the incident field are both at the same height as the centre of the tree canopy, and that the canopy is very high. The wave propagation is in three-dimensional space, as usual. Furthermore, attention is restricted to the vertically polarised field components, and hence the final expressions for the scattered fields are scalar. The tree itself is assumed to consist of a high, but finite cylindrical volume containing randomly located and oriented branches and leaves, modelled as dielectric cylinders and disks, as in [57–59]. The effects of the trunk are neglected.

As in previous tree-scattering models, the coherent field in the canopy is computed using the multiple scattering theory of Foldy and Twersky [60]. However, unlike these earlier models, the (coherent and incoherent) scattered fields outside the canopy are obtained as the approximate solutions to a set of integral equations, each involving an integration over the canopy volume. Due to their mathematical form, these solutions are particularly suitable for use in ray-based propagation models.

This chapter is organised as follows. Section 5.2 describes the overall scattering geometry and provides expressions for the scattering from branches and leaves. A model for the scattering of radiowaves from an entire tree canopy is developed in Section 5.3. The expressions derived in that section, as well as the underlying assumptions and simplifications, are largely original contributions. In Section 5.4, numerical results generated using these expressions are presented, and the accuracy of the approximations made in their derivation is investigated. A comparison with experimental data is made in Section 5.5. Conclusions are drawn in Section 5.6.

5.2 Vegetation model

From the standpoint of radiowave propagation, a vegetation canopy is a bounded medium consisting of many discrete, randomly distributed and oriented, dielectric inclusions (branches, leaves, fruit, etc.) in a homogeneous background material (air). Although the medium may, in general, be random in both space and time, in the present study the canopy structure and, consequently, the scattered field are assumed to be time-invariant. At the frequencies used for mobile communications, the dimensions of the inclusions can be comparable to or larger than the wavelength. This means that the canopy cannot be treated as a macroscopically homogeneous dielectric mixture, characterised by an effective dielectric permittivity. Instead, the geometries and orientations of the various types of inclusions present in the canopy also have to be taken into account.

In the present study, a tree canopy is assumed to consist of an ensemble of leaves and branches. Leaves are modelled as thin, lossy dielectric disks and branches as fi-

nite, lossy dielectric cylinders. A consequence of the dielectric heterogeneity of the canopy volume is that the scattered field has an incoherent (or diffuse) component, which consists of uncorrelated contributions from the individual scatterers. For short propagation paths through random media, the incoherent scattered field in the forward direction is generally small compared to the coherent scattered field. For this reason the incoherent scattered field is often disregarded in the literature dealing with tree scattering (attenuation) effects in terrestrial radiowave propagation. However, as will be shown later in this chapter, this incoherent field is much more important than the coherent field in scattering directions other than the forward direction.

5.2.1 Overall problem geometry

Consider the tree canopy in Fig. 5.1, modelled as a vertically oriented, high but finite cylindrical volume V in a rectangular coordinate system defined by the orthonormal vectors $\hat{\mathbf{x}}$, $\hat{\mathbf{y}}$ and $\hat{\mathbf{z}}$. This coordinate system, of which the origin $\mathbf{r}_0$ is located at the centre of the canopy, will be referred to as the reference frame. The radius R and the height H describe the dimensions of V. The canopy volume contains randomly distributed and oriented branches and leaves, the former of which can be classified into N_b different size categories. Their number densities are represented by ρ_b and ρ_l, respectively, where the subscript b is an element of $\{b_1, b_2, \ldots, b_{N_b}\}$ and b_n is used to denote branches of the nth size category.

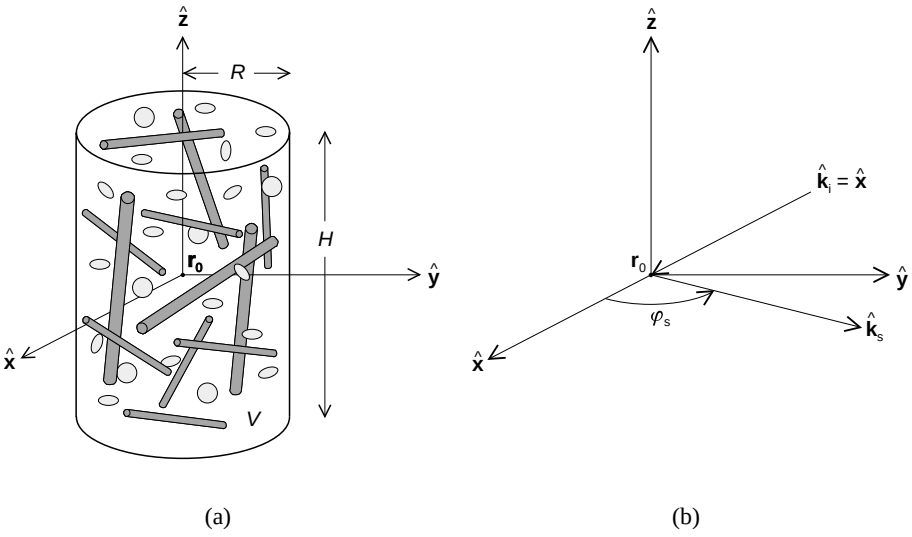

(a) (b)

Fig. 5.1: Problem geometry. (a) Canopy volume. (b) Incident and scattered directions.

Incident on the canopy is a vertically polarised wave with wavelength λ and direction of propagation $\hat{\mathbf{k}}_i$ relative to the canopy centre. The source of this wave is assumed to be located far away from the canopy, so that the incident field amplitude can be approximated as being constant over the canopy volume. The incident wave is scattered in all directions by the scatterers in the canopy volume, and the scattered field is observed at an observation point, also located far away from the canopy, in the direction $\hat{\mathbf{k}}_s$ relative to the canopy centre. The unit vectors $\hat{\mathbf{k}}_i$ and $\hat{\mathbf{k}}_s$ are perpendicular to $\hat{\mathbf{z}}$, and φ_s denotes the azimuthal scattering direction. Without loss of generality, it is assumed that $\hat{\mathbf{k}}_i = \hat{\mathbf{x}}$.

The problem dealt with in Section 5.3 is to compute the mean and variance of the (vertical component of the) scattered field at the observation point. The scattering amplitude functions of the branches and leaves, as well as some other equations required for the computations in Section 5.3, are given in the remainder of the present section (Sections 5.2.2 to 5.2.4). These equations are mostly taken from the published literature, in particular from [58, 59, 61].

5.2.2 Scattering from branches

Tree branches are composed of several concentric tissue layers (wood, bark, etc.), each of which is made up of many cells that are much smaller than the wavelengths normally used for mobile communications. Although it has been shown that the effective dielectric properties of the branch material can be different from one tissue layer to the other, and even anisotropic [62], for simplicity branches are modelled here as homogeneous dielectrics with an effective complex dielectric permittivity ϵ_b.

Consider the finite-length, lossy dielectric cylinder in the rectangular coordinate system defined by the orthonormal vectors $\hat{\mathbf{x}}'$, $\hat{\mathbf{y}}'$ and $\hat{\mathbf{z}}'$. This coordinate system will be called the local frame of the cylinder. In the local frame, the incident and scattered direction vectors $\hat{\mathbf{k}}_i$ and $\hat{\mathbf{k}}_s$ are defined by the angles θ_i', φ_i', θ_s' and φ_s' (view Fig. 5.2). The cylinder has length h_b and radius r_b, and is oriented parallel to $\hat{\mathbf{z}}'$. The scattering of an arbitrarily polarised wave incident on the cylinder can be described in terms of a scattering amplitude tensor. If the field inside the cylinder is estimated as the field inside a similar, but infinite cylinder, the elements of this tensor are given by [58, 59]

$$\begin{aligned} f_{vv}^b(\hat{\mathbf{k}}_s, \hat{\mathbf{k}}_i) \;=\; & \frac{k^2 h_b}{2}(\epsilon_b - 1)\mu_b(\hat{\mathbf{k}}_s, \hat{\mathbf{k}}_i)\Bigg\{ e_{0v}(B_0 \cos\theta_s' \cos\theta_i' - \sin\theta_s' z_0) \\ & + 2\sum_{n=1}^{\infty}\Big[(e_{nv}\cos\theta_i' B_n - j\eta h_{nv} A_n)\cos\theta_s' \\ & - \sin\theta_s' e_{nv} z_n\Big]\cos\Big[n(\varphi_i' - \varphi_s')\Big]\Bigg\} \end{aligned} \tag{5.1a}$$

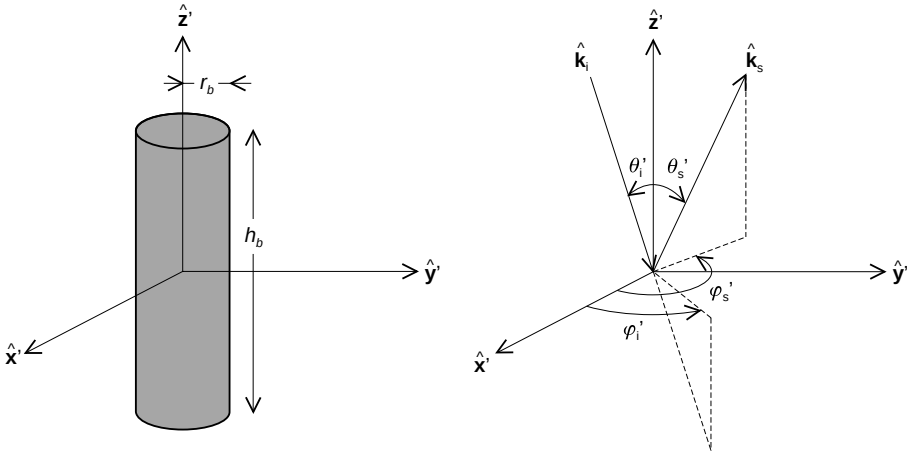

(a) (b)

Fig. 5.2: Branch scattering geometry. (a) Branch volume. (b) Incident and scattered directions in the local frame.

$$f_{vh}^{b}(\hat{\mathbf{k}}_s,\hat{\mathbf{k}}_i) = jk^2h_b(\epsilon_b-1)\mu_b(\hat{\mathbf{k}}_s,\hat{\mathbf{k}}_i)\sum_{n=1}^{\infty}\Big[(e_{nh}\cos\theta_i' B_n - j\eta h_{nh}A_n)\cos\theta_s' - \sin\theta_s' e_{nh} z_n\Big]\sin\Big[n(\varphi_s'-\varphi_i')\Big] \tag{5.1b}$$

$$f_{hv}^{b}(\hat{\mathbf{k}}_s,\hat{\mathbf{k}}_i) = jk^2h_b(\epsilon_b-1)\mu_b(\hat{\mathbf{k}}_s,\hat{\mathbf{k}}_i) \times\sum_{n=1}^{\infty}\big(\eta h_{nv}B_n + je_{nv}\cos\theta_i' A_n\big)\sin\Big[n(\varphi_s'-\varphi_i')\Big] \tag{5.1c}$$

$$f_{hh}^{b}(\hat{\mathbf{k}}_s,\hat{\mathbf{k}}_i) = \frac{k^2h_b}{2}(\epsilon_b-1)\mu_b(\hat{\mathbf{k}}_s,\hat{\mathbf{k}}_i)\Big\{B_0\eta h_{0h} + 2\sum_{n=1}^{\infty}\big(\eta h_{nh}B_n + je_{nh}\cos\theta_i' A_n\big)\cos\Big[n(\varphi_s'-\varphi_i')\Big]\Big\}. \tag{5.1d}$$

In these expressions, the subscripts "v" and "h" indicate the vertical and horizontal components of the scattered and incident waves, respectively, relative to the local frame of the scatterer. The function $\mu_b(\hat{\mathbf{k}}_s,\hat{\mathbf{k}}_i)$ is a so-called modifying function which reduces to unity when the scatterer becomes very small compared with the

wavelength (Rayleigh scattering) [58]. It is given by

$$\mu_b(\hat{\mathbf{k}}_s, \hat{\mathbf{k}}_i) = \frac{\sin\big[kh_b(\cos\theta_i' + \cos\theta_s')/2\big]}{kh_b(\cos\theta_i' + \cos\theta_s')/2}. \tag{5.2}$$

The parameter $k = 2\pi/\lambda$ is the free-space wavenumber. Furthermore,

$$e_{nv} = \frac{j\sin\theta_i'}{R_n J_n(u)}\left\{\frac{H_n^{(2)\prime}(v_i)}{v_i H_n^{(i)}} - \frac{J_n'(u)}{uJ_n(u)}\right\} \tag{5.3a}$$

$$\eta h_{nv} = \frac{\sin\theta_i'}{R_n J_n(u)}\left(\frac{1}{v_i^2} - \frac{1}{u^2}\right)n\cos\theta_i' \tag{5.3b}$$

$$e_{nh} = \frac{-\sin\theta_i'}{R_n J_n(u)}\left(\frac{1}{v_i^2} - \frac{1}{u^2}\right)n\cos\theta_i' \tag{5.3c}$$

$$\eta h_{nh} = \frac{j\sin\theta_i'}{R_n J_n(u)}\left\{\frac{H_n^{(2)\prime}(v_i)}{v_i H_n^{(i)}} - \frac{\epsilon_b J_n'(u)}{uJ_n(u)}\right\} \tag{5.3d}$$

$$R_n = \frac{\pi v_i^2 H_n^{(2)}(v_i)}{2}\left\{\left(\frac{H_n^{(2)\prime}(v_i)}{v_i H_n^{(2)}(v_i)} - \frac{J_n'(u)}{uJ_n(u)}\right)\right. \tag{5.3e}$$

$$\left.\times\left(\frac{H_n^{(2)\prime}(v_i)}{v_i H_n^{(2)}(v_i)} - \frac{\epsilon_b J_n'(u)}{uJ_n(u)}\right) - \left(\frac{1}{u^2} - \frac{1}{v_i^2}\right)^2 n^2\cos^2\theta_i'\right\} \tag{5.3f}$$

$$A_n = \frac{k}{2\lambda_i}(z_{n-1} - z_{n+1}) \tag{5.3g}$$

$$B_n = \frac{k}{2\lambda_i}(z_{n-1} + z_{n+1}) \tag{5.3h}$$

$$\lambda_i = k\sqrt{\epsilon_b - \cos^2\theta_i'} \tag{5.3i}$$

$$z_n = \frac{r_b^2}{u^2 - v_s^2}\big[uJ_n(v_s)J_{n+1}(u) - v_s J_n(u)J_{n+1}(v_s)\big] \tag{5.3j}$$

$$u = \lambda_i r_b \tag{5.3k}$$

$$v_i = kr_b\sin\theta_i' \tag{5.3l}$$

$$v_s = kr_b\sin\theta_s'. \tag{5.3m}$$

In these equations, $H_n^{(2)}(\cdot)$ and $J_n(\cdot)$ are the Bessel function of the first kind and the Hankel function of the second kind, respectively, and $H_n^{(2)\prime}(\cdot)$ and $J_n'(\cdot)$ are their derivatives with respect to the argument.

5.2.3 Scattering from leaves

Foliage leaf material is typically formed by a number of tissue layers, each consisting of many cells of complex composition. However, as the cell dimensions and

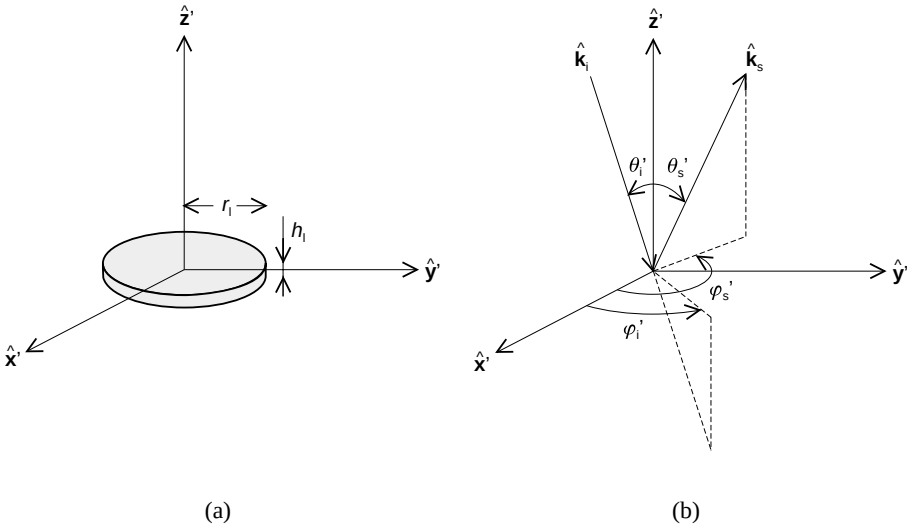

(a) (b)

Fig. 5.3: Leaf scattering geometry. (a) Leaf volume. (b) Incident and scattered directions in the local frame.

layer thicknesses are typically much smaller than the wavelength, the interaction of radiowaves with leaves can be well modelled by treating each leaf as a homogeneous dielectric with an effective complex permittivity ϵ_l.

For a thin, circular disk with radius r_l and thickness h_l (h_l small compared with the wavelength, so that $kh_l[\sqrt{\epsilon_l} - 1] \ll 1$), and with its axis of symmetry aligned with the z'-axis of the local frame (view Fig. 5.3), the scattering amplitude tensor elements can be estimated as [59]

$$f^l_{vv}(\hat{\mathbf{k}}_s, \hat{\mathbf{k}}_i) = \frac{k^2(\epsilon_l - 1)v_l}{4\pi}\mu_l(\hat{\mathbf{k}}_s, \hat{\mathbf{k}}_i) \times \left[a_N \sin\theta'_i \sin\theta'_s - a_T \cos\theta'_i \cos\theta'_s \cos(\varphi'_s - \varphi'_i)\right] \tag{5.4a}$$

$$f^l_{vh}(\hat{\mathbf{k}}_s, \hat{\mathbf{k}}_i) = \frac{k^2(\epsilon_l - 1)v_l}{4\pi}\mu_l(\hat{\mathbf{k}}_s, \hat{\mathbf{k}}_i) \cos\theta'_s \sin(\varphi'_s - \varphi'_i) a_T \tag{5.4b}$$

$$f^l_{hv}(\hat{\mathbf{k}}_s, \hat{\mathbf{k}}_i) = \frac{k^2(\epsilon_l - 1)v_l}{4\pi}\mu_l(\hat{\mathbf{k}}_s, \hat{\mathbf{k}}_i) \cos\theta'_i \sin(\varphi'_s - \varphi'_i) a_T \tag{5.4c}$$

$$f^l_{hh}(\hat{\mathbf{k}}_s, \hat{\mathbf{k}}_i) = \frac{k^2(\epsilon_l - 1)v_l}{4\pi}\mu_l(\hat{\mathbf{k}}_s, \hat{\mathbf{k}}_i) \cos(\varphi'_s - \varphi'_i) a_T. \tag{5.4d}$$

In these expressions, $v_l = \pi h_l r_l^2$ is the leaf volume, and

$$\mu_l(\hat{\mathbf{k}}_s, \hat{\mathbf{k}}_i) = \frac{2J_1(Q_{si} r_l)}{Q_{si} r_l} \tag{5.5a}$$

$$Q_{si} = k\sqrt{\sin^2\theta_s' + \sin^2\theta_i' - 2\sin\theta_s' \sin\theta_i' \cos(\varphi_s' - \varphi_i')} \tag{5.5b}$$

is a modifying function similar to that in (5.2). Furthermore, under the reasonable assumption that $h_l \ll r_l$, a_N and a_T are given by [59]

$$a_N = \epsilon_l^{-1} \quad \text{and} \quad a_T = 1. \tag{5.6}$$

5.2.4 Equivalent scattering amplitude and cross section

The scattering amplitude tensor for a scatterer with an arbitrary orientation with respect to the reference frame, described by the two-dimensional variable $\Omega = (\alpha, \beta)$, $0 < \alpha < 2\pi$, $0 < \beta < \pi/2$, with α and β defined in Fig. 5.4, can be obtained from the corresponding local-frame scattering amplitude tensor by means of a transformation of coordinates. In view of the application considered in this thesis, we are only interested in the vertical components of the fields incident on and scattered by branches and leaves. The reference-frame scattering amplitude tensor element which relates these fields is written as [61]

$$\begin{aligned} F^{b,l}(\hat{\mathbf{k}}_s, \hat{\mathbf{k}}_i) = \frac{1}{D(\hat{\mathbf{k}}_s, \hat{\mathbf{k}}_i)} \Big\{ & t_{vs}\big[f_{vv}^{b,l}(\hat{\mathbf{k}}_s, \hat{\mathbf{k}}_i) t_{vi} - f_{vh}^{b,l}(\hat{\mathbf{k}}_s, \hat{\mathbf{k}}_i) t_{hi} \big] \\ & - t_{hs}\big[f_{hv}^{b,l}(\hat{\mathbf{k}}_s, \hat{\mathbf{k}}_i) t_{vi} - f_{hh}^{b,l}(\hat{\mathbf{k}}_s, \hat{\mathbf{k}}_i) t_{hi} \big] \Big\}, \end{aligned} \tag{5.7}$$

where

$$D(\hat{\mathbf{k}}_s, \hat{\mathbf{k}}_i) = \sqrt{(t_{vs}^2 + t_{hs}^2)(t_{vi}^2 + t_{hi}^2)} \tag{5.8a}$$

$$t_{vs} = -\cos\beta \tag{5.8b}$$

$$t_{hs} = \sin\beta \sin(\alpha - \varphi_s) \tag{5.8c}$$

$$t_{vi} = -\cos\beta \tag{5.8d}$$

$$t_{hi} = \sin\beta \sin\alpha. \tag{5.8e}$$

Note that the subscript "vv" of the reference-frame scattering amplitude, which indicates vertical polarisation of the incident and scattered fields, is omitted for convenience.

The incidence and scattering angles in the local frame are related to φ_s, α and β

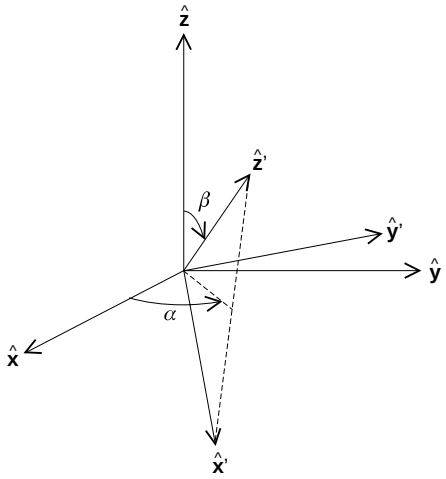

Fig. 5.4: Orientation of the local frame with respect to the reference frame.

by

$$\theta_i' = \frac{\pi}{2} - \arccos\{\sin\beta\cos\alpha\} \tag{5.9a}$$

$$\varphi_i' = \frac{\pi}{2}\big[1 - \operatorname{sgn}\{\cos\alpha\cos\beta\}\big] - \arctan\left\{\frac{\sin\alpha}{\cos\alpha\cos\beta}\right\} \tag{5.9b}$$

$$\theta_s' = \frac{\pi}{2} + \arccos\{\sin\beta\cos(\alpha - \varphi_s)\} \tag{5.9c}$$

$$\varphi_s' = \frac{\pi}{2}\big[1 - \operatorname{sgn}\{\cos(\alpha - \varphi_s)\cos\beta\}\big] - \arctan\left\{\frac{\sin(\alpha - \varphi_s)}{\cos(\alpha - \varphi_s)\cos\beta}\right\}, \tag{5.9d}$$

where the function $\operatorname{sgn}(\cdot)$ is defined as

$$\operatorname{sgn}(x) = \begin{cases} 1, & \text{if } x \geq 0, \\ -1, & \text{if } x < 0. \end{cases} \tag{5.10}$$

The probability density functions of the orientations of branches and leaves are denoted by $f_\Omega^b(\alpha, \beta)$ and $f_\Omega^l(\alpha, \beta)$, respectively. The statistics of α are assumed to be independent of those of β, so that

$$f_\Omega^{b,l}(\alpha, \beta) = f_\alpha^{b,l}(\alpha)\, f_\beta^{b,l}(\beta). \tag{5.11}$$

Also, the spatial distribution of the scatterers over the canopy volume is assumed to be truly random (with a uniform probability density), i.e. no account is taken

of a minimum distance between scatterers due to their sizes. The mean scattering amplitude of a single branch or leaf can then be written as

$$\mathrm{E}\{F^{b,l}(\hat{\mathbf{k}}_s, \hat{\mathbf{k}}_i)\} = \int_0^{2\pi} d\alpha \int_0^{\pi/2} d\beta \; F^{b,l}(\hat{\mathbf{k}}_s, \hat{\mathbf{k}}_i) \, f_\Omega^{b,l}(\alpha, \beta). \tag{5.12}$$

The equivalent scattering amplitude per unit volume of the canopy is defined as

$$F^{\mathrm{eq}}(\hat{\mathbf{k}}_s, \hat{\mathbf{k}}_i) = \sum_{b=b_1,b_2,\ldots,b_{N_b}} \rho_b \mathrm{E}\{F^b(\hat{\mathbf{k}}_s, \hat{\mathbf{k}}_i)\} + \rho_l \mathrm{E}\{F^l(\hat{\mathbf{k}}_s, \hat{\mathbf{k}}_i)\}. \tag{5.13}$$

In a similar way, the mean scattering cross section of a single branch or leaf is found as

$$4\pi \mathrm{E}\{|F^{b,l}(\hat{\mathbf{k}}_s, \hat{\mathbf{k}}_i)|^2\} = 4\pi \int_0^{2\pi} d\alpha \int_0^{\pi/2} d\beta \; |F^{b,l}(\hat{\mathbf{k}}_s, \hat{\mathbf{k}}_i)|^2 \, f_\Omega^{b,l}(\alpha, \beta), \tag{5.14}$$

and the equivalent scattering cross section per unit volume of the canopy is

$$\sigma^{\mathrm{eq}}(\hat{\mathbf{k}}_s, \hat{\mathbf{k}}_i) = 4\pi \sum_{b=b_1,b_2,\ldots,b_{N_b}} \rho_b \mathrm{E}\{|F^b(\hat{\mathbf{k}}_s, \hat{\mathbf{k}}_i)|^2\} + \rho_l \mathrm{E}\{|F^l(\hat{\mathbf{k}}_s, \hat{\mathbf{k}}_i)|^2\}. \tag{5.15}$$

Practical values of the number densities and the size, orientation and dielectric parameters of branches and leaves will be discussed in Section 5.4.1.

5.3 Scattered field

In general, the fields inside and scattered by a random medium are random functions of position, and can be divided into a mean or coherent component and a fluctuating component, which is called the incoherent or diffuse field. As will be shown in Sections 5.3.2 and 5.3.3, under certain reasonable assumptions both the coherent and the incoherent components of the tree-scattered field $E_s(\mathbf{r})$ can be expressed in terms of the mean field inside the canopy. A top view of the canopy volume is shown in Fig. 5.5.

5.3.1 Mean field inside the canopy

The field incident on the canopy is assumed to be a ray-optical field and can therefore be written as

$$E_i(\mathbf{r}) = A_i(\mathbf{r}) \; \exp\{-jkS_i(\mathbf{r})\}. \tag{5.16}$$

As the source of the incident field is located far away, the amplitude $A_i(\mathbf{r})$ is considered constant over the canopy volume. The eikonal of the incident field may be

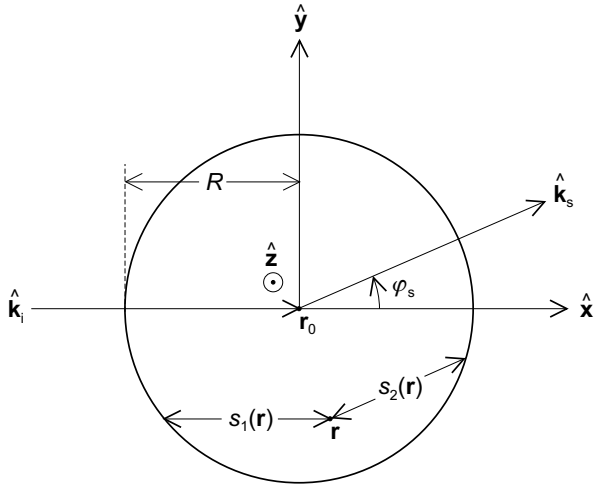

Fig. 5.5: Top view of the cylindrical canopy volume V.

written in terms of the phase at the canopy centre $\mathbf{r}_0$ and the displacement of $\mathbf{r}$ from $\mathbf{r}_0$, as

$$S_i(\mathbf{r}) = S_i(\mathbf{r}_0) + \hat{\mathbf{k}}_i \cdot (\mathbf{r} - \mathbf{r}_0) + \frac{1}{2}(\mathbf{r} - \mathbf{r}_0) \cdot \left[\frac{\hat{\mathbf{x}}_1 \hat{\mathbf{x}}_1}{r_1} + \frac{\hat{\mathbf{x}}_2 \hat{\mathbf{x}}_2}{r_2} \right] \cdot (\mathbf{r} - \mathbf{r}_0), \qquad (5.17)$$

where r_1 and r_2 are the principal radii of curvature of the incident wavefront, and $\hat{\mathbf{x}}_1$ and $\hat{\mathbf{x}}_2$ are unit vectors, each of which in combination with $\hat{\mathbf{k}}_i$ defines one of the principal planes of curvature. It is assumed that $\hat{\mathbf{x}}_1$ is oriented parallel to $\hat{\mathbf{z}}$, and $\hat{\mathbf{x}}_2$ is parallel to $\hat{\mathbf{y}}$. Now, the incident field in the canopy volume is

$$E_i(\mathbf{r}) = E_0 \, \exp\left\{ -jkx - \frac{1}{2} jk \left[\frac{z^2}{r_1} + \frac{y^2}{r_2} \right] \right\}, \quad \mathbf{r} \in V, \qquad (5.18)$$

where $E_0 = E_i(\mathbf{r}_0)$.

The coherent field $\mathrm{E}\{E^{\mathrm{in}}(\mathbf{r})\}$ inside the canopy can be shown [60] to satisfy the wave equation

$$\left(\nabla^2 + K^2\right) \mathrm{E}\{E^{\mathrm{in}}(\mathbf{r})\} = 0, \qquad (5.19)$$

in which

$$K = k + \frac{2\pi}{k} F^{\mathrm{eq}}(\hat{\mathbf{k}}_i, \hat{\mathbf{k}}_i) = K' - jK'' \qquad (5.20)$$

is the effective propagation constant. As $F^{\,\mathrm{eq}}(\hat{\mathbf{k}}_i, \hat{\mathbf{k}}_i)$ is in general a complex number, the attenuation constant K'' is non-zero and the coherent field attenuates as it propagates through the canopy. The specific attenuation in decibels per metre (dB/m) is given as

$$\alpha_c = 8.686\, K''. \tag{5.21}$$

For the case of a plane wave of the form

$$E_i(\mathbf{r}) = E_0 \exp\{-jk(\hat{\mathbf{k}}_i \cdot \mathbf{r})\} \tag{5.22}$$

incident on a slab containing random scatterers, the coherent field at a point $\mathbf{r}$ inside the slab can be shown to be [60]

$$\mathrm{E}\{E^{\mathrm{in}}(\mathbf{r})\} = E_i(\mathbf{r}) \exp\{-j(K-k)s_1(\mathbf{r})\}, \quad \mathbf{r} \in V, \tag{5.23}$$

where $s_1(\mathbf{r})$ is the length of the path through the slab to $\mathbf{r}$, along the incidence direction $\hat{\mathbf{k}}_i$. For a field of the more general form (5.16) incident on the canopy volume V it is assumed that the mean field inside the canopy can be described by the same equation (5.23), with $E_i(\mathbf{r})$ as in (5.16) and

$$s_1(\mathbf{r}) = x + \sqrt{R^2 - y^2}, \quad \mathbf{r} \in V, \tag{5.24}$$

which is equal to the length of the path to $\mathbf{r}$ through the cylindrical volume V (view Fig. 5.5).

5.3.2 Coherent scattered field

The coherent tree-scattered field can be found using Foldy-Twersky's integral equation for the coherent field in Twersky's multiple scattering theory [60]. This theory includes all multiple scattering involving chains of successive scattering going through different scatterers, but neglects the scattering paths which go through a scatterer more than once. According to Twersky's theory, for a uniform density of scatterers the coherent scattered field is given by

$$E_s^{\mathrm{coh}}(\mathbf{r}) = \mathrm{E}\{E_s(\mathbf{r})\} = \iiint_V U(\mathbf{r}, \mathbf{r}')\, \mathrm{E}\{E^{\mathrm{in}}(\mathbf{r}')\}\, dV', \tag{5.25}$$

where $U(\mathbf{r}, \mathbf{r}')$ is an operator which relates the mean scattered field at $\mathbf{r}$ due to a unit volume of the random medium located at $\mathbf{r}'$, to the field $\mathrm{E}\{E^{\mathrm{in}}(\mathbf{r}')\}$ incident on this volume. When $\mathbf{r}$ is in the far zone of the particles in the unit scattering volume at $\mathbf{r}'$, $U(\mathbf{r}, \mathbf{r}')$ can be approximated by

$$U(\mathbf{r}, \mathbf{r}') = 4\pi F^{\mathrm{eq}}(\hat{\mathbf{k}}_s, \hat{\mathbf{k}}_i)\, G_0(\mathbf{r}, \mathbf{r}'), \tag{5.26}$$

where

$$G_0(\mathbf{r},\mathbf{r}') = \frac{e^{-jk|\mathbf{r}-\mathbf{r}'|}}{4\pi\,|\mathbf{r}-\mathbf{r}'|} \tag{5.27}$$

is the free-space Green's function. For an observation point $\mathbf{r}$ located far away from the canopy, this function is well approximated by

$$\begin{aligned} G_0(\mathbf{r}_0 + s\hat{\mathbf{k}}_s, \mathbf{r}_0 + x'\hat{\mathbf{x}} + y'\hat{\mathbf{y}} + z'\hat{\mathbf{z}}) = {} & \frac{\exp\{-jk[s - x'\cos\varphi_s - y'\sin\varphi_s]\}}{4\pi s} \\ & \times \exp\left\{-jk\left[\frac{(x'\sin\varphi_s - y'\cos\varphi_s)^2 + z'^2}{2s}\right]\right\}, \end{aligned} \tag{5.28}$$

where s is the distance from the canopy centre to the observation point.

In order to simplify the computation of the coherent tree-scattered field, it is assumed that the canopy is high compared to the diameter of the first Fresnel zone at $\mathbf{r}_0$, so that the finite integral over z' in equation (5.25) may be replaced by an integration from $z' = -\infty$ to $z' = \infty$. Then, after substitution of (5.26), (5.23), (5.18) and (5.28) into (5.25) and performing the z'-integration, the coherent scattered field can be written as

$$E_s^{\mathrm{coh}}(\mathbf{r}) = E_0 S \sqrt{\frac{r_1}{s(r_1+s)}}\, e^{-jks}, \tag{5.29}$$

where

$$\begin{aligned} S = {} & \left[\frac{2\pi}{k}\right]^{\frac{1}{2}} e^{-j\pi/4}\, F^{\mathrm{eq}}(\hat{\mathbf{k}}_s, \hat{\mathbf{k}}_i) \iint\limits_{x'^2+y'^2<R^2} \exp\{-j(K-k)s_1(\mathbf{r}')\} \\ & \times \exp\left\{-jk\left[x'(1-\cos\varphi_s) - y'\sin\varphi_s \right.\right. \\ & \left.\left. + \frac{y'^2}{2r_2} + \frac{(x'\sin\varphi_s - y'\cos\varphi_s)^2}{2s}\right]\right\} dx'dy', \end{aligned} \tag{5.30}$$

is the scattering coefficient. The result (5.29) is similar in form to the general expression for the diffracted field used in the geometrical theory of diffraction (GTD) and its uniform extension (UTD). Physically, it describes the coherent scattered field in terms of a "coherently scattered ray" which interacts with the tree at the canopy centre $\mathbf{r}_0$.

The next step in the analysis is to find alternative, approximate expressions for the scattering coefficient (5.30) that require less computational effort to evaluate than

a numerical double integration. To this end, S is rewritten as

$$S = \left[\frac{2\pi}{k}\right]^{\frac{1}{2}} e^{-j\pi/4}\, F^{\mathrm{eq}}(\hat{\mathbf{k}}_s, \hat{\mathbf{k}}_i) \int_{-R}^{R} I_{y'}(x')dx', \tag{5.31}$$

in which $I_{y'}$ is given by

$$I_{y'}(x') = I^a_{y'} - I^b_{y'} = \int_{y'_a}^{\infty} \psi(y')e^{-jk\mu(y')}dy' - \int_{y'_b}^{\infty} \psi(y')e^{-jk\mu(y')}dy', \tag{5.32}$$

with integration endpoints $y'_a = -\sqrt{R^2 - x'^2}$ and $y'_b = \sqrt{R^2 - x'^2}$. In these integrals,

$$\psi(y') = \exp\{-j(K-k)s_1(\mathbf{r}')\} \tag{5.33}$$

is a complex "amplitude" function, and

$$\mu(y') = x'(1-\cos\varphi_s) - y'\sin\varphi_s + \frac{y'^2}{2r_2} + \frac{(x'\sin\varphi_s - y'\cos\varphi_s)^2}{2s} \tag{5.34}$$

is a smooth, real "phase" function with first and second derivatives

$$\begin{aligned} \mu'(y') &= -\sin\varphi_s + \frac{y'}{r_2} - \frac{(x'\sin\varphi_s - y'\cos\varphi_s)\cos\varphi_s}{s} \\ \mu''(y') &= \frac{1}{r_2} + \frac{\cos^2\varphi_s}{s}. \end{aligned} \tag{5.35}$$

According to the method of stationary phase, for large k the integrals $I^{a,b}_{y'}$ can be well approximated, in closed form, in terms of contributions from the neighbourhoods of the critical points, viz. the stationary point

$$y'_s = \frac{r_2\sin\varphi_s(s + x'\cos\varphi_s)}{r_2\cos^2\varphi_s + s}, \tag{5.36}$$

for which $\mu'(y') = 0$, and the integration endpoints $y'_{a,b}$ [63]. For some values of x', however, the stationary point may be near or even equal to one of the endpoints, and the contributions arising from the neighbourhoods of these points may not be treated separately. In the following, two different approaches are discussed to circumvent this problem.

First consider the asymptotic expansion obtained by Lewis in [64]. When applied to the integrals $I^{a,b}_{y'}$, this expansion is valid uniformly for y'_s in the neighbourhood

of $y'_{a,b}$, provided that $\psi(y')$ and $\mu(y')$ are smooth functions on the interval $y'_a - \epsilon \leq y' \leq y'_b + \epsilon$, where $\epsilon > 0$. This condition is not satisfied by the amplitude function $\psi(y')$, which is not differentiable at $y' = y'_{a,b}$. If, on the other hand, $\psi(y')$ is approximated as

$$\psi(y') \simeq \exp\big\{-j(K-k)\big[x'+R\big]\big\}, \tag{5.37}$$

one obtains

$$\begin{aligned} I_{y'}^{a,b} &\simeq \exp\big\{-j(K-k)\big[x'+R\big]\big\} e^{-jk\mu(y'_{a,b})} \\ &\times \left\{ \left[\frac{2}{k\big|\mu''(y'_s)\big|} \right]^{\frac{1}{2}} g_-\left(\operatorname{sgn}(y'_{a,b}-y'_s)\sqrt{k\big|\mu(y'_{a,b})-\mu(y'_s)\big|} \right) - \frac{j}{k\mu'(y'_{a,b})} \right\}, \end{aligned} \tag{5.38}$$

with

$$g_-(x) = f_-(x) - \frac{1}{2jx} \tag{5.39}$$

$$f_-(x) = e^{jx^2} \int_x^\infty e^{-jt^2} dt. \tag{5.40}$$

The function $f_-(\cdot)$ is closely related to the modified Fresnel integral, and can be approximated by [64, 65]

$$\begin{aligned} f_-(x) &= \sqrt{\pi}\left[\frac{1}{2\sqrt{\pi x^2 + x + 1}} + 0.022x\exp(-0.29x^2) \right] \\ &\qquad \times \exp\left\{ -j\arctan(x^2 + 1.5x + 1) \right\}, \quad x \geq 0 \end{aligned} \tag{5.41a}$$

$$f_-(-x) = \sqrt{\pi}\exp\big\{j(x^2 - \pi/4)\big\} - f_-(x). \tag{5.41b}$$

The amplitude and phase errors of the estimates of $f_-(\cdot)$ obtained with this formula are contained within 3.4 and 2 percent, respectively. For values of y'_s that are very close to $y'_{a,b}$, $I_{y'}^{a,b}$ reduces to

$$I_{y'}^{a,b} \to \left[\frac{\pi}{2k\big|\mu''(y'_s)\big|} \right]^{\frac{1}{2}} \exp\big\{-j(K-k)\big[x'+R\big]\big\} e^{-jk\mu(y'_s) - j\pi/4}, \quad y'_s \to y'_{a,b}. \tag{5.42}$$

The scattering coefficient S is computed by performing the single integration over x' in (5.31) numerically, using a rectangular rule.

A second approach to arriving at an asymptotic approximation of the double integral in expression (5.30) is to neglect the contributions from the endpoints $y'_{a,b}$, and restrict the analysis to those scattering angles φ_s for which stationary points exist in the canopy volume. This is the case if φ_s is small (forward scattering), such that the observation point is in the shadow area of the tree. For small values of φ_s, the phase function of (5.34) can be approximated as

$$\mu(y') \simeq x'(1-\cos\varphi_s) - y'\sin\varphi_s + \frac{y'^2}{2r_2} + \frac{y'^2\cos^2\varphi_s}{2s} \tag{5.43}$$

and the stationary point becomes

$$y'_s \simeq \frac{r_2 s\sin\varphi_s}{r_2\cos^2\varphi_s + s}. \tag{5.44}$$

If $|y'_s| < \sqrt{R^2 - x'^2}$, the integral $I_{y'}$ is approximated by the contribution arising from the vicinity of y'_s, which yields

$$I_{y'} \simeq \left[\frac{2\pi}{k}\right]^{\frac{1}{2}} e^{-j\pi/4}\sqrt{\frac{r_2 s}{r_2\cos^2\varphi_s + s}}\; A\;\exp\{-jx'[K - k\cos\varphi_s]\}, \tag{5.45}$$

with

$$A = \exp\{-j(K-k)\sqrt{R^2 - y'^2_s} + \frac{1}{2}jky'_s\sin\varphi_s\}. \tag{5.46}$$

If $|y'_s| \geq \sqrt{R^2 - x'^2}$, $I_{y'}$ is assumed to be zero. The integral over x' in equation (5.31) can now be evaluated in closed form, and the scattering coefficient is obtained as

$$S = -\frac{4\pi j}{k}\; F^{\text{eq}}(\hat{\mathbf{k}}_s, \hat{\mathbf{k}}_i)\sqrt{\frac{r_2 s}{r_2\cos^2\varphi_s + s}}\; A\;\frac{\sin[(K - k\cos\varphi_s)x'_s]}{K - k\cos\varphi_s}, \tag{5.47}$$

in which $x'_s = \sqrt{R^2 - y'^2_s}$. Note that, in general, the argument of the sine function in this expression has a complex value.

5.3.3 Incoherent scattered field

The incoherent (or diffuse) scattered field due to the tree canopy can be obtained from Twersky's integral equations for the total field intensity in Twersky's multiple scattering theory [60]. According to these equations, for a uniform density of

scatterers, the diffuse field intensity is given by

$$\begin{aligned} \mathrm{E}\{|E_s^{\mathrm{dif}}(\mathbf{r})|^2\} &= \mathrm{E}\{|E_s(\mathbf{r})|^2\} - |E_s^{\mathrm{coh}}(\mathbf{r})|^2 \\ &= \iiint_V |V(\mathbf{r},\mathbf{r}')|^2 \,\mathrm{E}\{|E^{\mathrm{in}}(\mathbf{r}')|^2\} dV' \end{aligned} \tag{5.48}$$

$$V(\mathbf{r},\mathbf{r}') = U(\mathbf{r},\mathbf{r}') + \iiint_V U(\mathbf{r},\mathbf{r}'')V(\mathbf{r}'',\mathbf{r}')dV''. \tag{5.49}$$

As in Section 5.3.2, $U(\mathbf{r},\mathbf{r}')$ is an operator which relates the field at $\mathbf{r}$ scattered from a unit scattering volume at $\mathbf{r}'$ to the field incident on the volume. The operator $V(\mathbf{r},\mathbf{r}')$, which represents the total radiation from a unit scattering volume at $\mathbf{r}'$ to $\mathbf{r}$ through multiple scattering, is approximated as

$$V(\mathbf{r},\mathbf{r}') = 4\pi F^{\mathrm{eq}}(\hat{\mathbf{k}}_s,\hat{\mathbf{k}}_i)\; G_0(\mathbf{r},\mathbf{r}') \exp\{-j(K-k)s_2(\mathbf{r}')\}, \tag{5.50}$$

where $s_2(\mathbf{r}')$ is the path length from $\mathbf{r}'$ to the observation point through the canopy along the direction of scattering $\hat{\mathbf{k}}_s$ (see Fig. 5.5), given by

$$s_2(\mathbf{r}) = -x\cos\varphi_s - y\sin\varphi_s + \sqrt{R^2 - x^2\sin^2\varphi_s - y^2\cos^2\varphi_s}, \quad \mathbf{r}\in V. \tag{5.51}$$

The operator $V(\mathbf{r},\mathbf{r}')$ is similar in form to the single-scattering operator $U(\mathbf{r},\mathbf{r}')$ given by (5.26), except that the propagation constant in the canopy is K rather than k, to account for the additional loss due to multiple scattering.

In general, under the assumption that the scatterers in a random medium have a small scattering albedo, the total field intensity $\mathrm{E}\{|E^{\mathrm{in}}(\mathbf{r})|^2\}$ in the medium can be approximated by the coherent intensity $|\mathrm{E}\{E^{\mathrm{in}}(\mathbf{r})\}|^2$. This approximation, and the substitution of (5.18), (5.23), (5.28) and (5.50) into (5.48), lead to the following expression for the diffuse scattered field intensity:

$$\mathrm{E}\{|E_s^{\mathrm{dif}}(\mathbf{r})|^2\} = \frac{|E_0|^2}{4\pi s^2}\sigma^{\mathrm{eq}}(\hat{\mathbf{k}}_s,\hat{\mathbf{k}}_i)I(\varphi_s), \tag{5.52}$$

in which $\sigma^{\mathrm{eq}}(\hat{\mathbf{k}}_s,\hat{\mathbf{k}}_i)$, as previously, is the equivalent scattering cross section of a unit volume within the tree canopy, and

$$I(\varphi_s) = \iiint_V \exp\{-2K''[s_1(\mathbf{r}') + s_2(\mathbf{r}')]\}dV'. \tag{5.53}$$

The bistatic scattering cross section of the entire canopy is given by

$$\sigma(\hat{\mathbf{k}}_s,\hat{\mathbf{k}}_i) = \sigma^{\mathrm{eq}}(\hat{\mathbf{k}}_s,\hat{\mathbf{k}}_i)I(\varphi_s). \tag{5.54}$$

The integral $I(\varphi_s)$ describes to what degree each elemental canopy volume dV' contributes to the total incoherent scattered field, and is closely related to the illumination integral in [66]. When normalised with respect to the total canopy volume $\pi H R^2$, it is a function of the scattering angle φ_s and the product $K''R$. For $K''R < 1$, $I(\varphi_s)$ is approximated by the empirical formula

$$\begin{aligned} I(\varphi_s) = \pi H R^2 \big\{1 + \big[K''R\big]^2 \big(1 - \cos\varphi_s\big)\big\} \\ \times \exp\big\{-3.62K''R + 0.58\big[K''R\big]^2\big\} \end{aligned} \tag{5.55}$$

with an accuracy better than 0.7 dB for all φ_s.

5.4 Numerical results

This section presents numerical results generated using the expressions of the previous section, and attempts to assess the loss in accuracy caused by some of the approximations that were made in the derivations of these expressions. Branch and leaf parameters such as size and orientation statistics and dielectric properties are important inputs to the models, and will be discussed in Section 5.4.1.

5.4.1 Branch and leaf parameters

Number densities, size and orientation statistics of branches and leaves were analysed in detail for an oak tree in Boxtel, The Netherlands (view Fig. 5.6), which is considered to be a typical example of the trees commonly found in urban environments. The same tree was also used for a number of scattering experiments, which are reported in Section 5.5. The branches were categorised into $N_b = 5$ groups according to their radii, and for each group an average branch length and number density were computed. Leaf thickness and radius were determined for a single, representative oak leaf. The size parameter values that were thus obtained are listed in Table 5.1. On average, these values are larger than those found by McDonald *et al.* [67] and Karam *et al.* [68] for a walnut orchard. However, the trees examined by these authors were only six years old and therefore probably less mature than the tree analysed in the present study and most urban trees.

Neither branches nor leaves were found to exhibit a preferred azimuthal orientation, and the distribution of α is therefore chosen to be uniform on $(0, 2\pi)$. The statistics of the elevational orientation β of branches and leaves are assumed to be described by the distribution

$$f_\beta^{b,l}(\beta) = \begin{cases} \sin\beta/(\cos\beta_1 - \cos\beta_2), & \text{if } \beta_1 < \beta < \beta_2, \\ 0, & \text{otherwise.} \end{cases} \tag{5.56}$$

(a) (b)

Fig. 5.6: The Boxtel oak tree (a) in full leaf (summer) and (b) defoliated (winter).

The orientation of the larger branches (categories 1 and 2) was observed to be predominantly vertical, and therefore these branches are assigned the values $\beta_1 = 0$ and $\beta_2 = \pi/4$. The smaller branches (categories 3, 4 and 5) and the leaves are characterised by $\beta_1 = 0$ and $\beta_2 = \pi/2$, which implies that they have no preferred orientation at all (spherical distribution).

As time did not permit measurements of the effective dielectric permittivity of branches and leaves, suitable values were obtained from the literature, as described below. The dielectric properties of branch and leaf material are well known to be strongly influenced by the gravimetric moisture content M_g, defined as the ratio between the mass of the moisture contained in the material and the total mass of

Table 5.1: Size and dielectric parameters of branches and leaves.

Scatterer type	Radius (cm)	Length/ thickness (cm)	Relative permittivity	Number density (m^{-3})
Branch (1)	11.4	131	$28 - j7$	0.013
Branch (2)	6.0	99	$28 - j7$	0.073
Branch (3)	2.8	82	$28 - j7$	0.41
Branch (4)	0.7	54	$28 - j7$	5.1
Branch (5)	0.2	12	$28 - j7$	56
Leaf	3.7	0.02	$31 - j8$	420

the moist material. As the moisture content of branches shows significant diurnal and seasonal variations, their dielectric properties are also strongly time-dependent. From the results presented in [67], the average day-time dielectric permittivity of branches at 1.2 GHz is found to be $\epsilon_b = 28 - j7$. From a comparison with the dielectric properties of wood, tabulated in [62] as a function of various parameters, it is concluded that ϵ_b remains approximately constant in the high UHF frequency band used for mobile communications, and is hardly dependent on temperature above freezing point.

A semi-empirical formula for the complex permittivity of leaves in terms of M_g and the complex permittivity $\epsilon_{\rm sw}$ of saline water, valid in the frequency range from 1 to 100 GHz and for a salinity of about 1%, was proposed in [69] and is written as

$$\epsilon_l = 0.689\ (M_g - 0.24)\ \epsilon_{\rm sw} + 4.35 - 3.84 M_g. \tag{5.57}$$

For a walnut tree, the moisture content M_g of the leaves was shown in [67] to be time-invariant and have a value of approximately 80%. The dielectric properties of saline water are strongly dependent on frequency, and can be evaluated using [70]. For a frequency of 2 GHz and a salinity of 1%, $\epsilon_{\rm sw}$ takes a value of $77 - j22$, and the leaf permittivity becomes $\epsilon_l = 31 - j8$. Similar to branches, above freezing point the temperature-dependence of ϵ_l is negligible. The dielectric parameter values discussed above are also listed in Table 5.1.

5.4.2 Attenuation coefficients

Theoretical values of the attenuation coefficient α_c due to the different canopy constituents, computed with the aid of (5.13), (5.20) and (5.21), are shown in Table 5.2. Examination of this table shows that most of the attenuation is due to the smaller branches (size category 4) and the leaves. The total attenuation coefficient for the tree in leaf is 1.10 dB/m; for the defoliated tree this value is 0.80 dB/m. These values are comparable to, although somewhat lower than the experimental values published in [56] (1.3 and 1.1 dB/m, respectively), which were obtained in the shadow zone of a single Pecan tree at 1.6 GHz. The difference between these values may be related to differences in branch and leaf parameters.

5.4.3 Scattering cross sections of branches and leaves

Fig. 5.7 shows the mean scattering cross sections for single branches and leaves, computed using equation (5.14) with size, orientation and dielectric parameters taken from Table 5.1. It can be seen that the scattering from the larger branches is concentrated in the forward direction, whereas the scattering from the smallest branches (size category 5) and the leaves is almost isotropic. Fig. 5.7 also shows the equivalent scattering cross sections per unit volume of canopy, $\sigma^{\rm eq}(\hat{\mathbf{k}}_s, \hat{\mathbf{k}}_i)$, for the tree in

Table 5.2: Attenuation coefficients associated with branches and leaves at 1.9 GHz.

Scatterer type	Specific attenuation coefficient (dB/m)
Branch (1)	0.04
Branch (2)	0.08
Branch (3)	0.17
Branch (4)	0.44
Branch (5)	0.07
Leaf	0.30
Total	1.10

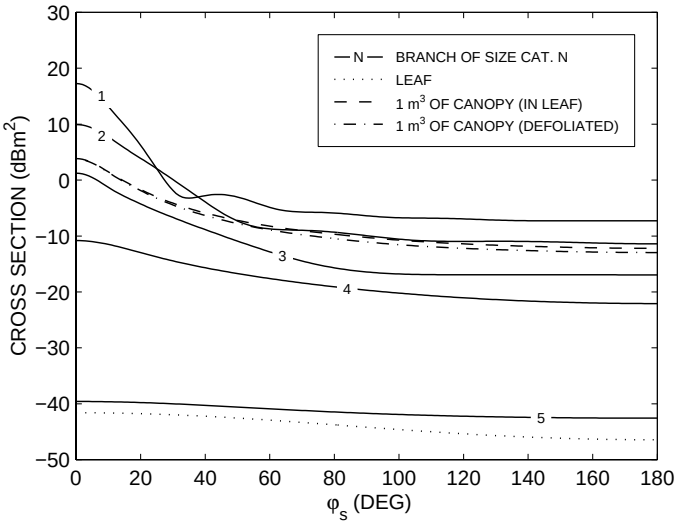

Fig. 5.7: Mean scattering cross sections of branches and leaves at 1.9 GHz.

full leaf, computed using equation (5.15) and the number densities of Table 5.1, and for the defoliated tree, computed by setting $\rho_l = 0$. As can be observed in Fig. 5.7, $\sigma^{\text{eq}}(\hat{\mathbf{k}}_s, \hat{\mathbf{k}}_i)$ is almost identical for these two cases.

5.4.4 Coherent scattered field

This section compares the coherent scattering patterns obtained by evaluating:

1. the expression (5.30) using a numerical double integration with an estimated accuracy of 1 percent (reference method);

2. the integral $I_{y'}$ using the asymptotic expansion (5.38) and performing the single integration in (5.31) numerically, using a rectangular rule with fixed step size $\Delta x'$;

3. the closed-form expression (5.47).

All three methods require the computation of the equivalent scattering amplitude $F^{\text{eq}}(\hat{\mathbf{k}}_s, \hat{\mathbf{k}}_i)$. This is a very time-consuming task, but has to be performed only once; the computed values are then stored and can be read every time S is evaluated. The branch and leaf parameters used to produce the results of this section were taken from Table 5.1. The tree was assumed to be in full leaf.

First of all, in order to investigate the influence of the step size $\Delta x'$ on the accuracy of the numerical integration in method (2), the scattering coefficient S was evaluated for a range of step sizes and for different canopy radii R. An adaptive step size integration with an estimated accuracy of 1 percent was also performed for comparison. Normalised scattering patterns obtained in this way are shown in Fig. 5.8 for $R = 1$ and 5 m. The numerical integration accuracy tends to be better in the forward direction. For $R = 1$ m, a step size of 0.03λ is sufficient to guarantee an error smaller than 0.7 dB relative to the "adaptive step size" pattern, over the entire interval $0 < \varphi_s < 180^{\text{o}}$; for $R = 5$ m, the error is smaller than 0.4 dB for this step size. For a step size of 0.01λ, these maximum errors become 0.5 and 0.2 dB, respectively. In comparing the curves for $R = 1$ m and $R = 5$ m, it is further seen that the main lobe of the scattering pattern – responsible for the attenuation of the total field in the forward direction – is considerably wider for the larger canopy. This is not a surprising result as the larger canopy can be expected to have a larger "shadow area" behind it. In this region, the coherent scattered field is nearly equal to the incident field but approximately 180 degrees out of phase.

Next, the effects are considered of the approximations made in the derivation of the expressions for the coherent scattered field. In Fig. 5.9, the scattering patterns obtained using the approximate methods (2) and (3) are compared with the pattern

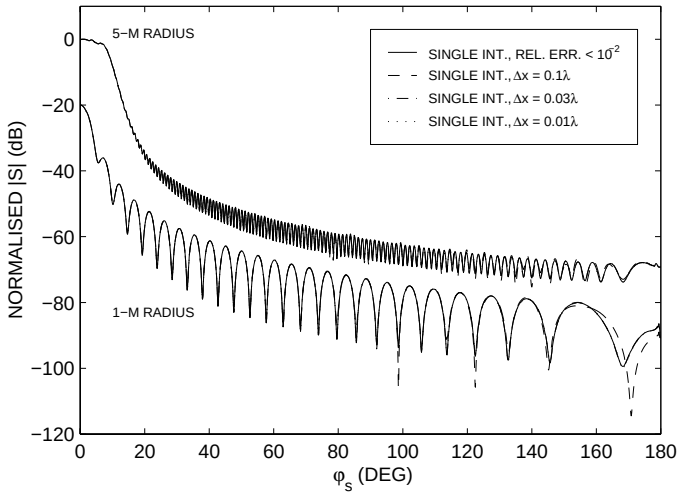

Fig. 5.8: Normalised magnitudes of the scattering coefficient S, for $R = 1$ m and $R = 5$ m. $r_2 = s = 50$ m, $f = 1.9$ GHz. Lower curves have an offset of -20 dB for clarity.

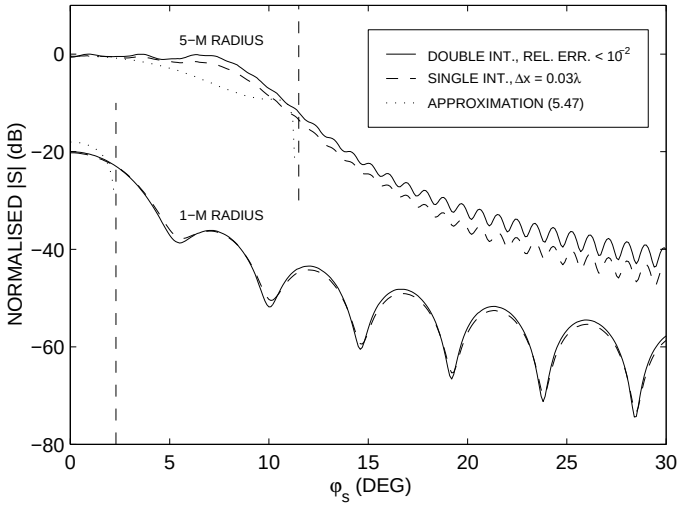

Fig. 5.9: Normalised magnitudes of the scattering coefficient S, for $R = 1$ m and $R = 5$ m. $r_2 = s = 50$ m, $f = 1.9$ GHz. Lower curves have an offset of -20 dB for clarity. Dashed vertical lines indicate GO shadow boundaries.

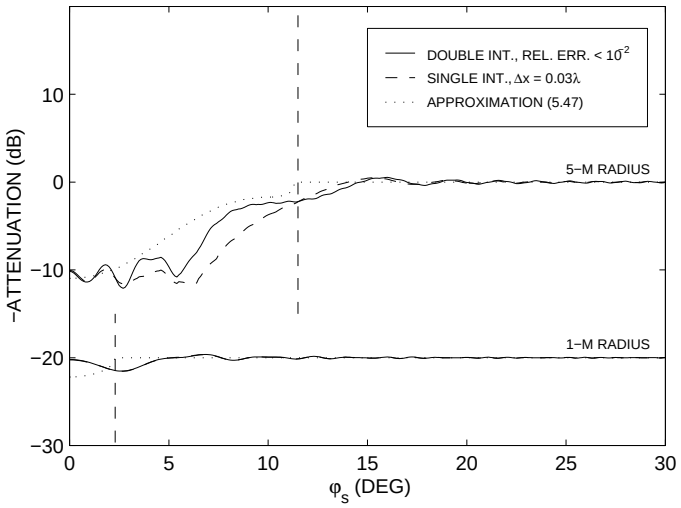

Fig. 5.10: Excess attenuation due to "tree shadowing", for $R = 1$ m and $R = 5$ m. $r_1 = r_2 = s = 50$ m, $f = 1.9$ GHz. Lower curves have an offset of -20 dB for clarity. Dashed vertical lines indicate GO shadow boundaries.

obtained using the reference method (1). All patterns in this figure are normalised with respect to the magnitude of the reference pattern for $\varphi_s = 0^o$. In addition, Fig. 5.10 shows the excess attenuation or "shadowing loss" – due to destructive interference with the coherent tree-scattered field – of a field originating from a point source at 50 m from the canopy centre. Again, the curves in this figure were computed using the three different methods mentioned above. In both Figs. 5.9 and 5.10, the boundary of the geometric-optical (GO) shadow region behind the canopy is indicated by dashed vertical lines. It is further noted that no comparisons are made for $\varphi_s > 30^o$ because of the excessive computational load of the double numerical integration for these angles.

From Fig. 5.9 it is observed that the approximations made in method (2) result in a fairly small disagreement with the reference method (1), especially in the GO shadow region. For $R = 5$ m the overall difference is considerably larger than for $R = 1$ m. This can be explained by the fact that the error made in the approximation of the true path length $s_1(\mathbf{r}')$ by $x' + R$ in (5.37) is proportional to R. Method (3) is seen to provide a relatively poor approximation of the reference scattering pattern. Also, as this method is only valid if stationary points exist in the canopy volume, it does not reproduce the lobes outside the shadow area. However, from Fig. 5.10 it is observed that, as far as the attenuation of the field behind the tree is concerned, both methods (2) and (3) provide a coarse but reasonable approximation.

5.4.5 Incoherent scattered field

To provide insight into the accuracy of the empirical formula (5.55), the integral $I(\varphi_s)$ in (5.53) was evaluated numerically with an estimated relative accuracy of 1 percent, for $R = 1$ and 5 m and $H = 8$ m. Fig. 5.11 compares the values of $\sigma(\hat{\mathbf{k}}_s, \hat{\mathbf{k}}_i)$ obtained in this way with values generated using (5.55). The equivalent scattering cross section per unit volume of the canopy, $\sigma^{\text{eq}}(\hat{\mathbf{k}}_s, \hat{\mathbf{k}}_i)$, was computed once and then stored for use in the computation of $\sigma(\hat{\mathbf{k}}_s, \hat{\mathbf{k}}_i)$. From Fig. 5.11 it is seen that the approximation (5.55) results in a maximum error smaller of 0.3 dB for a canopy radius of 5 m. For a radius of 1 m, the maximum error is smaller than 0.2 dB.

Fig. 5.12 compares the coherent and incoherent scattered fields due to an incident field radiated by a point source at 50 m from the canopy centre, for $R = 1$ and 5 m. The coherent field is computed by using the asymptotic expansion (5.38) and performing the single integration in (5.31) numerically, using a rectangular rule with step size $\Delta x' = 0.03\lambda$. The incoherent scattered field is computed using expression (5.55). All powers in this figure are relative to the power of the wave incident on the canopy centre. For both radii considered, the coherent scattered field is dominant over the incoherent scattered field in a small region that is approximately identical to the GO shadow region of the canopy. Outside this region, the incoherent scattered field quickly becomes much stronger than the coherent scattered field.

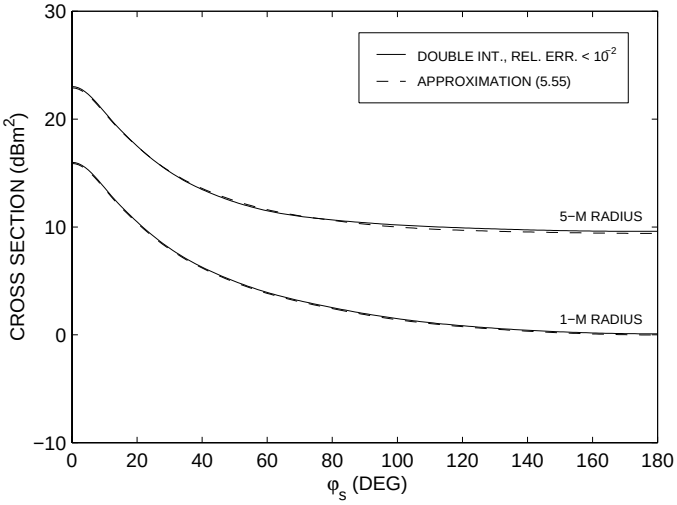

Fig. 5.11: Theoretical scattering cross sections of the tree in leaf, for $R = 1$ m and $R = 5$ m. $H = 8$ m, $f = 1.9$ GHz.

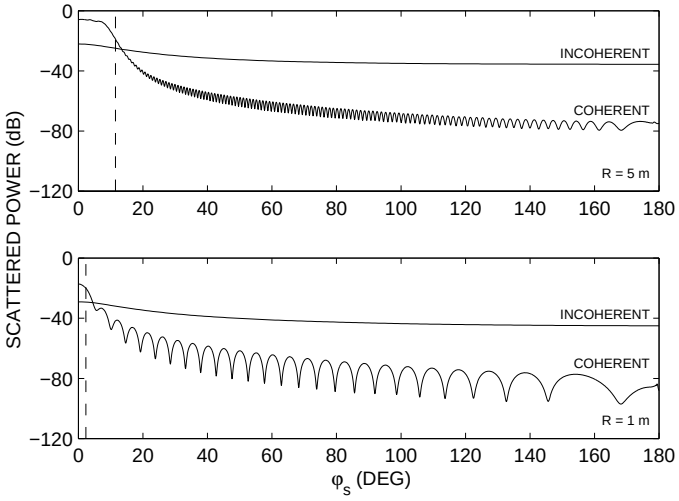

Fig. 5.12: Coherent and incoherent scattered fields due a point source, for $R = 1$ m and $R = 5$ m. $H = 8$ m, $r_1 = r_2 = s = 50$ m, $f = 1.9$ GHz. Dashed vertical lines indicate GO shadow boundaries.

5.5 Experimental results

This section describes the results of measurements of the field scattered by a single deciduous tree at 1.9 GHz. Where possible, a comparison is made with theoretical results. As with the building transmission measurements described in Chapter 4, one of the major concerns with this kind of measurement is formed by the disturbing effects of other multipath contributions entering the receiving antenna, of which the direct wave is the most important in the present case. To reduce the effects of scattering from other objects, a tree was selected that stands in the middle of a large, otherwise empty farmer's field. This tree was described in detail in Section 5.4.1, and is shown in Fig. 5.6. To distinguish the scattered field contribution from the direct wave, the TU/e wideband channel sounder – previously described in Section 2.2 – was employed. With this equipment multipath waves can be separated on the basis of their propagation delay times.

All measurements described in this section were conducted twice: the first time in August and September, 1999, when the tree was in full leaf, and the second time in January, 2000, when the tree was bare. On all measurement days there was no rain and only a light wind, i.e. leaves were slightly moving, but the branches were still.

5.5.1 Measurement equipment and procedure

During the experiment, the tree was uniformly illuminated using a 7.1-dBi vertically polarised double-ridged pyramidal horn with an azimuthal 3-dB beamwidth of 53 °. The antenna was located at 7 m above ground level, 50 m away from the centre of the canopy, as illustrated in Fig. 5.13. This configuration was also discussed in Section 3.3.2 of this thesis. A rotatable 2-dBi sleeve monopole antenna over a circular ground plane, located on the roof of a measurement vehicle (2.4 m above ground level), was used for reception.

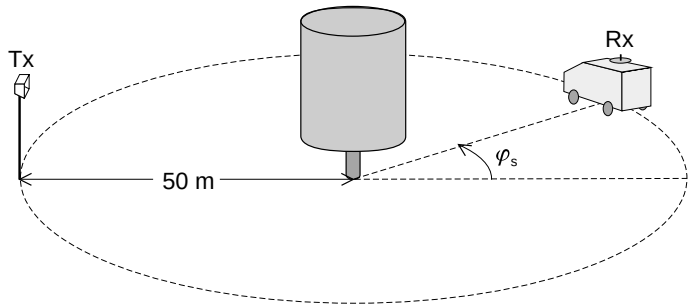

Fig. 5.13: Illustration of the measurement configuration.

Two types of measurements were conducted: (1) at a fixed vehicle location, with the antenna rotating along a horizontal circle with a radius of 30 cm, and (2) along a straight trajectory with the receiving antenna in a fixed position with respect to the vehicle. While the first type of measurement was used to determine the local average of the scattered power at a number of specified locations, the second type was useful to obtain information about the global behaviour of the scattered field.

In the experiments of the second type, impulse response data were recorded every 0.1 s while the vehicle was moving at constant speed along a trajectory running radially outward from the centre of the tree. As an example, Fig. 5.14 shows a measured set of power delay profiles for the trajectory corresponding with $\varphi_s = 135^o$. In this figure, the direct wave can easily be identified by its hyperbolic shape, and because it has minimum delay along the entire trajectory. The solid line represents the theoretical delay associated with the tree-scattered field, and is seen to be in very good agreement with the measured delay of the scattered contribution. The absolute scattered field strength, required to determine the tree's scattering cross section $\sigma(\hat{\mathbf{k}}_s, \hat{\mathbf{k}}_i)$, can be obtained in a way similar to that described in Section 4.4.1 for the field due to building transmission. The weak contribution arriving 0.16 μs after the direct wave for all receiver positions is the result of cable reflections (view Section 3.3.2).

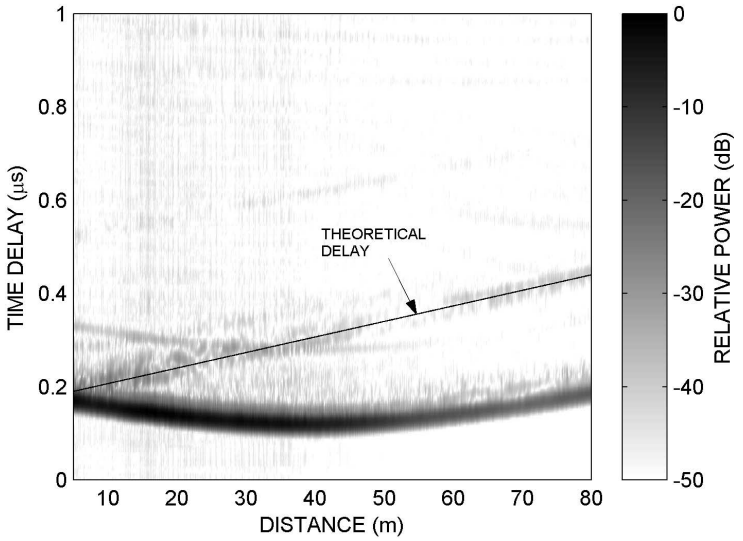

Fig. 5.14: Measured power delay profiles along the trajectory $\varphi_s = 135^{\text{o}}$.

In some part of the area, especially near and behind the tree, the delay time difference between the direct and the scattered field contributions becomes smaller than the resolution of the channel sounder (20 ns), and the scattered field can no longer be distinguished from the direct field. Of course, at these locations it is still possible to measure the total field, i.e. the sum of the direct and the scattered field.

5.5.2 Attenuation

Fig. 5.15 shows the received field strength, relative to the free-space level, along a straight trajectory in the shadow area behind the tree ($\varphi_s = 180^{\text{o}}$). Results of repeated measurements along the same trajectory are also shown. The field strength is seen to show strong, large-scale spatial variations, which are quite different for the "in leaf" and the defoliated case, but roughly time-invariant between successive measurements. The absence of large small-scale spatial fluctuations indicates that the field behind the tree is predominantly coherent. A possible explanation for the irregular large-scale fading patterns in Fig. 5.15 is the interference of the wave propagating through the canopy with a ground-reflected wave. For receiver locations close to the tree the ground-reflected wave propagates *under* the canopy, while at larger distances it is attenuated and phase-shifted by the canopy in the same way as the "direct" wave. The disturbing effect of the ground reflection makes it impossible to verify the theoretical values of the attenuation coefficient α_c that were found in

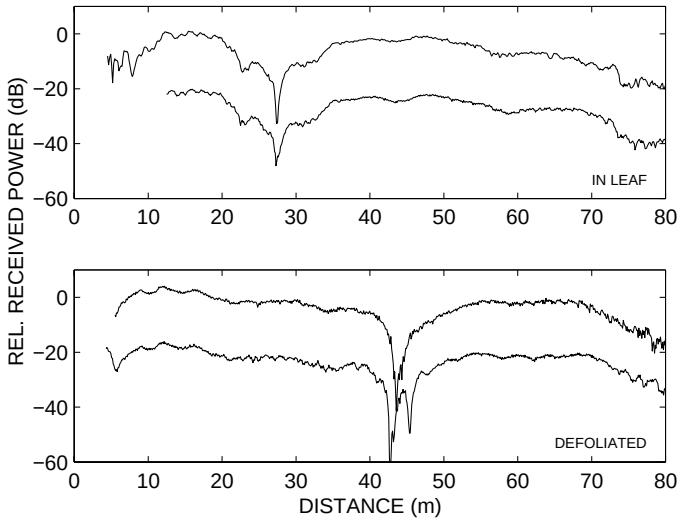

Fig. 5.15: Measured field strength, relative to the free-space level, behind the tree in leaf (top) and the defoliated tree (bottom), versus distance from the centre of the tree ($\varphi_s = 0^o$). Lower curves have an offset of -20 dB for clarity.

Section 5.4.2.

5.5.3 Scattering cross section

The method described in Section 5.5.1 was used to measure the scattered field along a trajectory corresponding with $\varphi_s = 135^o$. As in Section 5.5.2, the reproducibility of the resulting data was verified by repeating the measurement immediately afterwards. Fig. 5.16 shows the scattering cross section $\sigma(\hat{\mathbf{k}}_s, \hat{\mathbf{k}}_i)$, computed from the measured scattered field for every receiver position, versus the distance from the centre of the tree. The theoretical value of $\sigma(\hat{\mathbf{k}}_s, \hat{\mathbf{k}}_i)$ for $\varphi_s = 135^o$, computed with the aid of expression (5.55), is shown for comparison. For this computation the radius and height of the canopy were chosen equal to 5 m and 8 m, respectively.

Although the measured scattering cross section in Fig. 5.16 does show some large-scale spatial fluctuations – indicating disturbance caused by a ground-reflected wave – its local average value remains approximately constant along the entire trajectory and is very well predicted by the theory. Furthermore, it can be seen that the measurement results for the defoliated case were well reproducible, whereas they appear to have a random, time-varying nature for the tree in full leaf. This shows that small movements of leaves can have a significant influence on the instantaneous tree-scattered field.

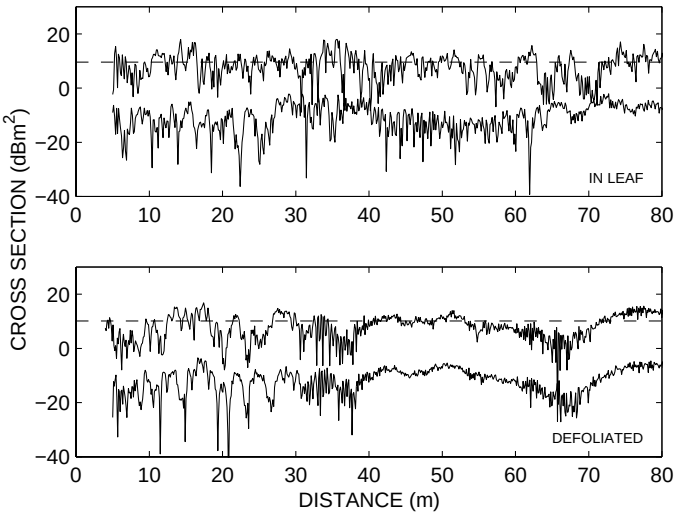

Fig. 5.16: Measured scattering cross section of the tree in leaf (top) and the defoliated tree (bottom), versus distance from the centre of the tree ($\varphi_s = 135^o$). Dashed lines represent theoretical values. Lower curves have an offset of -20 dB for clarity.

For the accurate measurement of the scattering cross section as a function of the scattering angle, the mobile receiver was moved to several locations – 10 degrees apart – on the perimeter of a 50-m circle around the canopy centre (view Fig. 5.13). At each location the receiving antenna was rotated along a 30-cm horizontal circle in order to record the local variations of the scattered field. Results of these measurements are given in Fig. 5.17, which shows the average measured scattering cross section, and the upper and lower 90 percent percentiles, versus the scattering angle φ_s. For $\varphi_s < 40^o$, the scattered field contribution could no longer be separated from the direct field. Large spreads in the measured cross section are observed over the entire range of φ_s, especially for the tree in leaf. Fig. 5.17 also shows the theoretical dependence of $\sigma(\hat{\mathbf{k}}_s, \hat{\mathbf{k}}_i)$ on φ_s. Theoretical and average measured values shown a reasonable to good agreement.

Contrary to what might be expected, the theory predicts a larger scattering cross section for the bare tree. Physically, this is because $\sigma^{\,\mathrm{eq}}(\hat{\mathbf{k}}_s, \hat{\mathbf{k}}_i)$, the equivalent scattering cross section per unit volume of the canopy, is strongly dominated by the branches. Due to the absence of leaves, the incident wave penetrates deeper into the canopy, so that more branches can contribute to the scattered field. The resulting difference in cross section is however small, and cannot be confirmed by the experimental results presented in this section.

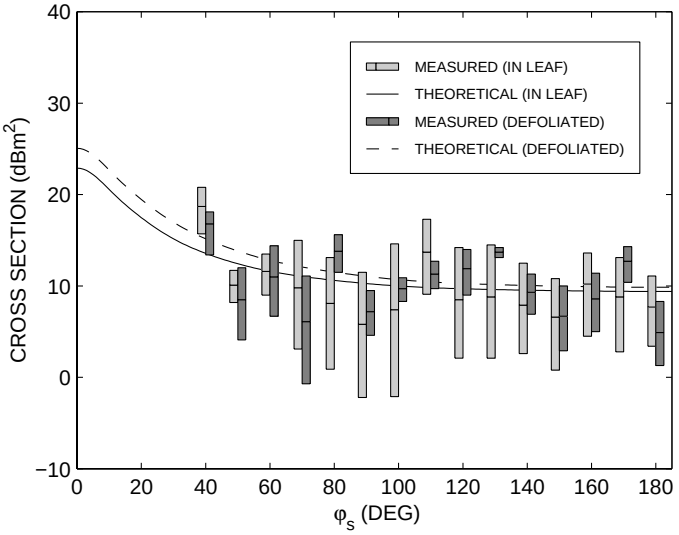

Fig. 5.17: Measured and theoretical scattering cross section versus the scattering angle. Vertical bars denote average scattered power and upper and lower 90 percent percentiles.

5.6 Conclusions

In this chapter, a quasi-two-dimensional model has been presented for the scattering of radiowaves from a single deciduous tree. In addition to coherent scattering, of which the attenuation of the field in the geometric-optical shadow area behind the tree is the most obvious manifestation, the effects of the incoherent scattered field have also been considered. Incoherent scattering is predominant over coherent scattering outside the tree's shadow area, and is a mechanism through which a part of the power of an incident field is dispersed in all directions. This can, for example, be an important phenomenon in radio propagation around street corners.

Approximate expressions for the coherent and incoherent tree-scattered fields, suitable to be used in any ray-based propagation model, were derived using Twersky's multiple scattering theory. Further approximations were made so that these expressions could be written in closed form. An investigation of numerical results showed that the accuracy of the resulting expressions for the coherent scattered field is reasonable, especially in the forward scattering direction, but not very good. The simplified expression for the incoherent scattered field, on the other hand, gives excellent results.

Numerical results from the new scattering model were also compared with experimental data that were obtained by means of an accurate wideband measurement

technique. Measurements of the attenuated field behind the tree were observed to be disturbed by a ground-reflected wave, and could therefore not be used for a direct verification of the theoretical attenuation due to tree shadowing. Separation of ground-reflected waves from the direct wave is a difficult task for measurement configurations involving low transmitting and receiving antennas, because they have almost equal propagation delay times and angles-of-arrival (AOAs). An alternative method to measure the canopy's specific attenuation, which is complicated but probably more accurate, is to raise one of the antennas to a high level and use a directive antenna on the other side of the tree to eliminate the ground reflection. Values of α_c that were obtained in this way [56] are in good agreement with theoretical values found in this chapter. Theoretical values of the scattering cross section, which also depend on α_c, were shown to agree reasonably well with average measured data.

According to the new model, leaves have a considerable influence on the attenuation of radiowaves propagating through the canopy, but make hardly any difference with regard to the tree's scattering cross section. This result, which may at first seem surprising, was in fact verified by the experimental results discussed in Section 5.5.3, which showed little difference between the scattering cross section of a bare tree and the same tree in full leaf. From the viewpoint of radio network planning this is a convenient result, because it implies that (incoherent) tree-scattering models do not need to be season-dependent.

The new scattering model is unable to predict the considerable spatial fluctuations of the scattered field that were observed in the measurements. Indeed, it is likely that the unpredictability of these variations cannot be overcome by any propagation model, however sophisticated. Still, as the present model is capable of providing accurate average values of the scattered field, it can form an important improvement of the accuracy of propagation prediction models in vegetated urban environments.

6

A ray-tracing propagation prediction model for urban microcells

6.1 Introduction

With the advent of the microcellular radio networks that are likely to be employed in third-generation mobile communication systems such as UMTS, there is an increased interest in propagation models that are able to provide location-specific predictions of channel parameters such as local mean power and delay spread. Ray-tracing-based propagation prediction, in which the propagation of radiowaves is described in terms of straight trajectories in space called rays, has emerged as the most successful technique for this purpose. Quasi-two-dimensional ray-tracing models (often just called two-dimensional, or 2-D models) are quite adequate if transmission and receiving heights are well below the average rooftop level [48, 71], as is normally the case in urban microcells. These models have been reported to provide excellent prediction results for a variety of urban scenarios. In many other cases however, these models do not provide the same accuracy that can at present be achieved for macrocells.

Although currently available ray-tracing tools come in a wide variety with regard to the implementation of the ray-tracing algorithm itself, they are generally based on models of the same propagation mechanisms: line-of-sight propagation, reflection

and diffraction. It was shown in Chapter 3 of this thesis that in a number of frequently occurring scenarios these mechanisms alone do not adequately explain the actually observed channel properties. In particular, (1) transmission through buildings was shown to be a significant phenomenon behind buildings obstructing the line-of-sight to the base station antenna, and (2) scattering from trees located near street intersections was observed to play an important role concerning propagation around street corners. Models for these propagation mechanisms were developed in the Chapters 4 and 5. The present chapter presents a new 2-D ray-tracing-based propagation prediction tool that incorporates these models. It is based on the fully three-dimensional ray-tracing model *FiPre* that was originally developed for satellite applications [6] and later adapted to handle the large building databases and high ray orders required for propagation prediction for terrestrial mobile communications [7]. A detailed description of the implementation of the new tool is outside the scope of this thesis and will therefore not be given.

The organisation of this chapter is as follows. Section 6.2 gives a general description of the new propagation prediction model. It addresses the three main stages of the tool: database preprocessing, ray-tracing and channel parameter estimation. The estimation of local mean power, which is the most important channel parameter for the purpose of cell planning, is given special attention in Section 6.3. Section 6.4 presents prediction results for the two urban microcell environments previously considered in Chapter 3. Where possible, a comparison is made with measured field strength data. Conclusions are drawn in Section 6.5.

6.2 Model description

The propagation prediction model presented in this chapter is a quasi-2-D model. This means that the geometries of the scattering objects are described in two dimensions and that the base station antenna is modelled as being at the same height as the mobile station (even though this is normally not the case in reality), so that all rays propagate in a horizontal plane. Other than in truly 2-D models [40, 72], the base station antenna is modelled as a point source in three-dimensional space, which means that the radiated field diverges in both the horizontal and the vertical plane. As reported in [48, 71], quasi-2-D ray-tracing models are quite accurate when transmitting and receiving heights are well below the rooftops of surrounding buildings, as is usually the case in urban microcells. Under these conditions propagation takes place mainly at the street level, and propagation over rooftops is insignificant. The major advantage of quasi-2-D ray-tracing models, as compared to fully 3-D models, is their relatively low computational complexity.

The new prediction model accounts for the following propagation mechanisms

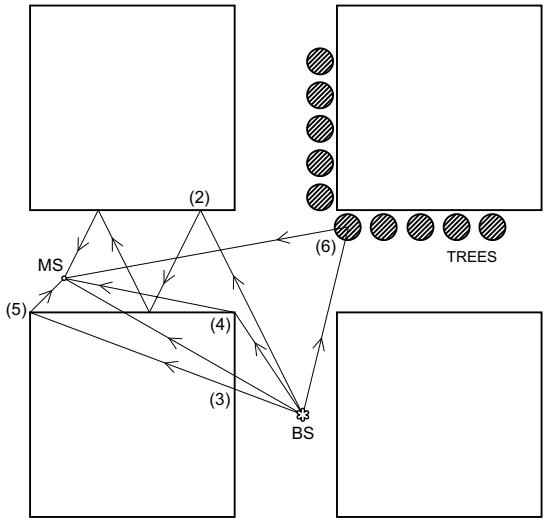

Fig. 6.1: Illustration of propagation mechanisms included in the prediction model.

(view Fig. 6.1):

1. direct, unobstructed propagation (not shown in Fig. 6.1),
2. reflection by building faces,
3. transmission through building faces,
4. external diffraction by building corners,
5. internal diffraction by building corners,
6. coherent and incoherent scattering from trees (which is assumed to take place at the tree centre),

and all possible combinations thereof, up to any predetermined number of interactions. In addition, a maximum number of interactions can be specified for each propagation mechanism separately. Ground reflections and rays over rooftops are neglected. As the present investigation is relevant to mobile communications, the electric field is assumed to be parallel to the building walls (vertical polarisation).

Transmission through buildings and scattering from trees are modelled in accordance with the theory presented in the Chapters 4 and 5 of this thesis. In addition to the external diffraction coefficient of Taket and Burge [45, 46] used in Chapter 4,

Luebbers' heuristic diffraction coefficient [43] and Tiberio-Maliuzhinets' diffraction coefficient for an impedance wedge [44] may be selected. The diffraction coefficients of Taket-Burge and Luebbers are used in conjunction with the Fresnel reflection coefficient; application of Tiberio-Maliuzhinets' diffraction coefficient requires the use of the reflection coefficient for impedance boundaries [44].

The inputs to the model include databases specifying the 2-D coordinates of the corners of each building and the locations, radii and heights of the trees, the complex permittivities ϵ_r and specific attenuation coefficients α_b of the buildings (cf. Section 4.2), and tables containing the equivalent scattering amplitudes $F^{\,\mathrm{eq}}(\hat{\mathbf{k}}_s, \hat{\mathbf{k}}_i)$ and cross sections $\sigma^{\,\mathrm{eq}}(\hat{\mathbf{k}}_s, \hat{\mathbf{k}}_i)$ per unit volume of the tree canopies (cf. Section 5.2.4). Also, the location and radiation pattern (in the horizontal plane) of the base station, the frequency and some other simulation parameters, such as the spatial resolution of the prediction and the permitted ray order, must be specified. Trees and the base station may not be located inside a building, but the observation point may be chosen arbitrarily. Modes of operation supported by the prediction model are field strength prediction over an area or along a trajectory, and determination of all ray trajectories for a set of discrete observation points.

The propagation prediction is basically performed in three phases. The first phase, which is referred to as database preprocessing, serves to decrease the computational complexity of the second and most intricate phase, which is formed by the ray-tracing. In the last phase, relevant channel parameters are predicted from the ray data. The procedures involved in these phases are outlined in the following (Sections 6.2.1, 6.2.2 and 6.2.3).

6.2.1 Database preprocessing

Generally, the most computationally intensive aspect of ray-tracing-based propagation prediction is formed by the tracing itself, i.e. by the algorithm that determines all possible rays between the source and observation points. In comparison, the computation of the complex field amplitudes associated with each ray is a small task. In cases in which ray contributions of second or higher order are taken into account, the ray-tracing can be accelerated considerably if one knows for all pairs of diffraction and/or scattering points if a ray between these points can exist. As these so-called visibility relations are independent of the locations of the base station and the observation points, they have to be determined only once, prior to the actual ray-tracing. The preprocessing procedure applied in the present model is similar to that proposed in [73], but it is more general in the sense that it does not just evaluate *if* the ray between two points is obstructed, but also by how many building faces. This is essential for tracing rays that propagate through buildings.

The computation time needed for the ray-tracing can be reduced further by subdi-

viding the building faces into smaller "tiles" and determining the visibility relations of the tile centres with other tiles, building corners and trees, together with a number of angles [73]. As this technique introduces small errors that may obscure the errors resulting from inadequacies of the physical models presented in this thesis, it is not used here.

The visibility relations of the base station and the observation points with the diffraction and scattering points must be determined during the actual ray-tracing. The processing time required for these computations is reduced through another form of preprocessing of the building database. This procedure consists of the computation and storage of each building's *bounding circle* [74], which is defined by the building's centre of gravity [75] and the radius of the smallest circle – centred at the centre of gravity – enclosing the building. When searching for building faces obstructing a given ray path, first a selection is made of buildings whose bounding circles intersect the ray path. This involves only a relatively simple computation. In practice, this selection procedure excludes the majority of candidate obstructing buildings from further examination.

6.2.2 Ray-tracing

The ray-tracing algorithm makes use of the concept of virtual sources, which account for the reflections, diffractions and scattering resulting from interaction of the field radiated from the base station antenna with the environment [48]. As the name implies, these virtual sources are not real sources but imaginary ones that, in combination with the real source (the base station antenna), form an equivalent system that replaces the actual system and gives the same radiated field as the actual system itself. Five types of virtual sources can be distinguished:

1. reflection sources,
2. external diffraction sources,
3. internal diffraction sources,
4. coherent scattering sources, and
5. incoherent scattering sources.

In the presence of buildings or trees, the real source formed by the base station gives rise to one or more virtual sources. In turn, these sources also interact with the environment and generate secondary virtual sources. This process is repeated until the specified maximum ray order is reached. If proper account is taken of the zones in which each source is "visible" (possibly through one or more building faces),

the total field at any observation point can be computed as the vector sum of the contributions from all sources.

The generation of virtual sources is now described in more detail. New diffraction and scattering sources are formed at building corners and trees which are "illuminated" (possibly through one or more building faces) by a source of lower order or "parent" source. Every building face illuminated by a parent source forms one or more new reflection sources, which are the mirror images of the parent source (view Fig. 6.2). A so-called illumination zone [48, 76], which is the area in which a valid reflected ray exists, is associated with each reflection source. Only building faces, corners and trees inside the illumination zone of a parent reflection source can produce higher-order virtual sources, or "children". Other faces, corners and trees do not need to be considered. The illumination zones tend to get narrower as the reflection order increases. This prevents the number of images – and hence the computation time – from increasing exponentially with the permitted ray order, and makes it feasible to produce accurate field predictions for large and complicated environments. Diffraction sources also have illumination zones associated with them, but these depend only on the geometry of the building corner, and not on the location of the parent source. The illumination zones of the base station antenna and of scattering sources are always identical to the infinite two-dimensional plane.

If the number of building faces intersecting the line-of-sight between a parent source and a reflecting building face takes different values for different sections of the reflecting face, a separate reflection source is associated with each section, each with a unique illumination zone. This is illustrated in Fig. 6.2, where the left section of building face 1 is illuminated by rays transmitted through two obstructing faces, and the right section is directly illuminated. Two new reflection sources – SRC(1) and SRC(2) – are therefore generated for building face 1. Each of these first-order sources gives rise to a second-order reflection source that accounts for subsequent reflection from building face 2. These second-order sources – SRC(1,1) and SRC(2,1) – also have unique illumination zones. Using these illumination zones it is easy to establish whether rays of a given sort are possible. For example, transmitted rays first reflected from building face 1 and subsequently reflected from building face 2 are possible only if the observation point is in the illumination zone of SRC(2,1).

The sources found in the ray-tracing procedure are categorised in a hierarchical fashion, in a tree structure called a source tree [48, 76]. The root of the source tree is formed by the base station antenna, and each next level contains the children of the sources in the previous level. Each of the sources in the source tree is capable of providing a valid path if the observation point lies in its illumination zone.

To treat multiple interactions of radiowaves with the environment in a proper way, it is necessary to accurately keep track of the relevant ray parameters. At every

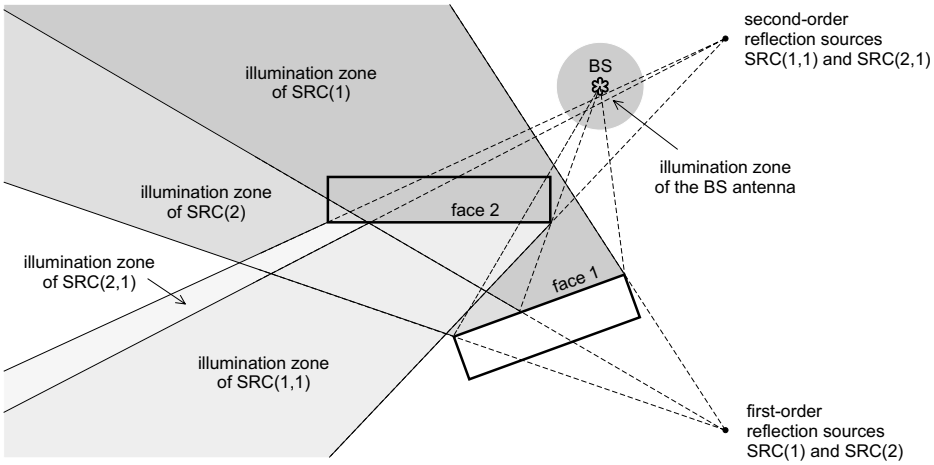

Fig. 6.2: Illustration of the generation of reflection sources.

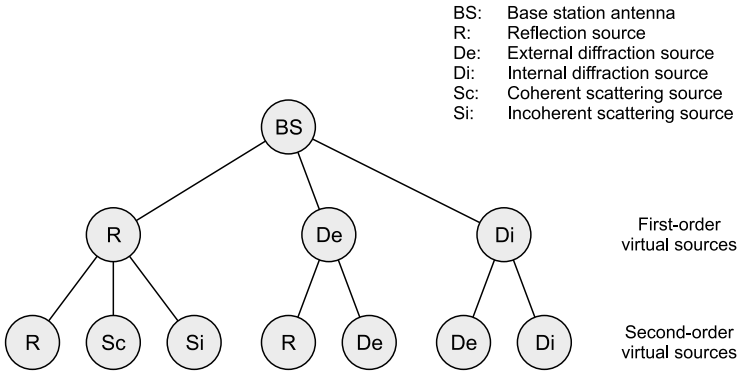

Fig. 6.3: Example of a source tree.

point in space, a radiowave is characterised by its direction of propagation $\hat{\mathbf{k}}_i$, its vertical and horizontal radii of curvature r_1 and r_2, and the complex amplitude of the electric field. The interaction with an obstacle involves a transformation from incident-wave parameters at the interaction point to outgoing-wave parameters evaluated at either the next interaction point or the observation point [74]. Every time a new diffraction or scattering source is generated, the incident-wave parameters are determined and stored in the source tree, together with the type and coordinates of the new source, some parameters describing the illumination zone, and the number of previous interactions of each type. This information is later retrieved and used to

generate higher-order sources or to evaluate the field at the observation point. New reflection sources are treated differently; as the precise location of the reflection point is unknown when a new reflection source is generated, the associated incident-wave parameters cannot be determined. The reflection points and reflection coefficients of (multiply) reflected rays are computed at a later stage, when higher-order diffraction or scattering sources are generated or the field at the observation point is evaluated.

In the computation of the field amplitude due to the base station antenna or a virtual source which only has reflection sources as its parents, the directivity of the base station antenna is taken into account, i.e., the field is weighted by the envelope of the antenna's radiation pattern in the direction of the launched ray.

6.2.3 Channel parameter estimation

For a given observation point and permitted ray order, the ray-tracing algorithm generates the set of all valid ray trajectories, and the associated complex electric field amplitudes. In order to find the complex signals at the output of the receiving antenna due to these rays, their field amplitudes are weighted by the envelope of the antenna's radiation pattern. In the present model, the receiving antenna is assumed to be non-directional in the horizontal plane, so that it can be characterised by a single gain value. For each multipath wave, the delay time can be computed from the total length of the associated ray trajectory and the angle-of-arrival (AOA) is found as the direction of the (virtual) source that is responsible for the ray. Important channel characteristics such as the received field strength, power delay profile, power angular profile and power Doppler profile (Doppler spectrum), as well as multi-dimensional characteristics like the temporal-angular power distributions discussed in the Chapters 2 and 3 of this thesis, can be computed from the ray parameters. In a second step, channel parameters such as delay spread, mean AOA, angular spread, mean Doppler shift and Doppler spread can be derived from these simulated characteristics.

In this chapter it has been assumed that the geometrical and dielectric features of the environment, the locations of the base station antenna and the observation points, the frequency, etc. are deterministic, constant and exactly known. The predicted channel parameters therefore also have a deterministic and constant nature. There is one source of randomness, however, which is very important in propagation prediction for the purpose of network planning, and this is the uncertainty with regard to the exact receiver position. In the planning stage of cellular radio networks, channel parameters are usually determined for a set of discrete points, but they are assumed to be representative for an observation area around each point. The dimensions of such an area (sometimes called *pixel*) depend on the desired spatial resolution of the prediction, but they are typically in the order of several tens of wavelengths. The actual receiver location is implicitly assumed to be random within the observation area,

and the radio channel properties at this location can be characterised by *local mean* channel parameters, of which the local mean power is probably the most important one.

The estimation of local mean power from ray parameters generated using a 2-D ray-based propagation prediction model is the subject of the next section. With some minor modifications, this method can also be used to estimate local mean power delay profiles.

6.3 Estimation of local mean power

Probably the most important channel parameter used in the planning stage of radio networks is the local mean power, which is the total received signal intensity, averaged in space in order to remove small-scale fading. A method which is often used to estimate local mean power is to simply add the individual ray powers [48, 71, 77]. This method has been referred to as the sum-of-individual-ray-powers (SP) method in [71]. This section presents an alternative method, which is based on the spatial average (SA) of the received power over a given pixel area, but does not require ray-tracing for more than one observation point per pixel [78]. This SA method consists of the evaluation of an expression for the local mean power that is exact assuming that the ray amplitudes and AOAs are constant over the pixel area. Unlike the SP method, the SA method provides a statistically valid approximation of the expected field strength at a random receiver position within a given observation area. Furthermore, this method allows a fairer comparison to be made between propagation predictions and propagation measurement data obtained with a moving receiving antenna, in which the long-term fading component is usually also determined by spatial averaging – albeit in only one dimension.

6.3.1 Formulation

Consider the area S around the observation point O which is assumed to be at the origin of a rectangular coordinate system (x, y), and assume that N rays are incident on O from the AOAs φ_n, $n = 1, 2, \ldots, N$ (view Fig. 6.4). Associated with each ray is a narrowband signal with amplitude u_n and phase ϕ_n. If u_n and φ_n do not vary over the observation area S (plane wave assumption), the total received signal s can be evaluated at any point within S by taking the sum of the individual complex ray amplitudes (e.g. [71, 79]), i.e.

$$s(x, y) = \sum_{n=1}^{N} u_n \exp[jk(x \cos\varphi_n + y \sin\varphi_n) + j\phi_n], \tag{6.1}$$

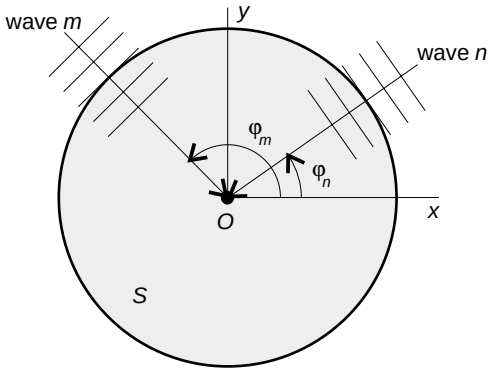

Fig. 6.4: Horizontal observation area S with incident multipath rays.

k being the free-space wavenumber, and the corresponding received power is

$$p(x, y) = |s(x, y)|^2 . \tag{6.2}$$

Both $s(x, y)$ and $p(x, y)$ are deterministic functions of the coordinates x and y, and the known ray parameters u_n, ϕ_n and φ_n.

The received power at a random observation point X in S obviously has a probabilistic nature, and will be denoted by the random variable $P = p(X)$. Here, we assume that the (two-dimensional) random location variable X has a probability distribution $f_X(x, y)$ that is uniform in S. Under this assumption the statistical mean $\overline{P}$ of the received power is identical to the received power averaged over S.

6.3.2 Computation of local mean power

The mean power $\overline{P}$ in the observation area S can be found by integration of the product $p(x, y) f_X(x, y)$ over S, which gives

$$\overline{P} = \sum_{n=1}^{N} u_n^2 + 2 \sum_{m=1}^{N} \sum_{n<m} u_m u_n \mathrm{Re}\{\rho_{mn}\}, \tag{6.3}$$

where

$$\begin{aligned} \rho_{mn} = \iint_S & \exp[jk(x \cos\varphi_m + y \sin\varphi_m) + j\phi_m] \\ & \times \exp[-jk(x \cos\varphi_n + y \sin\varphi_n) - j\phi_n] f_X(x, y) dx dy, \end{aligned} \tag{6.4}$$

is a complex scalar that lies on or inside the unit circle and represents the correlation between the mth and the nth multipath signal in S. When ρ_{mn} lies on the unit circle,

the two signals are fully coherent. If ρ_{mn} lies inside the unit circle, the two signals are only partially correlated, while $\rho_{mn} = 0$ implies totally uncorrelated multipath signals. The SA method presented in this section consists of the evaluation of equation (6.3), including the terms containing the spatial correlation coefficients, which are not taken into account by the conventional SP method.

For a rectangular observation area centred at O, with sides of lengths D_x and D_y aligned with the x and y axes, respectively, ρ_{mn} can be written as

$$\rho_{mn} = \frac{\sin[kD_x(\cos\varphi_m - \cos\varphi_n)/2]}{kD_x(\cos\varphi_m - \cos\varphi_n)/2} \times \frac{\sin[kD_y(\sin\varphi_m - \sin\varphi_n)/2]}{kD_y(\sin\varphi_m - \sin\varphi_n)/2} \exp[j(\phi_m - \phi_n)]. \tag{6.5}$$

The predicted local mean power along a measurement trajectory can be obtained by locally orienting the (x, y) coordinate system with the x axis parallel to the trajectory, making D_x equal to the averaging interval applied in the measurements, and letting $D_y \to 0$, so that the second factor in (6.5) vanishes. For a circular observation area of diameter D centred at O, ρ_{mn} becomes

$$\rho_{mn} = \frac{2J_1\big(kD\sin[(\varphi_m - \varphi_n)/2]\big)}{kD\sin[(\varphi_m - \varphi_n)/2]} \exp[j(\phi_m - \phi_n)], \tag{6.6}$$

where $J_1(\cdot)$ is the Bessel function of the first kind of order one. Finally, for the prediction of the mean power received along a horizontal circle centred at O with diameter D (ring-shaped observation domain), ρ_{mn} is given by

$$\rho_{mn} = J_0\big(kD\sin[(\varphi_m - \varphi_n)/2]\big) \exp[j(\phi_m - \phi_n)], \tag{6.7}$$

where $J_0(\cdot)$ is the Bessel function of the first kind of order zero. Plots of the absolute correlation $|\rho_{12}|$ between two multipath signals, computed from (6.5)–(6.7), are shown in Fig. 6.5 as a function of the angular difference $\Delta\varphi = \varphi_2 - \varphi_1$, for $kD_x = kD_y = kD = 100$.

Expression (6.3) simplifies for the specific cases in which all multipath signals are totally correlated or uncorrelated. For nearly uncorrelated multipath signals ($\rho_{mn} \simeq 0$, $m \neq n$), $\overline{P}$ can be approximated as the sum of the individual multipath signal powers, as in the SP method:

$$\overline{P} \simeq \sum_{n=1}^{N} u_n^2. \tag{6.8}$$

From (6.3)-(6.7) it is seen that the SP method is generally valid only if at least one of the dimensions of the observation domain is large in terms of the wavelength, and all

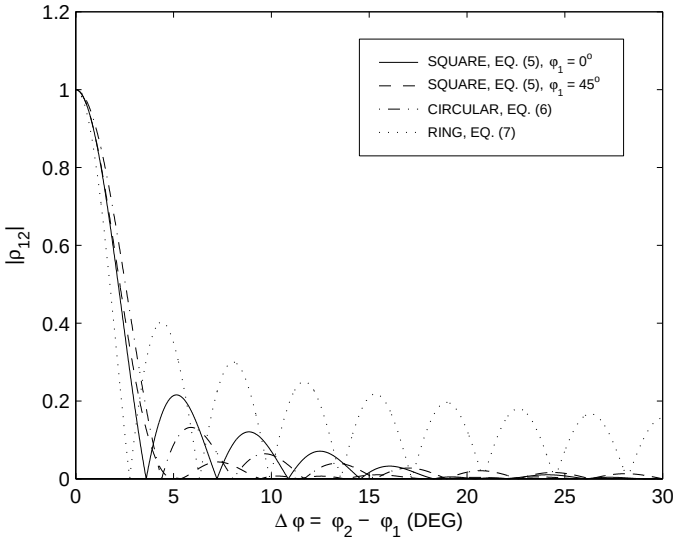

Fig. 6.5: Magnitude of the correlation coefficient versus the angular difference $\Delta\varphi = \varphi_2 - \varphi_1$, for a square observation area with $kD_x = kD_y = 100$, $\varphi_1 = 0°$, a square observation area with $kD_x = kD_y = 100$, $\varphi_1 = 45°$, a circular observation area with $kD = 100$, and a ring-shaped observation domain with $kD = 100$.

rays are sufficiently spaced in angle. If all multipath signals are almost completely correlated ($|\rho_{mn}| \simeq 1$, $m \neq n$), then $\mathrm{Re}\{\rho_{mn}\} \simeq \cos(\phi_m - \phi_n)$, and the local mean power is well approximated by the received power at the observation point O, which is calculated as the power of the vector sum of the individual signals:

$$\overline{P} \simeq \left| \sum_{n=1}^{N} u_n \exp(j\phi_n) \right|^2 . \tag{6.9}$$

From (6.3)-(6.7) it is clear that this approximation is good as long as all dimensions of the observation area are small compared to the wavelength, or the angular region from which all rays arrive is sufficiently small. In all other cases, in which one or more pairs of multipath signals are partially correlated, neither the SP method nor the received power at O forms a generally valid approximation of equation (6.3).

6.3.3 Numerical results

In this section, local mean power predictions computed using the SA method presented in this paper are compared with results obtained using the SP method in some simple test environments composed of one or more of the buildings marked as A–D

in Fig. 6.6. Some of the configurations that can be composed in this way, such as the so-called 2-corner and 4-corner street intersections, have been investigated previously to study radio propagation around street corners [31, 48, 71]. In the present simulations, local mean power estimates are compared with each other and with the received power along the trajectory indicated in Fig. 6.6, and spatial distributions of the error made by the SP method (as compared with the SA method) are given for the complete coverage area. The transmitter is situated at a fixed location, indicated by the label "BS". Reflections up to tenth order and/or diffraction up to order two are taken into account, and the carrier frequency is 900 MHz. The diffraction contributions are computed using the diffraction coefficient for a wedge with impedance faces [44]. A relative permittivity of $\epsilon_r = 5.3$ and zero conductivity, corresponding to dry brick, are selected for the buildings.

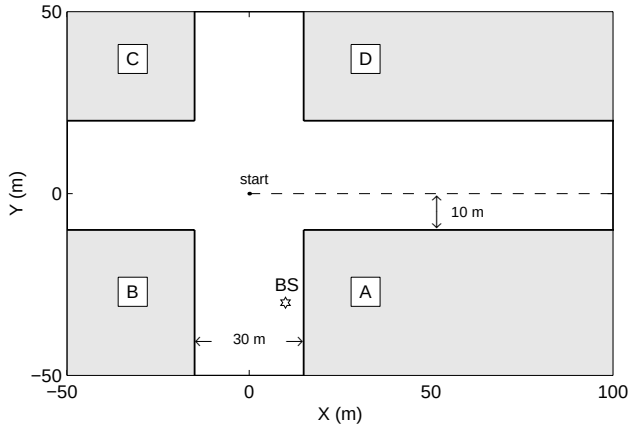

Fig. 6.6: Configuration of the test environment. Trajectory is indicated by the dashed line. "BS" denotes the base station location.

Figs. 6.7 and 6.8 show the predicted received power and the local mean power estimates along the trajectory, evaluated by means of the SP method and the SA method, for configurations consisting of buildings A+B (2-corner intersection) and buildings A+B+C+D (4-corner intersection), respectively. The received power is computed every 5 cm, while the local mean power estimates are evaluated every 5 m. For the SA method, a 5-m averaging interval (Eqn. (6.5), with $D_x = 5$ m, $D_y = 0$) is applied. In the 2-corner intersection case of Fig. 6.7, the received power shows rapid fluctuations at distances close to the transmitter. As desired, the local mean power, estimated by either the SA or the SP method, does not follow these small-scale fluctuations. At larger distances from the transmitter, the SP method no

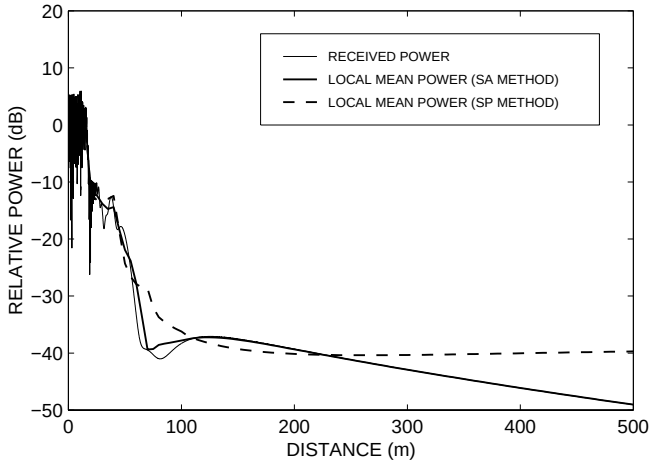

Fig. 6.7: Received power and local mean power estimates along the trajectory in configuration A+B (2-corner intersection). Local mean power estimates are computed using the SA method (Eqn. (6.5), with $D_x = 5$ m and $D_y = 0$) and the SP method. Powers are relative to the free-space level.

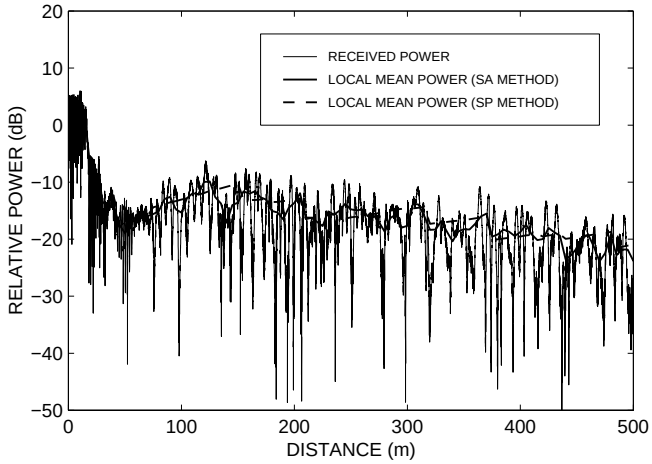

Fig. 6.8: Received power and local mean power estimates along the trajectory in configuration A+B+C+D (4-corner intersection). Local mean power estimates are computed using the SA method (Eqn. (6.5), with $D_x = 5$ m and $D_y = 0$) and the SP method. Powers are relative to the free-space level.

longer accurately predicts the local mean power, whereas the SA method provides a good approximation at all distances from the transmitter. The error made by the SP method amounts to 10 dB at 500 m from the transmitter. In the 4-corner intersection case of Fig. 6.8, on the other hand, the received power shows fast fluctuations along the entire 500-m trajectory, and the SA and SP methods provide very similar results.

A physical explanation for the observations made above can be given after considering the spatial distribution of the error made by applying the SP method, as compared with the SA method. Fig. 6.9 shows the error distribution for a configuration composed of building A only (1-corner intersection). The largest errors, ranging up to 7 dB, are found near the shadow boundary of the incident field. In this region the first Fresnel zone of the direct wave is partially obstructed by building A, which is accounted for by ray-based diffraction theory through destructive interference with the wave diffracted from the corner of building A. In the SP method however, the power of this diffraction contribution is *added* to the power of the direct wave, which results in an overestimation of the local mean power. The SA method handles the contribution of the diffracted ray signal to the local mean power in a correct manner, by taking into account its high correlation with the "direct" signal. In the configuration considered here equally large errors do not occur near the reflection boundary, because the field in this region is dominated by the direct wave. Smaller, but significant errors occur in regions where the signals associated with the direct wave and the reflection from the wall behind the transmitter become strongly correlated.

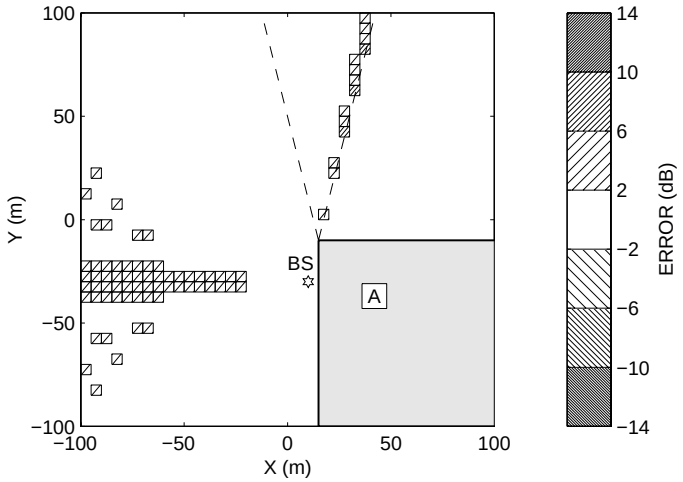

Fig. 6.9: Spatial distribution of the SP estimation error (relative to the SA method) for configuration A only (1-corner intersection). $D_x = D_y = 5$ m. "BS" denotes the base station location. Dashed lines indicate shadow and reflection boundaries of the direct ray.

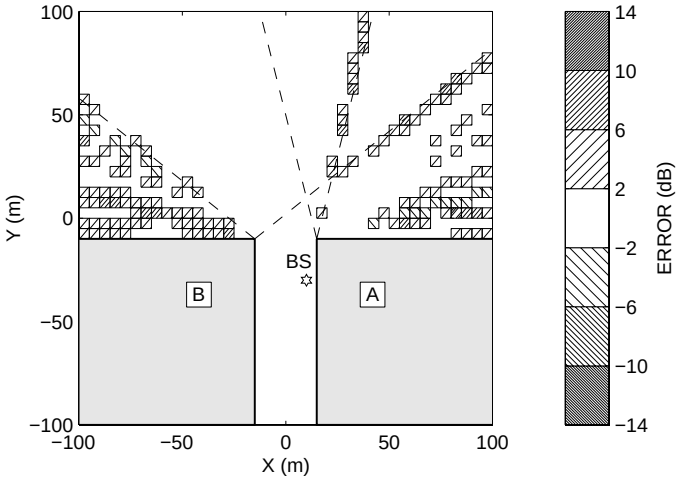

Fig. 6.10: Spatial distribution of the SP estimation error (relative to the SA method) for configuration A+B (2-corner intersection). $D_x = D_y = 5$ m. "BS" denotes the base station location. Dashed lines indicate shadow and reflection boundaries of the direct ray.

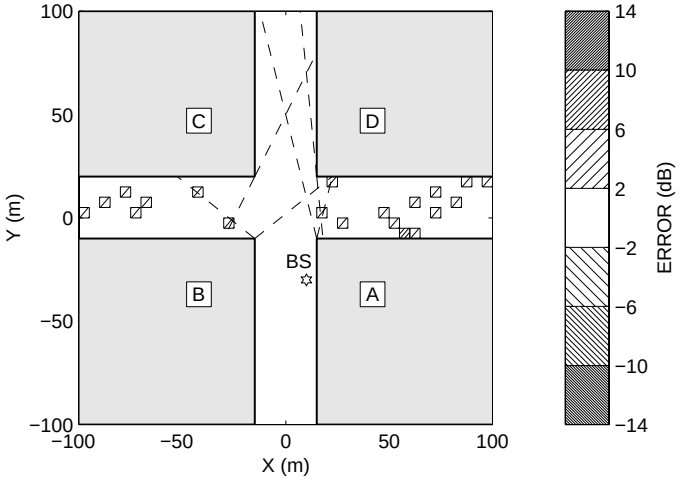

Fig. 6.11: Spatial distribution of the SP estimation error (relative to the SA method) for configuration A+B+C+D (4-corner intersection). $D_x = D_y = 5$ m. "BS" denotes the base station location. Dashed lines indicate shadow and reflection boundaries of the direct ray.

Similar plots of the error distributions for the configurations A+B and A+B+C+D are shown in Figs. 6.10 and 6.11. Instead of two there are now many shadow boundaries, each one associated with one of the many multipath waves reflected and/or diffracted between the buildings. For the 2-corner intersection of Fig. 6.10 this results in considerable errors in large parts of the coverage area, as was also observed from Fig. 6.7. On the other hand, in the 4-corner intersection configuration of Fig. 6.11 the diffraction contributions are dominated by multiple reflections in the street canyons formed by all four buildings, and these waves impinge on the receiver from a relatively wide angular region. The associated multipath signals therefore have low correlation, so that in this case the SP method provides a good approximation of the local mean power in most of the coverage area, including the trajectory of Fig. 6.6.

6.3.4 Conclusions and discussion

In this section, an accurate method for determining local mean power using 2-D ray-tracing based propagation prediction models was proposed. This method, which consists of the evaluation of equation (6.3), automatically reduces to the commonly used SP method for uncorrelated multipath signals, but, unlike the SP method, remains valid for correlated signals, i.e. for rays arriving at the receiver from a narrow angular region. Although it is based on the spatial average (SA) of the received power, the presented method does not require the calculation of the received power at many discrete points within each observation area or interval, as in [71].

Numerical results for some simple test configurations show that application of the SP method can result in considerable estimation errors, while the new SA method remains accurate in all cases – at the cost of slightly increased computational complexity. They further indicate that poor performance of the SP method occurs particularly near the shadow boundaries associated with diffracted rays. In the most complex test environment considered (Fig. 6.11), the SP method was shown to give results similar to the new SA method. Although this may suggest that the conventional power sum gives a sufficiently good approximation of the local mean power in complex environments, it is hard or even impossible to say in general for what building configurations and/or in which parts of a reception area the SP method provides accurate results.

The presented method can be extended to 3-D ray-tracing models in a straightforward manner. Computation of the local mean power then involves an integration of the received power over a volume around each observation point, and the correlation between multipath signal pairs will depend on the angular spacing of the corresponding rays in both azimuth and elevation.

6.4 Prediction results

This section presents prediction results for two urban microcell environments that were previously discussed in Chapter 3 of this thesis. It is aimed at illustrating the improvement in accuracy that can be achieved by incorporating appropriate models for transmission through buildings and scattering from trees. Where possible, a comparison is made with measured data.

The predictions in this section are generated for a carrier frequency of 1890 MHz. The relative dielectric permittivity of the buildings, ϵ_r, is chosen equal to 5, and the conductivity is zero. The specific attenuation constant α_b, which characterises the attenuation of waves propagating through buildings, is assumed to be 2.0 dB/m, which is the average of the empirical values found in Chapter 4. Reflected and diffracted fields are computed using the Fresnel reflection coefficient and the diffraction coefficients of Taket and Burge [45, 46], respectively. All branch and leaf parameters are taken from Chapter 5, particularly from Table 5.1. The prediction area is divided into 5×5 m^2 square pixels. For each pixel the local mean power, required to compute the (local mean) path loss, is obtained using the SA method proposed in the previous section.

6.4.1 Transmission through buildings – Bern

Fig. 6.12 shows area predictions of path loss for an urban microcell environment in Bern (cf. Section 3.2.1), with and without considering transmission through buildings. In generating the prediction result shown in Fig. 6.12(a), the maximum number of wall transmissions was set to one, so that rays can penetrate into buildings but cannot be transmitted through them. The results shown in Fig. 6.12(b), on the other hand, were obtained by setting the maximum transmission order to three, permitting rays to be transmitted through maximally one building and then penetrate a second one. The diffraction order was one and tree-scattering was not considered. The white observation areas (pixels) that can be seen in both subfigures correspond with areas that cannot be "reached" by rays permitted in the present simulation. Obviously, a larger fraction of the total area can be reached if transmission through buildings is permitted. Significant differences between the prediction results of Fig. 6.12(a) and (b) are observed in Rodtmatt Street and Wiesen Street, opposite to the base station. In these areas, differences up to approximately 50 dB occur.

A detailed comparison between measured data obtained from [29, 48] and predictions generated with and without considering building transmission was made for the trajectory indicated in Fig. 6.12. The number of observation points on this trajectory is 92. Table 6.1 shows the mean and rms prediction errors obtained for various (maximum) ray orders. The diffraction order – the maximum number of external

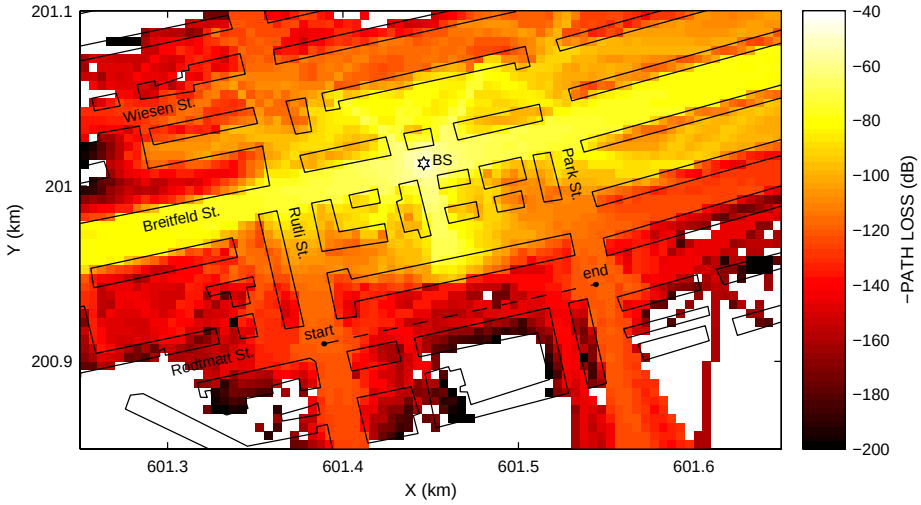

(a)

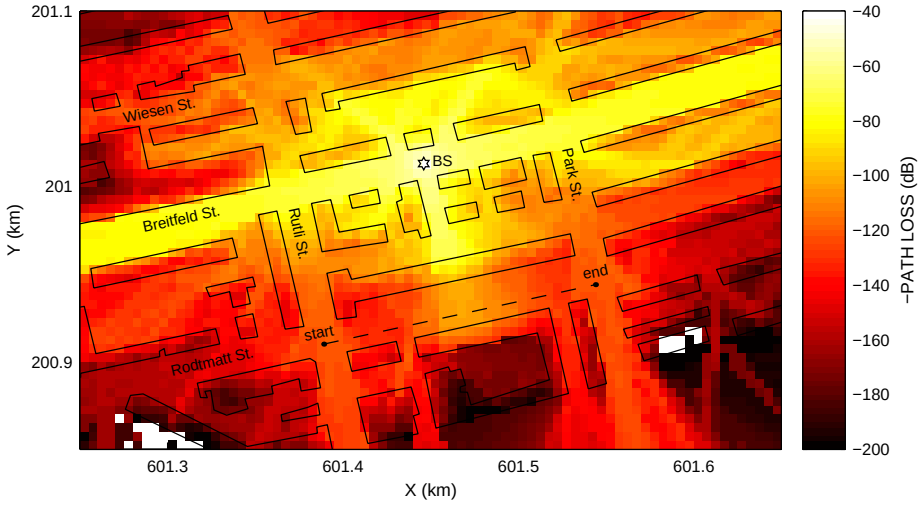

(b)

Fig. 6.12: Area predictions of local mean power for the urban microcell configuration in Bern, for (a) transmission order one and (b) transmission order three. Predictions were generated considering five reflections, one diffraction and no scattering. “BS” denotes the base station location.

Table 6.1: Prediction errors and number of sources for the urban microcell configuration in Bern, for various ray orders.

Max. ray order	Number of sources	Mean error (dB)	Rms error (dB)
1 refl., 1 transm., 1 diffr., 0 scatt.	826	–	–
2 refl., 1 transm., 1 diffr., 0 scatt.	2,955	–	–
3 refl., 1 transm., 1 diffr., 0 scatt.	7,475	–	–
4 refl., 1 transm., 1 diffr., 0 scatt.	15,697	-31.7	36.7
5 refl., 1 transm., 1 diffr., 0 scatt.	29,048	-29.8	33.7
6 refl., 1 transm., 1 diffr., 0 scatt.	49,441	-28.8	32.4
7 refl., 1 transm., 1 diffr., 0 scatt.	78,897	-27.2	30.6
8 refl., 1 transm., 1 diffr., 0 scatt.	120,120	-26.3	29.4
9 refl., 1 transm., 1 diffr., 0 scatt.	175,568	-26.6	29.7
1 refl., 3 transm., 1 diffr., 0 scatt.	3,211	-14.4	18.4
2 refl., 3 transm., 1 diffr., 0 scatt.	15,252	-10.3	14.1
3 refl., 3 transm., 1 diffr., 0 scatt.	46,298	-8.9	12.4
4 refl., 3 transm., 1 diffr., 0 scatt.	111,475	-8.0	11.5
5 refl., 3 transm., 1 diffr., 0 scatt.	230,853	-7.6	11.2
6 refl., 3 transm., 1 diffr., 0 scatt.	431,439	-7.4	11.0
1 refl., 5 transm., 1 diffr., 0 scatt.	8,121	-13.4	17.0
2 refl., 5 transm., 1 diffr., 0 scatt.	48,273	-10.0	13.9
3 refl., 5 transm., 1 diffr., 0 scatt.	170,128	-8.7	12.2
4 refl., 5 transm., 1 diffr., 0 scatt.	462,008	-7.9	11.4

and internal diffractions permitted for each ray – was set to one, and the scattering order to zero. For transmission order one and reflection orders less than four, some points on the trajectory are not reached by at least one ray, so that the prediction error is meaningless. Increasing the reflection order is seen to gradually reduce the prediction error, until convergence is reached at some point. A very significant improvement is obtained, however, if rays are permitted to propagate through buildings. In that case, the rms error drops from 30 to 11 dB. A further increase of the transmission order to five, allowing rays to be transmitted through two buildings, does not lead to further improvement. Table 6.1 also shows the total number of sources found in the ray-tracing procedure. This number, and with it the computational load, is seen to rise sharply with the number of ray interactions considered. Yet, by considering building transmission a much better prediction accuracy can be achieved with roughly the same number of sources.

Fig. 6.13 shows the measured and predicted path loss along the trajectory, for reflection order five, diffraction order one and transmission orders one and three. Again, the large improvement due to taking into account transmission through buildings can be clearly seen, especially in the middle part of the trajectory. A considerable difference between measurement and prediction remains near the intersections with Rutli and Park Street. This may be the result of the neglect of scattering from trees, which are found in the entire area.

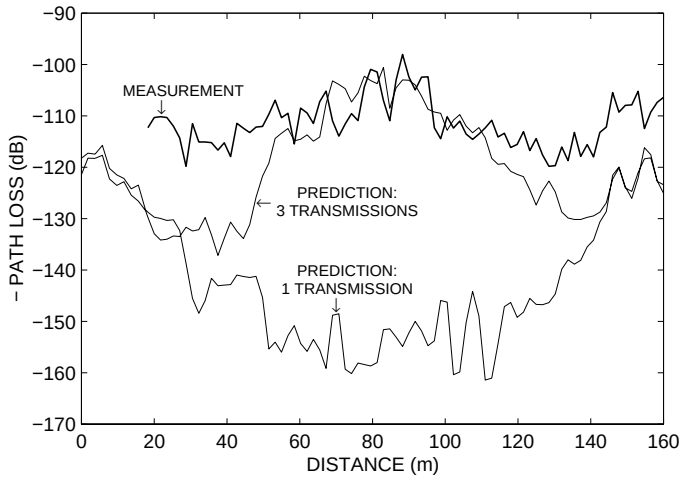

Fig. 6.13: Measured and predicted path loss along the trajectory in Bern. Predictions were generated considering five reflections, one diffraction and no scattering.

6.4.2 Scattering from trees – Fribourg

Fig. 6.14 shows area predictions of path loss for an urban microcell environment in Fribourg (cf. Section 3.3.1), with and without considering scattering from trees. The trees, represented by green circles, have a radius of 3 m and a height of 6 m. The tree locations indicated in Fig. 6.14 and used in generating the predictions are not claimed to be exact, but do represent an adequate picture of the actual situation. The prediction result of Fig. 6.14(a) was obtained by setting the scattering order to zero, while the result of Fig. 6.14(b) was generated for scattering order one, allowing maximally one coherent or incoherent scattering per ray. The maximum number of transmissions was set to one, so that penetration into buildings was permitted (but not transmission through them), and the diffraction order was one. As previously, the white pixels correspond with observation areas for which no rays exist, given the permitted ray order. Distinct differences between the prediction results of Fig. 6.14(a) and (b) are observed in Perolles Street outside the line-of-sight region. In some parts, these amount to over 20 dB. In qualitative terms, the field in Fig. 6.14(b) appears to be much more diffuse.

A detailed comparison between measured data obtained from [29, 31, 48][1] and predictions produced with and without taking into account scattering from trees was made for the trajectory indicated in Fig. 6.14. The number of observation points on this trajectory is 64. The prediction results were obtained by setting the transmission and diffraction order to one. Mean and rms prediction errors obtained for various ray orders are shown in Table 6.2. This table also gives the number of sources found in the ray-tracing procedure. As in the scenario considered in the previous section, increasing the reflection order gradually reduces the prediction error until convergence is reached. A much larger improvement is achieved, however, by taking into account the effects of tree-scattering. This leads to a reduction of the rms prediction error from more than 13 to less than 4 dB. It was found that in the present scenario the prediction accuracy cannot be improved further by considering transmission through buildings. The effects of multiple tree-scattering per ray were not investigated because of the explosive growth of the number of sources, and hence the computational intensity, resulting from an increase of the scattering order.

Fig. 6.15 shows the measured and predicted path loss along the trajectory, with and without tree-scattering. The reflection order is three, and the transmission and diffraction order are both set to one. The improvement due to considering tree-scattering is remarkable. Note that the total effect of incoherent tree-scattering is not very sensitive to the exact number of trees or to their radii and heights. Indeed, a simple theoretical argument shows that doubling the number of trees or the volumes

[1] A 10-dB offset must be added to the measured data published in [29, 48] (cf. [31]).

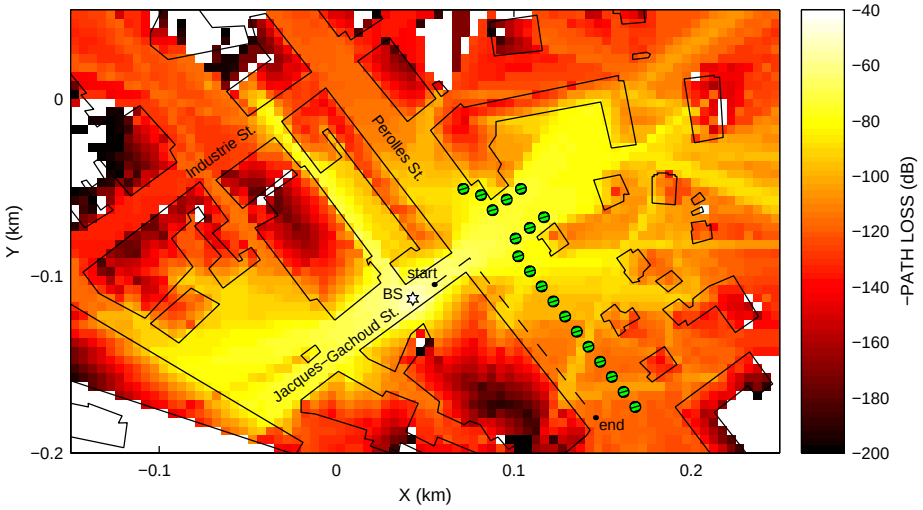

(a)

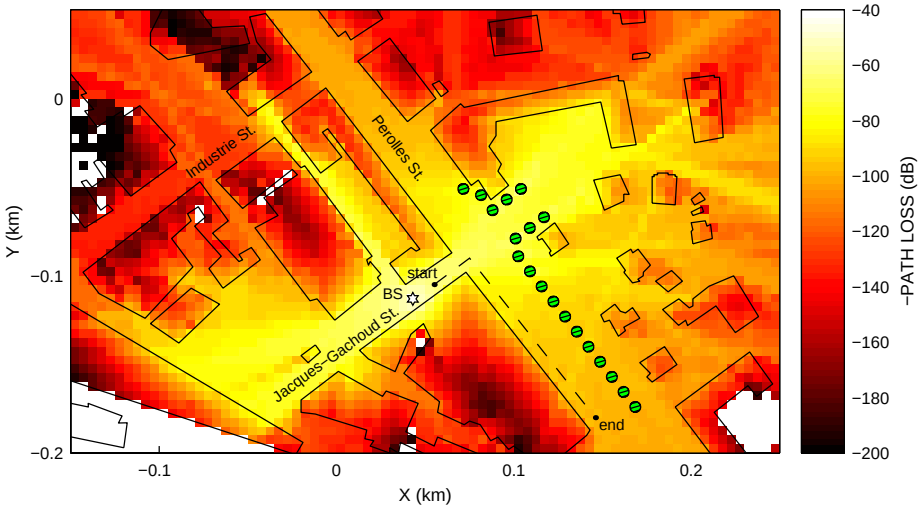

(b)

Fig. 6.14: Area predictions of local mean power for the urban microcell configuration in Fribourg, for (a) scattering order zero and (b) scattering order one. Predictions were generated considering three reflections, one transmission and one diffraction. “BS” denotes the base station location.

Table 6.2: Prediction errors and number of sources for the urban microcell configuration in Fribourg, for various ray orders.

Max. ray order	Number of sources	Mean error (dB)	Rms error (dB)
1 refl., 1 transm., 1 diffr., 0 scatt.	619	-15.5	18.1
2 refl., 1 transm., 1 diffr., 0 scatt.	2,641	-11.3	14.4
3 refl., 1 transm., 1 diffr., 0 scatt.	7,849	-10.2	13.7
4 refl., 1 transm., 1 diffr., 0 scatt.	18,144	-10.1	13.5
5 refl., 1 transm., 1 diffr., 0 scatt.	35,896	-9.9	13.3
6 refl., 1 transm., 1 diffr., 0 scatt.	63,107	-9.9	13.3
7 refl., 1 transm., 1 diffr., 0 scatt.	102,165	-9.9	13.2
1 refl., 1 transm., 1 diffr., 1 scatt.	10,551	-1.1	3.6
2 refl., 1 transm., 1 diffr., 1 scatt.	63,228	0.1	3.3
3 refl., 1 transm., 1 diffr., 1 scatt.	237,539	0.3	3.5
1 refl., 3 transm., 1 diffr., 1 scatt.	97,183	-1.0	3.6
2 refl., 3 transm., 1 diffr., 1 scatt.	612,735	0.2	3.4

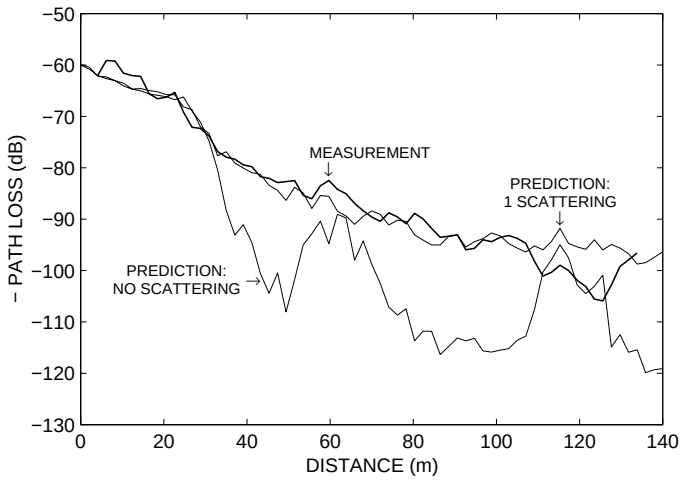

Fig. 6.15: Measured and predicted path loss along the trajectory in Fribourg. Predictions were generated considering three reflections, one transmission and one diffraction.

of their canopies would result in an increase of the incoherent scattered field by no more than roughly 3 dB.

6.5 Conclusions

A ray-tracing-based propagation prediction model has been presented that incorporates models for transmission through buildings and scattering from trees. The model is two-dimensional in the sense that it neglects propagation over rooftops. This approximation is valid for urban microcell configurations in which the base station antenna is located well below the rooftop level. Due to its relatively low computational complexity, the model is capable of handling large building databases and high ray orders in modest computation times, i.e. the most complex computations considered in this section were performed within a few hours.

The model consists of three major stages: database preprocessing, ray-tracing and channel parameter estimation. The first stage is meant to reduce the complexity of the ray-tracing algorithm by determining the so-called visibility relations among all building corners and trees, and has to be performed only once. The ray-tracing algorithm is based on the well-known concepts of virtual sources and illumination zones, but is enhanced in order to cope with rays passing through buildings. In the last stage, various channel parameters can be estimated from the amplitudes, phases, lengths and AOAs of the traced rays.

A new method was presented for the estimation of local mean power. This method is based on the spatial average of the received power over a given observation area or pixel, but does not require ray-tracing for more than one observation point per pixel. Unlike the so-called sum-of-individual-ray-powers, which is the most commonly used method to remove small-scale fading effects from prediction results, it remains accurate for the often occurring case of spatially correlated multipath signals.

An important benefit of the propagation model presented in this chapter is that outdoor-to-indoor propagation (at ground level) is automatically taken into account, as a "by-product" of the building transmission model. This phenomenon is receiving increased attention as indoor coverage is becoming an important aspect of mobile network quality.

In the last section of this chapter, path loss predictions obtained using the new model were compared with measured data. Considering the effects of transmission through buildings and scattering from trees was shown to result in a very significant improvement of the prediction accuracy.

7

Summary, conclusions and recommendations

7.1 Summary and conclusions

The work reported in this dissertation is aimed at contributing to the development of improved propagation prediction models for urban microcell environments and, at the same time, to a better physical understanding of radiowave propagation in such areas.

The first part of the study (Chapters 2 and 3) consisted of the experimental characterisation of radio channels at the level of the individual multipaths. The objective of these experiments was to identify the dominant propagation mechanisms in urban microcell environments. The method employed in the measurements and the processing of the data was the subject of Chapter 2. Separation of the received signal into its constituent multipath components was done on the basis of the different propagation delay times and angles-of-arrival of the multipath waves. The delay measurements were carried out at 1900 and 2000 MHz using a wideband radio channel sounder. For the measurement of the directional properties of multipath contributions, a synthetic uniform circular array of antennas was employed. An algorithm named UCA-MUSIC was developed for the high-resolution estimation of angles-of-arrival (azimuth and elevation) for each 20-ns time delay interval of the

measured channel impulse response. Preprocessing techniques, viz. beamspace processing and forward/backward averaging, were applied to improve the robustness of the algorithm against highly correlated multipath signals. The capability of the measurement method to identify the dominant propagation mechanisms in a real built-up environment was successfully tested.

The technique developed in Chapter 2 was used to perform extensive measurements in urban microcell environments in Bern and Fribourg, Switzerland, and also in more controlled, laboratory-like outdoor environments in Eindhoven and Boxtel, The Netherlands. These measurements were discussed in detail in Chapter 3. An important result of the measurements was the identification of two propagation mechanisms that have hitherto received little or no attention: transmission through buildings and scattering from trees. Building transmission is particularly significant in areas directly behind the buildings surrounding the base station antenna. In the experiments discussed in Section 3.2 and from additional measurement results presented in Chapter 4, the path loss associated with propagation paths through buildings was observed to be roughly in the range from 20 to 40 dB above the free-space loss. Such a low shielding effectiveness of buildings, if disregarded in the planning stage of urban microcellular networks, may lead to unacceptable levels of co-channel interference. Scattering from trees can be predominant in situations where the line-of-sight propagation path is obstructed and reflection and diffraction contributions are weak, for example in streets perpendicular to the street in which the base station is located. Experimental results discussed in Section 3.3 indicated that the fields scattered in all directions by trees located near a street intersection can be more significant than the fields diffracted by the building corners. Taking into account the effects of tree scattering will therefore lead to a better modelling of radiowave propagation around street corners.

In the second part of the study (Chapters 4 and 5), transmission and scattering models were developed that can be readily incorporated in ray-based propagation prediction tools. Chapter 4 presented a semi-empirical model for the transmission of radiowaves through buildings. The model is based on a physical-optics (PO) approximation of the interior (penetrated) and transmitted fields due to a ray-optical field incident on a building with plane faces. It does not require any information about the buildings other than the exterior coordinates, the complex permittivity of the exterior walls and an effective attenuation constant α_b. This constant characterises the attenuation experienced by radiowaves propagating through the building due to their interaction with the unknown building interior, and must be determined empirically. In Section 4.4, a new measurement technique – capable of separating the field due to building transmission from other, disturbing multipath components – was presented that can be used for this purpose. With the aid of this technique, α_b-values were

determined for a set of 22 buildings. Although these values showed some spread, most were concentrated closely around the average value of 2.0 dB/m. It is therefore expected that the model presented herein, in combination with the average value of α_b, has considerable predictive value.

In Chapter 5, a model was developed for the scattering of radiowaves from the canopy of a single tree. The canopy was modelled as a cylindrical volume containing randomly distributed and oriented cylinders, representing the branches, and thin disks, representing the leaves. The coherent and incoherent scattered fields outside the canopy were obtained as approximate solutions to a set of integral equations, each involving an integration over the canopy volume. Further approximations were made to reduce the computation time required to evaluate the resulting expressions. The accuracy of these approximations was investigated in Section 5.4. It was shown that the accuracy of the expressions for the coherent scattered field is reasonable, especially in the shadow region behind the tree, but not very good. The simplified expression for the incoherent scattered field, on the other hand, gives excellent results. It was further shown that coherent scattering dominates mainly in the shadow region, whereas incoherent scattering is more important in all other directions. Results of scattering measurements on a live tree were discussed in Section 5.5. Measurements of the attenuation behind the tree were disturbed by ground-reflections and could not be used to verify the coherent scattering model. Measured scattering cross sections, however, were shown to agree well with the incoherent scattering model.

In the third part of the study (Chapter 6) a new ray-tracing-based propagation prediction model, incorporating the transmission and scattering models of the previous chapters, was presented. It models the propagation of radiowaves between a mobile station and a low base station, which is modelled as being at the same height as the mobile station although this is in reality never the case. Buildings are modelled as being infinitely high, so that there is no propagation over rooftops. Based on ray parameters computed by the ray-tracing algorithm that forms the main stage of the prediction model, important channel parameters such as local mean power and delay spread can be estimated. Outdoor-to-indoor propagation at ground level is automatically taken care of as a "by-product" of the building transmission model. This is important as indoor coverage is becoming an important aspect of mobile network quality. Local mean power is computed using a new method that, unlike the conventional "sum-of-individual-ray-powers method", provides accurate values for the often occurring case of spatially correlated multipath signals. Path loss predictions for two urban microcell environments were shown to illustrate the very significant improvement in prediction accuracy that the new model can achieve.

7.2 Recommendations

The following recommendations are made regarding follow-up research on improved radiowave propagation modelling for urban microcell environments:

1. **Ground reflections.** Although ground reflections are neglected in the present work, it is a simple matter to include their effects in the new propagation model, without having to extend it to a three-dimensional model. (Of course, the antenna heights would have to be known.) To this end, the field associated with each ray is replaced by the combined field of the same ray plus a ground-reflected ray. This leads to a different behaviour of the ray amplitude as a function of the ray length, especially for ray lengths beyond the so-called break point [80].

2. **Tree shadowing.** The coherent tree-scattering model presented in this thesis can be simplified considerably by approximating the attenuation associated with propagation through a tree canopy by the path length through the canopy multiplied by the canopy attenuation coefficient α_c, as was proposed in [57]. Although this approach neglects the coherent scattered field outside the tree's shadow area and provides only a crude approximation of the "exact" attenuation as predicted using expression (5.30), from the results shown in the cited reference it appears to be quite adequate in describing the general effect of tree shadowing. This approach is particularly advantageous if the attenuation due to propagation through multiple canopies is computed. In that case, application of the scattering coefficient of Section 5.3.2 would mean that rays of high scattering order should be taken into account, which would lead to excessive computation times.

3. **Further experimental verification of the prediction model.** In order to assess the performance of the propagation model of Chapter 6 in terms of the rms prediction error that can be achieved in the actual practice of cell planning, it is necessary to compare predicted and measured data for a large number of points in several urban microcell environments. A relevant performance target is the rms prediction error that can at present be achieved for open macrocell environments (approximately 6 dB).

4. **Reduction of prediction times.** Significant reductions in computation time required by the prediction tool could probably be achieved by applying a pre-processing scheme proposed in [73], at the cost of some loss in accuracy. This technique, which subdivides the building faces into smaller "tiles" and determines the visibility relations of each tile with other tiles, building corners,

trees, etc. is claimed to accelerate the ray-tracing procedure by a factor of 1,000, reducing the ray-tracing time to several seconds on a standard personal computer.

5. **Prediction of fading statistics.** The general idea behind the method used in Chapter 6 to estimate local mean power (cf. Section 6.3) can also be used to compute other local channel parameters, such as the local envelope distribution of the received signal and the local correlation of fading signals between the elements of an antenna array ("fading correlation"). The latter parameter is highly relevant in the design of adaptive antenna array techniques such as space diversity and space-time processing.

6. **Extension to small-cell environments.** For so-called "small-cell" configurations, in which the base station antenna is located approximately at the rooftop level and over-rooftop propagation is no longer negligible, two-dimensional propagation prediction models are inadequate [29, 71]. For propagation prediction in such configurations it may be desirable to extend the presented transmission and scattering models, which are now valid only for horizontal ray incidence, to three dimensions.

References

[1] *The path towards UMTS technologies for the information society*, UMTS Forum Report No. 2. UMTS Forum, London, UK, Sept. 1998.

[2] A. Mawira, "Terrestrial land-mobile communications," *Tijdschrift van het Nederlands Elektronica- en Radiogenootschap*, vol. 60, no. 1, pp. 19–23, 1995.

[3] M. Hata, "Empirical formula for propagation loss in land mobile radio services," *IEEE Trans. Veh. Technol.*, vol. VT-29, no. 3, pp. 317–325, Aug. 1980.

[4] E. Damosso and L.M. Correia, Eds., *COST 231 Final Report*, Commission of the European Community, Torino, Italy, 1996.

[5] B.H. Fleury and P.E. Leuthold, "Radiowave propagation in mobile communications: an overview of European research," *IEEE Commun. Mag.*, vol. 34, no. 2, pp. 70–81, Feb. 1996.

[6] G.A.J. van Dooren, *A deterministic approach to the modelling of electromagnetic wave propagation in urban environments*, Ph.D. thesis, Eindhoven University of Technology, Eindhoven, The Netherlands, 1994.

[7] M.G.J.J. Klaassen and A. Mawira, "A deterministic model for the planning of microcellular mobile radio communication systems," in *Proc. 5th IEEE Int. Symp. Personal, Indoor and Mobile Radio Communications (PIMRC'94)*, The Hague, The Netherlands, 1994, pp. 389–395.

[8] F. Ikegami and S. Yoshida, "Analysis of multipath propagation structure in urban mobile radio environments," *IEEE Trans. Antennas Propagat.*, vol. AP-28, no. 4, pp. 531–537, July 1980.

[9] J. Fuhl, J.-P. Rossi, and E. Bonek, "High-resolution 3-D direction-of-arrival determination for urban mobile radio," *IEEE Trans. Antennas Propagat.*, vol. 45, no. 4, pp. 672–682, Apr. 1997.

[10] J.G.O. Moss, A.M. Street, and D.J. Edwards, "Wideband radio imaging technique for multipath environments," *Electron. Lett.*, vol. 33, no. 11, pp. 941–942, May 1997.

[11] Y.L.C. de Jong and M.H.A.J. Herben, "Accurate identification of scatterers for improved microcell propagation modelling," in *Proc. 8th IEEE Int. Symp. Personal, Indoor and Mobile Radio Communications (PIMRC'97)*, Helsinki, Finland, 1997, vol. 2, pp. 645–649.

[12] K.I. Pedersen, B.H. Fleury, and P.E. Mogensen, "High resolution of electromagnetic waves in time-varying radio channels," in *Proc. 8th IEEE Int. Symp. Personal, Indoor and Mobile Radio Communications (PIMRC'97)*, Helsinki, Finland, 1997, vol. 2, pp. 650–654.

[13] J.-P. Rossi, J.-P. Barbot, and A.J. Levy, "Theory and measurement of the angle of arrival and time delay of UHF radiowaves using a ring array," *IEEE Trans. Antennas Propagat.*, vol. 45, no. 5, pp. 876–884, May 1997.

[14] T. Manabe and H. Takai, "Superresolution of multipath delay profiles measured by PN correlation method," *IEEE Trans. Antennas Propagat.*, vol. 40, no. 5, pp. 500–509, May 1992.

[15] D.C. Cox, "Delay Doppler characteristics of multipath propagation at 910 MHz in a suburban mobile radio environment," *IEEE Trans. Antennas Propagat.*, vol. AP-20, no. 5, pp. 625–635, Sept. 1972.

[16] Y.L.C. de Jong and M.H.A.J. Herben, "High-resolution angle-of-arrival measurement of the mobile radio channel," *IEEE Trans. Antennas Propagat.*, vol. 47, no. 11, pp. 1677–1687, Nov. 1999.

[17] L.C. Godara, "Applications of antenna arrays to mobile communications, part II: beam-forming and direction-of-arrival considerations," *Proc. IEEE*, vol. 85, no. 8, pp. 1195–1245, Aug. 1997.

[18] M. Wax and J. Sheinvald, "Direction finding of coherent signals via spatial smoothing for uniform circular arrays," *IEEE Trans. Antennas Propagat.*, vol. 42, no. 5, pp. 613–620, May 1994.

[19] M. Abramowitz and I.A. Stegun, *Handbook of Mathematical Functions*, Nat. Bureau Standard, Appl. Math., 1964.

[20] U. Nickel, "Angular superresolution with phased array radar: a review of algorithms and operational constraints," *IEE Proc.-F*, vol. 134, no. 1, pp. 53–59, Feb. 1987.

[21] P.J.D. Gething, *Radio direction finding and superresolution*, Peregrinus, London, 1991.

[22] C.P. Mathews and M.D. Zoltowski, "Eigenstructure techniques for 2-D angle estimation with uniform circular arrays," *IEEE Trans. Signal Proc.*, vol. 42, no. 9, pp. 2395–2407, Sept. 1994.

[23] R.O. Schmidt, "Multiple emitter location and signal parameter estimation," *IEEE Trans. Antennas Propagat.*, vol. AP-34, no. 3, pp. 276–280, Mar. 1986.

[24] G. Xu, R.H. Roy, and T. Kailath, "Detection of number of sources via exploitation of centro-symmetry property," *IEEE Trans. Signal Proc.*, vol. 42, no. 1, pp. 102–112, Jan. 1994.

[25] H. Akaike, "A new look at the statistical model identification," *IEEE Trans. Automat. Contr.*, vol. AC-19, no. 6, pp. 716–723, Dec. 1974.

[26] M. Wax and T. Kailath, "Detection of signals by information theoretic criteria," *IEEE Trans. Acoust., Speech, Signal Processing*, vol. ASSP-33, no. 2, pp. 387–392, Apr. 1985.

[27] L. Chang and C.-C. Yeh, "Resolution threshold for coherent sources using smoothed eigenstructure methods," *IEE Proc.-F*, vol. 138, no. 5, pp. 470–478, Oct. 1991.

[28] S.U. Pillai and B.H. Kwon, "Forward/backward spatial smoothing techniques for coherent signal identification," *IEEE Trans. Acoust., Speech, Signal Processing*, vol. 37, no. 1, pp. 8–15, Jan. 1989.

[29] K. Rizk, *Propagation in microcellular and small cell urban environment*, Ph.D. thesis, Ecole Polytechnique Fédérale de Lausanne, Lausanne, Switzerland, 1997.

[30] M.H.J.L. Koelen, "Measurements and modelling of transmission of radiowaves through buildings," M.S. thesis, Eindhoven University of Technology, Eindhoven, The Netherlands, 2000.

[31] J.-F. Wagen and K. Rizk, "Ray tracing based prediction of impulse responses in urban microcells," in *Proc. IEEE 44th Veh. Technol. Conf. (VTC'94)*, Stockholm, Sweden, 1994, pp. 210–214.

[32] R. Jakoby and U. Liebenow, "Modelling of radiowave propagation in microcells," in *Proc. Ninth Int. Conf. Antennas Propagat. (ICAP'95)*, Eindhoven, The Netherlands, 1995, pp. 377–380.

[33] Y.L.C. de Jong and M.H.A.J. Herben, "Experimental verification of ray-tracing based propagation prediction models for urban microcell environments," in *Proc. IEEE 50th Veh. Technol. Conf. (VTC'99–Fall)*, 1999, vol. 3, pp. 1434–1438.

[34] J. Horikoshi, K. Tanaka, and T. Morinaga, "1.2 GHz band wave propagation measurements in concrete building for indoor radio communications," *IEEE Trans. Veh. Technol.*, vol. VT-35, no. 4, pp. 146–152, Nov. 1986.

[35] A. Davidson and C. Hill, "Measurement of building penetration into medium buildings at 900 and 1500 MHz," *IEEE Trans. Veh. Technol.*, vol. 46, no. 1, pp. 161–168, Feb. 1997.

[36] C.J. Haslett, "The transmission of microwaves through buildings," in *Proc. Progress In Electromagnetic Research Symposium (PIERS'94)*, Noordwijk, The Netherlands, 1994, pp. 1–5.

[37] C.J. Haslett and D.A. Jacklin, "Site shielding reduction due to transmission through buildings in a city centre environment," in *Proc. Ninth Int. Conf. on Antennas and Propagation (ICAP'95)*, Eindhoven, The Netherlands, 1995, pp. 37–41.

[38] B. de Backer, F. Olyslager, and F. de Zutter, "An integral equation approach to the prediction of wave propagation in an indoor environment," in *Proc. IEEE 3rd Symp. Commun. and Veh. Technol. in the Benelux (SCVT'95)*, Eindhoven, The Netherlands, 1995, pp. 28–33.

[39] A. Lauer, "FDTD simulations of indoor propagation," in *Proc. IEEE 44th Veh. Technol. Conf. (VTC'94)*, Stockholm, Sweden, 1994, pp. 883–886.

[40] W.M.C. Dolmans, *Effect of indoor fading on the performance of an adaptive antenna system*, Ph.D. thesis, Eindhoven University of Technology, Eindhoven, The Netherlands, 1997.

[41] S.Y. Seidel and T.S. Rappaport, "Site-specific propagation prediction for wireless in-building personal communication system design," *IEEE Trans. Veh. Technol.*, vol. 43, no. 4, pp. 879–891, Nov. 1994.

[42] W. Honcharenko, H.L. Bertoni, J.L. Dailing, J. Qian, and H.D. Yee, "Mechanisms governing UHF propagation on single floors in modern office buildings," *IEEE Trans. Veh. Technol.*, vol. 41, no. 4, pp. 496–504, Nov. 1992.

[43] R.J. Luebbers, "Finite conductivity uniform GTD versus knife edge diffraction in prediction of propagation path loss," *IEEE Trans. Antennas Propagat.*, vol. AP-32, no. 1, pp. 70–76, Jan. 1984.

[44] R. Tiberio, G. Pelosi, and G. Manara, "A uniform GTD formulation for the diffraction by a wedge with impedance faces," *IEEE Trans. Antennas Propagat.*, vol. AP-33, no. 8, pp. 867–873, Aug. 1985.

[45] N.D. Taket and R.E. Burge, "A physical optics version of the geometrical theory of diffraction," *IEEE Trans. Antennas Propagat.*, vol. 39, no. 6, pp. 719–731, June 1991.

[46] R.E. Burge, X.-C. Yuan, B.D. Caroll, N.E. Fisher, T.J. Hall, G.A. Lester, N.D. Taket, and C.J. Oliver, "Microwave scattering from dielectric wedges with planar surfaces: a diffraction coefficient based on a physical optics version of GTD," *IEEE Trans. Antennas Propagat.*, vol. 47, no. 10, pp. 1515–1527, Oct. 1999.

[47] C.A. Balanis, *Advanced engineering electromagnetics*, John Wiley, New York, 1989.

[48] K. Rizk, J.-F. Wagen, and F. Gardiol, "Two-dimensional ray tracing modeling for propagation prediction in microcellular environments," *IEEE Trans. Veh. Technol.*, vol. 46, no. 2, pp. 508–518, May 1997.

[49] G.E. Athanasiadou and A.R. Nix, "Investigation into the sensitivity of the power predictions of a microcellular ray tracing propagation model," *IEEE Trans. Veh. Technol.*, vol. 49, no. 4, pp. 1140–1151, July 2000.

[50] W.D. Burnside and K.W. Burgener, "High frequency scattering by a thin lossless dielectric slab," *IEEE Trans. Antennas Propagat.*, vol. AP-31, no. 1, pp. 104–110, Jan. 1983.

[51] N. Morita, N. Kumagai, and J.R. Mautz, *Integral equation methods for electromagnetics*, Artech House, Boston, 1990.

[52] J.A.C. Weideman, "Computation of the complex error function," *SIAM J. Numer. Anal.*, vol. 31, no. 5, pp. 1497–1518, Oct. 1994.

[53] Y.L.C. de Jong, M.H.A.J. Herben, J.-F. Wagen, and A. Mawira, "Transmission of UHF radiowaves through buildings in urban microcell environments," *Electron. Lett.*, vol. 35, no. 9, pp. 743–745, Apr. 1999.

[54] Y.L.C. de Jong, M.H.J.L. Koelen, and M.H.A.J. Herben, "Measurement of building transmission loss using wideband radio channel sounding," *Electron. Lett.*, vol. 36, no. 12, pp. 1067–1069, June 2000.

[55] W.C.Y. Lee, *Mobile communications design fundamentals*, Sams, Indianapolis, 1986.

[56] W.J. Vogel and J. Goldhirsh, "Earth-satellite tree attenuation at 20 GHz: foliage effects," *Electron. Lett.*, vol. 29, no. 18, pp. 1640–1641, Sept. 1993.

[57] S.A. Torrico, H.L. Bertoni, and R.H. Lang, "Modeling tree effects on path loss in a residential environment," *IEEE Trans. Antennas Propagat.*, vol. 46, no. 6, pp. 872–880, June 1998.

[58] M.A. Karam, A.K. Fung, and Y.M.M. Antar, "Electromagnetic wave scattering from some vegetation samples," *IEEE Trans. Geosci. Remote Sensing*, vol. 26, no. 6, pp. 799–808, Nov. 1988.

[59] M.A. Karam and A.K. Fung, "Electromagnetic scattering from a layer of finite length, randomly oriented, dielectric, circular cylinders over a rough interface with application to vegetation," *Int. J. Remote Sensing*, vol. 9, no. 6, pp. 1109–1134, 1988.

[60] A. Ishimaru, *Wave propagation and scattering in random media*, Academic Press, New York, 1978.

[61] M.A. Karam and A.K. Fung, "Leaf-shape effects in electromagnetic wave scattering from vegetation," *IEEE Trans. Geosci. Remote Sensing*, vol. 27, no. 6, pp. 687–697, Nov. 1989.

[62] G.I. Torgovnikov, *Dielectric properties of wood and wood-based materials*, Springer-Verlag, Berlin, 1993.

[63] L.B. Felsen and N. Marcuvitz, *Radiation and scattering of waves*, Prentice-Hall, New Jersey, 1973.

[64] R.M. Lewis, "Asymptotic theory of transients," in *Electromagnetic wave theory*, J. Brown, Ed. Pergamon Press, 1967.

[65] M. Taher Abuelma'atti, "An improved approximation to the Fresnel integral," *IEEE Trans. Antennas Propagat.*, vol. 37, no. 7, pp. 946–947, July 1989.

[66] F.T. Ulaby, T.E. van Deventer, J.R. East, T.F. Haddock, and M.E. Coluzzi, "Millimeter-wave bistatic scattering from ground and vegetation targets," *IEEE Trans. Geosci. Remote Sensing*, vol. 26, no. 3, pp. 229–243, May 1988.

[67] K.C. McDonald, M.C. Dobson, and F.T. Ulaby, "Using MIMICS to model L-band multiangle and multitemporal backscatter from a walnut orchard," *IEEE Trans. Geosci. Remote Sensing*, vol. 28, no. 4, pp. 477–491, July 1990.

[68] M.A. Karam, A.K. Fung, R.H. Lang, and N.S. Chauhan, "A microwave scattering model for layered vegetation," *IEEE Trans. Geosci. Remote Sensing*, vol. 30, no. 4, pp. 767–784, July 1992.

[69] C. Mätzler, "Microwave (1-100 GHz) dielectric model of leaves," *IEEE Trans. Geosci. Remote Sensing*, vol. 32, no. 5, pp. 947–949, Sept. 1994.

[70] F.T. Ulaby, R.K. Moore, and A.K. Fung, *Microwave remote sensing: active and passive*, vol. 3, Appendix E, Artech House, Dedham, Massachusetts, 1986.

[71] V. Erceg, A.J. Rustako, and R.S. Roman, "Diffraction around corners and its effects on the microcell coverage area in urban and suburban environments at 900 MHz, 2 GHz, and 6 GHz," *IEEE Trans. Veh. Technol.*, vol. 43, no. 3, pp. 762–766, Aug. 1994.

[72] B. Chopard, P.O. Luthi, and J.-F. Wagen, "Lattice Boltzmann method for wave propagation in urban microcells," *IEE Proc.-Microw. Antennas Propag.*, vol. 144, no. 4, pp. 251–255, Aug. 1997.

[73] R. Hoppe, G. Wölfle, and F.M. Landstorfer, "Accelerated ray optical propagation modeling for the planning of wireless communication networks," in *Proc. 1999 IEEE Radio and Wireless Conf. (RAWCON'99)*, Piscataway, New Jersey, 1999, pp. 159–162.

[74] G.A.J. van Dooren and M.H.A.J. Herben, "A deterministic approach for the modeling of wave propagation around buildings," *J. Electromag. Waves Appl.*, vol. 8, no. 2, pp. 175–194, 1994.

[75] P.S. Heckbert, Ed., *Graphics Gems IV*, pp. 3–6, Academic Press, Cambridge, Massachusetts, 1994.

[76] G.E. Athanasiadou, A.R. Nix, and J.P. McGeehan, "A microcellular ray-tracing propagation model and evaluation of its narrow-band and wide-band predictions," *IEEE J. Select. Areas Commun.*, vol. 18, no. 3, pp. 322–335, Mar. 2000.

[77] S.-C. Kim, B.J. Guarino, T.M. Willis, V. Erceg, S.J. Fortune, R.A. Valenzuela, L.W. Thomas, J. Ling, and J.D. Moore, "Radio propagation measurements and prediction using three-dimensional ray tracing in urban environments at 908 MHz and 1.9 GHz," *IEEE Trans. Veh. Technol.*, vol. 48, no. 3, pp. 931–946, May 1999.

[78] Y.L.C. de Jong and M.H.A.J. Herben, "Prediction of local mean power using 2-D ray-tracing-based propagation models," *IEEE Trans. Veh. Technol.*, vol. 50, no. 1, pp. 325–331, Jan. 2001.

[79] G. Lampard and T. Vu-Dinh, "The effect of terrain on radio propagation in urban microcells," *IEEE Trans. Veh. Technol.*, vol. 42, no. 3, pp. 314–317, Aug. 1993.

[80] H.H. Xia, H.L. Bertoni, L.R. Maciel, A. Lindsay-Stewart, and R. Rowe, "Radio propagation characteristics for line-of-sight microcellular and personal communications," *IEEE Trans. Antennas Propagat.*, vol. 41, no. 10, pp. 1439–1447, Oct. 1993.

Samenvatting

Het in dit proefschrift beschreven werk is bedoeld als bijdrage aan een beter fysisch begrip van radiogolfvoortplanting (radiopropagatie) in stedelijke microcelomgevingen en tevens aan de ontwikkeling van verbeterde propagatievoorspellingsmodellen voor dergelijke omgevingen. Nadruk wordt gelegd op de identificatie, door middel van geavanceerde experimenten, en modellering van de dominante propagatiemechanismen in de UHF band.

Het eerste gedeelte van de studie behandelt de experimentele karakterisering van mobiele radiokanalen met betrekking tot de propagatielooptijden en aankomsthoeken van individuele multipadgolven, met behulp van een radiokanaalsounder in combinatie met een gesynthetiseerd antennestelsel. Resultaat van deze metingen is de identificatie van twee propagatiemechanismen die tot nu toe weinig of geen aandacht hebben gekregen: transmissie door gebouwen en verstrooiing aan bomen. Transmissie door gebouwen is vooral belangrijk direct achter gebouwen rondom de basisstationantenne. Verstrooiing aan bomen kan bijvoorbeeld een overheersende rol spelen bij propagatie om straathoeken.

Het tweede gedeelte behandelt de ontwikkeling van transmissie- en verstrooiingsmodellen die eenvoudig zijn op te nemen in propagatievoorspellingsmodellen die op de stralenbenadering zijn gebaseerd. Het model voor transmissie door gebouwen vereist geen andere informatie over de gebouwen dan de externe coördinaten, de permittiviteit van de buitenmuren en een effectieve verzwakkingscoëfficiënt. De laatstgenoemde coëfficiënt karakteriseert de verzwakking van zich door het inwendige van een gebouw voortplantende radiogolven en moet worden bepaald door middel van metingen. Dit wordt gedaan voor een groot aantal gebouwen. Een model voor de coherente en incoherente verstrooiing aan een enkele boom wordt ontwikkeld op basis van de meervoudige verstrooiingstheorie van Twersky. Numerieke resultaten gegenereerd met behulp van dit model komen redelijk tot goed overeen met meetdata.

Het derde gedeelte van de studie introduceert een nieuw, op de techniek van *ray-tracing* gebaseerd propagatievoorspellingsmodel, waarin de transmissie- en ver-

strooiingsmodellen van het voorgaande gedeelte zijn opgenomen. Dit model maakt gebruik van een nieuwe methode voor de schatting van lokaal gemiddeld vermogen. In tegenstelling tot de conventionele vermogensoptelling van multipadsignalen produceert deze methode ook correcte waarden voor het veel voorkomende geval van ruimtelijk gecorreleerde signalen. De opmerkelijke nauwkeurigheidsverbetering die kan worden behaald met het nieuwe model wordt geïllustreerd aan de hand van padverliesvoorspellingen voor twee stedelijke microcelomgevingen.

Acknowledgments

The completion of this thesis would not have been possible without the support of the following people, to whom I would like to express my sincere gratitude.

Staff members and students in the Radiocommunications Group of the Eindhoven University of Technology were responsible for creating an excellent atmosphere, in which it has been a pleasure to work. Jaap Swijghuisen Reigersberg and Ludi Wijdemans were always there to provide technical assistance in the many experiments performed, even if this meant giving up a day off now and then. Special thanks go to Matti Herben and Gert Brussaard, for stimulating feedback and discussions, for taking care of many administrative issues and for providing the right degree of freedom.

Irene Fernández Díaz, Noelia Vàzquez Mejuto and Maikel Koelen did a lot of good work during their graduation projects in the Radiocommunications Group, which has contributed much to the research reported in this thesis. Maikel Koelen, in particular, is responsible for a large part of the experimental work described in Chapter 4. In his practical training period Hans Puttenstein rewrote some of the software for the TU/e channel sounder, for which I am grateful.

Colleagues at KPN Research in Leidschendam, in particular Bi Mawira, gave me the opportunity to have a glance at the dynamic business of mobile telecommunications from within, and to learn more about the actual practice of propagation prediction and cell planning. This experience has proved to be invaluable. I am indebted to Peter Rijsdijk of KPN Research for his technical support and pleasant company during measurements, and for the excellent preparations he made for the experiments in Switzerland.

Jean-Frédéric Wagen and his former colleagues at Swisscom Corporate Information and Technology in Bern made possible my stay in Switzerland during five months in 1998. Despite some serious technical problems, which were eventually solved thanks to the skills and perseverance of Erich Zimmermann, this period has brought me many good memories. Moreover, the experimental results obtained in

Switzerland are an important element of the work presented in this thesis.

Koen van Staalduinen and Hans van Bruggen, who were with Ericsson Business Mobile Networks in Enschede at the time, made available the channel sounding equipment that was used for many measurements in 1997 and 1998. Their cooperation and support are gratefully acknowledged.

I am grateful to Mr and Mrs Jacobs in Boxtel for being so kind as to let us do measurements on their land during many days in 1999 and 2000.

Robert Bultitude (Communications Research Centre, Ottawa, and Carleton University, Ottawa), Rolf Jakoby (Darmstadt University of Technology, Darmstadt), Bi Mawira (KPN Research, Leidschendam) and Anton Tijhuis (Eindhoven University of Technology) are thanked for reading and commenting on the draft version of this thesis.

Frank Zomerdijk created the cover of this thesis. I am an admirer of his work.

Other people I would like to thank, for various reasons, are Karim Rizk (Wavecall, Lausanne), Pierre Melançon and Tyler Smith (Communications Research Centre, Ottawa) and Christian Mätzler (University of Berne, Bern).

Finally, I thank Nathalie, my parents and other family members for their stimulation and support.

Curriculum vitae

Yvo de Jong, the author of this thesis, was born in Vlaardingen, The Netherlands, on June 13, 1972. From 1984 to 1990, he attended secondary school at the Willem van Oranje College in Waalwijk. In 1996 he received the M.Sc. degree in electrical engineering (*cum laude*) from the Eindhoven University of Technology (TU/e) in Eindhoven, The Netherlands. His Master's thesis was concerned with a bidirectional communication scheme for cable television networks, based on code-division multiple access (CDMA). He then became a Research Assistant in the Radiocommunications Group of the TU/e, where he has been active in the area of radiowave propagation modelling with application in mobile communications. In the framework of this research he visited KPN Research in Leidschendam, The Netherlands, from January, 1997 to May, 1998, and Swisscom Corporate Information and Technology in Bern, Switzerland, from June to October, 1998. The results of his work have been published in several internationally available refereed journals and at conferences, and have led to this dissertation. As of July, 2001, he will be with the Communications Research Centre in Ottawa, Canada.